

**CONSTITUTIVE MODELING OF HEXAGONAL
CLOSE PACKED POLYCRYSTALS**

By

HUAMIAO WANG, M.A.Sc.

A Thesis

**Submitted to the School of Graduate Studies
in Partial Fulfilment of the Requirements
for the Degree of Doctor of Philosophy**

McMaster University

©Copyright by Huamiao Wang, Septembe 2010

TITLE: CONSTITUTIVE MODELING OF HEXAGONAL CLOSE PACKED
POLYCRYSTALS

AUTHOR: Huamiao WANG
B. Eng (Xi'an Jiaotong University)
M. A. Sc. (Tsinghua University)

SUPERVISOR: Dr. Peidong WU

NUMBER OF PAGES: XI, 124

ABSTRACT

There is a growing interest in magnesium and its alloys due to their high strength to weight ratio. Magnesium is of particular interest to the automotive industry as a consequence of the current pressure to reduce green house gas emissions from the transportation sector through vehicle weight reduction. However, there is a lack of knowledge concerning the formability of magnesium. As a result, the application of magnesium as a commercial material has not been fully exploited. Much has been learned from the constitutive modeling of materials such as aluminum and steel. Therefore, this thesis considers the constitutive modeling of magnesium and its alloys.

Based on this motivation, polycrystal plasticity theories that have been established and used to characterize aluminum and steel are studied. The validity of these theories is examined with respect to magnesium and its alloys. The magnesium system is composed of the hexagonal closed-packed (HCP) crystal structure. Therefore, a strong plastic anisotropy is induced in magnesium crystals due to the limited number of slip systems that may be activated with ease. The models proposed by Taylor and Sachs neglect strain and stress heterogeneities respectively. As a result, the models are either too stiff or too soft to study magnesium due to the anisotropic nature of the crystal structure. The intermediate models; self-consistent models, which are able to consider the heterogeneities among the grains in polycrystals, are believed to be more suitable to study magnesium and its alloys. Therefore, a large strain elastic-viscoplastic self-consistent (EVPSC) model is developed for polycrystalline materials. Both rate sensitive slip and twinning are included as mechanisms of plastic deformation, while elastic anisotropy is accounted for in the elastic modulus. The transition from single crystal plasticity to polycrystal plasticity is based on a completely self-consistent approach. It is shown that the differences in the predicted stress-strain curves and texture evolutions based on the EVPSC and the viscoplastic self-consistent (VPSC) model proposed by Lebensohn and Tomé (1993) are negligible at large strains for monotonic loadings. For the deformations involving unloading and strain path changes, the EVPSC predicts a smooth elasto-plastic transition, while the VPSC model gives a discontinuous response because the model is incapable of modeling elastic deformation. In addition, it is demonstrated that the EVPSC model can capture some important experimental features which cannot be simulated by using the VPSC model.

Various self-consistent schemes exist for EVPSC and VPSC models. However, the evaluations of these models are not complete. Therefore, an examination of various polycrystal plasticity models is made, based on comparisons of the predicted and experimental stress responses as well as the R values, to assess their validity. It is established that, among the models examined, the self-consistent models with grain interaction stiffness values halfway between those of the limiting Secant (stiff) and

Tangent (compliant) approximations give the best results. Among the available options, the Affine self-consistent scheme results in the best overall performance. Furthermore, it is demonstrated that the R values under uniaxial tension and compression within the sheet plane show a strong dependence on the imposed strain. This suggests that the development of anisotropic yield functions using measured R values, must account for the strain dependence.

The recently developed large strain elastic visco-plastic self-consistent (EVPSC) model, which incorporates both slip and twinning deformation mechanisms, is used to study the lattice strain evolution in extruded magnesium alloy AZ31 under uniaxial tension and compression. The results are compared against in-situ neutron diffraction measurements done on the same alloy. For the first time, the effects of stress relaxation and strain creep on lattice strain measurements in respectively displacement controlled and load controlled in-situ tests are numerically assessed. It is found that the stress relaxation has a significant effect on the lattice strain measurements. It is also observed that although the creep does not significantly affect the trend of the lattice strain evolution, a better agreement with the experiments is found if creep is included in the simulations.

In conjunction with the M-K approach developed by Marciniak and Kuczynski (1967), the EVPSC model is applied to study the sheet metal formability of magnesium alloys in terms of the forming limit diagram (FLD). The role of crystal plasticity models and the effects of basal texture on formability of magnesium alloy AZ31B sheet are studied numerically. It is observed that formability in HCP polycrystalline materials is very sensitive to the intensity of the basal texture. The path-dependency of formability is examined based on different non-proportional loading histories, which are combinations of two linear strain paths. It is found that while the FLD in strain space is very sensitive to strain path changes, the forming limit stress diagram (FLSD) in stress space is much less path-dependent. It is suggested that the FLSD is much more favourable than the FLD in representing forming limits in the numerical simulation of sheet metal forming processes. The numerical results are found to be in good qualitative agreement with experimental observations.

ACKNOWLEDGEMENT

I would like to gratefully acknowledge my supervisor, Dr. Peidong Wu, not only for his intellectual support, excellent guidance and advice, constant encouragement and stimulation, but also for his kindness helping me to get used to working and living in Canada.

My sincere gratitude is attributed to Dr. Keh-Chih Hwang (Tsinghua University, China) and Dr. Yonggang Huang (Northwestern University, USA) for their leading me to the field of crystal plasticity and introducing me to Dr. Wu.

I would like to thank Dr. Carlos N Tomé (Los Alamos National Laboratory, USA) for his providing the VPSC and EPSC codes and Dr. Sean A Agnew (University of Virginia Charlottesville, USA) for his providing the experimental data. Their valuable comments and suggestions are also acknowledged.

I would also like to thank the collaborators for their interests and kind supports: Dr. Kenneth W Neale (University of Sherbrooke, Canada), Dr. Michael A Gharghouri (Chalk River Laboratory, Canada) and Dr. Kevin P Boyle (CANMET Materials Technology Laboratory, Canada).

Finally, I would like to thank my parents for their great support and understanding during my graduate studies.

DEDICATION

This is dedicated to my beloved parents and my younger brother.

This thesis is based on the following publications with permission:

Chapter 2. Wang, H., Wu, P.D., Tomé, C.N., Huang, Y., 2010. A finite strain elastic-viscoplastic self-consistent model for polycrystalline materials. *Journal of the Mechanics and Physics of Solids* 58, 594-612.

Chapter 3. Wang, H., Raeisinia, B., Wu, P.D., Agnew, S.R., Tomé, C.N., 2010. Evaluation of self-consistent crystal plasticity models for magnesium alloy AZ31B sheet. *International Journal of Solids and Structures* 47, 2905-1917.

Chapter 4. Wang, H., Wu, P.D., Tomé, C.N., 2010. Study of lattice strain measurements of magnesium alloy AZ31 using EVPSC model. *Acta Materialia*, to be submitted.

Chapter 5. Wang, H., Wu, P.D., Boyle, K.P., Neale, K.W., 2010. On crystal plasticity formability analysis for magnesium alloy sheets. *International Journal of Solids and Structures*. In press, doi:10.1016/j.ijsolstr.2010.1012.1004.

Author's contribution to publications:

All the four papers were written by the author and his co-workers. The following are the contributions by author in all four publications:

- (a) Development and validation of the algorithms, numerical procedures and simulation experiments.
- (b) Preparing the results.
- (c) Preparing the manuscripts.

Table of Contents

| | |
|--|-----|
| ABSTRACT..... | I |
| ACKNOWLEDGEMENT | III |
| DEDICATION..... | IV |
| Table of Contents..... | VI |
| Table of Figures | VII |
| Table of Tables | XI |
| Chapter 1. General introduction | 1 |
| 1.1 Background | 1 |
| 1.2 Crystallography of HCP metals..... | 2 |
| 1.3 Deformation of HCP metals..... | 4 |
| 1.3.1 Elastic behavior..... | 4 |
| 1.3.2 Deformation slip | 5 |
| 1.3.3 Deformation twinning..... | 6 |
| 1.4 Deformation of Magnesium | 11 |
| 1.4.1 Plastic deformation of pure magnesium | 11 |
| 1.4.2 Deformation of magnesium alloys..... | 16 |
| 1.5 Constitutive modeling of polycrystalline materials | 20 |
| 1.5.1 Continuum phenomenological models | 20 |
| 1.5.2 Polycrystal models | 21 |
| Chapter 2. A finite strain elastic-viscoplastic self-consistent model for polycrystalline materials | 26 |
| 2.1 Introduction | 26 |
| 2.2 Constitutive relations for single crystals | 30 |
| 2.3 A large strain EVPSC model..... | 33 |
| 2.3.1 A rigid viscoplastic inclusion embedded in a homogeneous viscoplastic matrix | 34 |
| 2.3.2 An elastic inclusion embedded in a homogeneous elastic matrix..... | 35 |
| 2.3.3 An elastic-viscoplastic inclusion embedded in a homogeneous elastic-viscoplastic matrix..... | 36 |
| 2.4 Specific constitutive functions | 37 |
| 2.5 Results and Discussions | 40 |
| 2.6 Conclusions | 49 |
| Chapter 3. Evaluation of self-consistent polycrystal plasticity models for magnesium alloy AZ31B sheet | 51 |
| 3.1 Introduction | 51 |

| | | |
|--------------|--|-----|
| 3.2 | Polycrystal plasticity models..... | 54 |
| 3.3 | Results and Discussions | 58 |
| 3.4 | Conclusions | 69 |
| Chapter 4. | Study of lattice strains in magnesium alloy AZ31 based on EVPSC model | 71 |
| 4.1 | Introduction | 71 |
| 4.2 | Lattice strains | 73 |
| 4.3 | The EVPSC model | 74 |
| 4.4 | Results and discussions | 76 |
| 4.5 | Conclusions | 91 |
| Chapter 5. | On crystal plasticity formability analysis for magnesium alloy sheets..... | 93 |
| 5.1 | Introduction | 93 |
| 5.2 | Constitutive Model..... | 95 |
| 5.3 | Problem formulation and method of solution | 98 |
| 5.4 | Results and discussions | 100 |
| 5.5 | Conclusions | 111 |
| Chapter 6. | General conclusions | 112 |
| Bibliography | | 114 |

Table of Figures

| | | |
|-------------|--|----|
| Figure 1.1 | The hexagonal close packed unit cell..... | 2 |
| Figure 1.2 | Important planes and directions in the hexagonal system (Patridge, 1967)..... | 2 |
| Figure 1.3 | Anisotropy of Young's modulus in (a) magnesium and (b) zinc (Schmid and Boas, 1950)..... | 4 |
| Figure 1.4 | Bi-pyramidal construction for the HCP lattice (Berghezan et al., 1961)..... | 6 |
| Figure 1.5 | Crystallographic elements of twinning. | 7 |
| Figure 1.6 | Twinning elements of twinning mode $\{10\bar{1}2\} <10\bar{1}\bar{1}>$ | 8 |
| Figure 1.7 | Stress-strain curve of a cadmium single crystal. Each serration corresponds to the formation of a twin (Schmid and Boas, 1950)..... | 8 |
| Figure 1.8 | Effect of texture on the stress-strain curves of highly textured pure magnesium (Reed-Hill, 1973). | 10 |
| Figure 1.9 | Some details of twinning in magnesium (a) Twinning on $\{10\bar{1}2\}$ occurs in tension perpendicular or compression parallel to the $\{0001\}$ basal plane and reorients the basal plane through 86.3° . (b) Under an opposite system of loading, a $\{10\bar{1}1\}$ twin can form and then retwin (c) on $\{10\bar{1}2\}$. A similar double twinning processes, (d)-(e), can occur on a $\{10\bar{1}3\}$ plane (Wonsiewicz and Backofen, 1967)..... | 12 |
| Figure 1.10 | Stress-strain curves for magnesium crystals compressed along $<0001>$ with expansion limited to (a) $<\bar{1}210>$ and (b) $<10\bar{1}0>$ (Wonsiewicz and Backofen, 1967). | 13 |

| | |
|--|----|
| Figure 1.11 Stress-strain curves for magnesium crystals compressed along (a) $\langle 11\bar{2}0 \rangle$ and (b) $\langle 10\bar{1}0 \rangle$ with expansion limited parallel to the $\langle 0001 \rangle$ direction (Wonsiewicz and Backofen, 1967). | 13 |
| Figure 1.12 Stress-strain curves for pure magnesium under channel die compression (Kelley and Hosford, 1968b). | 15 |
| Figure 1.13 Stress-strain curves for textured magnesium under channel die compression. The orientations are combinations of the letters R (rolling direction), T (transverse direction) and Z (thickness direction) with the first letter representing the loading direction and second letter the extension direction. (Kelley and Hosford, 1968a). | 16 |
| Figure 1.14 Tensile stress-strain curves for (a) pure magnesium, (b) Mg-Li, and (c) Mg-1Y alloys at room temperature (Agnew et al., 2006b). | 18 |
| Figure 1.15 Tensile stress-strain curves of extruded AZ61 for different tilt angles between extrusion direction and loading direction (Kleiner and Uggowitzer, 2004). | 19 |
| Figure 1.16 Stress-strain curves of (a) tension and (b) compression as a function of temperature (Jain and Agnew, 2007). | 20 |
| Figure 1.17 Schematic one dimensional representation of the linearization of strain rate against stress response in vicinity of the overall magnitudes $(\bar{\sigma}, \bar{D})$ for different types of interaction assumptions (Tomé, 1999). | 23 |
| Figure 2.1 Plastic deformation modes in hexagonal structure, (a) Basal; (b) Prismatic; (c) Pyramidal; and (d) extension Twin. | 40 |
| Figure 2.2 (a) Initial texture of the FCC polycrystal with 2000 grains in terms of $\{111\}$ pole figures, and (b) HCP polycrystal with 500 grains in terms of $\{0001\}$ pole figure. | 40 |
| Figure 2.3 Predicted shear stress - strain curves under simple shear (2.5.3) for the FCC polycrystal. | 41 |
| Figure 2.4 Predicted deformation textures in terms of the $\{111\}$ pole figure for the FCC polycrystal under simple shear (2.5.3) at shear strain of 2. | 42 |
| Figure 2.5 Predicted stress - strain curves under plane strain compression (2.5.2) for the FCC polycrystal. | 43 |
| Figure 2.6 Predicted deformation textures in terms of the $\{111\}$ pole figure for the FCC polycrystal under plane strain compression (2.5.2) at compressive strain of -1. | 43 |
| Figure 2.7 Predicted stress - strain curves under uniaxial tension (2.5.1) for the HCP polycrystal. | 44 |
| Figure 2.8 Predicted deformation texture in terms of the $\{0001\}$ pole figure for the HCP polycrystal under axisymmetric tension (2.5.1) at tensile strain of 0.5. | 45 |
| Figure 2.9 Predicted stress - strain curves under axisymmetric tension (2.5.1) for the HCP polycrystal. | 45 |
| Figure 2.10 Predicted stress - strain curves under plane strain compression (2.5.2) for the HCP polycrystal. | 46 |
| Figure 2.11 Predicted deformation textures in terms of the $\{0001\}$ pole figure for the HCP polycrystal under plane strain compression (2.5.2) at compressive strain of -0.5. | 46 |
| Figure 2.12 Predicted shear stress - strain curves under cyclic simple shear (2.5.3) for the HCP polycrystal. | 46 |

| | |
|---|----|
| Figure 2.13 Predicted effect of axisymmetric tension pre-straining (2.5.1) on subsequent plane strain tension (2.5.2) for the HCP polycrystal..... | 47 |
| Figure 2.14 Predicted stress - time curves for a stress relaxation test during axisymmetric compression (2.5.1) of the HCP polycrystal. | 48 |
| Figure 2.15 Predicted effect of Young's modulus E on stress responses for a stress relaxation test during axisymmetric compression (2.5.1) of the HCP polycrystal. | 48 |
| Figure 3.1 Initial texture of AZ31B sheet represented in terms of the $\{0001\}$ pole figure (a) and $\{10\bar{1}0\}$ pole figure (b)..... | 58 |
| Figure 3.2 Plastic deformation modes in hexagonal structure: (a) Basal $\langle a \rangle$ slip systems, (b) Prismatic $\langle a \rangle$ slip systems, (c) Pyramidal $\langle c + a \rangle$ slip systems, and (d) extension twin..... | 58 |
| Figure 3.3 Stress and strain curves under (a) uniaxial tension, and (b) uniaxial compression along the RD..... | 59 |
| Figure 3.4 Predicted slip/twinning activities for the sheet under uniaxial tension along the RD based on various polycrystal plasticity models. | 60 |
| Figure 3.5 Predicted slip/twinning activities for the sheet under uniaxial compression along the RD based on various polycrystal plasticity models..... | 60 |
| Figure 3.6 Deformed textures under uniaxial compression along the RD at strain of -0.11. | 61 |
| Figure 3.7 Stress and strain curves under (a) uniaxial tension, and (b) uniaxial compression along the TD..... | 62 |
| Figure 3.8 Deformed textures under uniaxial compression along the TD at strain $\varepsilon = -0.11$ | 62 |
| Figure 3.9 Stress and strain curves under uniaxial compression along the ND. | 63 |
| Figure 3.10 Predicted slip/twinning activities for the sheet under uniaxial compression along the ND based on various polycrystal plasticity models..... | 64 |
| Figure 3.11 R values under uniaxial tension within the sheet plane. Same results are plotted in different scales in (a) and (b)..... | 65 |
| Figure 3.12 Predicted R value vs. true plastic strain curves under uniaxial tension along the TD based on various polycrystal plasticity models. | 66 |
| Figure 3.13 Predicted R value vs. true plastic strain curves under uniaxial compression within the sheet plane based on Affine model..... | 67 |
| Figure 3.14 R values under uniaxial compression within the sheet plane. | 67 |
| Figure 3.15 R values under uniaxial compression along the ND. | 68 |
| Figure 3.16 Dependence of the fitted critical resolved shear stress (CRSS) ratios of Prismatic and Pyramidal slips to Basal slip on the grain interaction stiffness (different m^{eff} values). CRSS values determined from fits to experimental stress-strain curves and R values of slip-dominated strain paths. Corresponding ratios for Affine self-consistent scheme also depicted. | 68 |
| Figure 4.1 Initial texture of AZ31 bar represented in terms of the $\{0002\}$ and $\{10\bar{1}0\}$ pole distributions (Agnew et al., 2006a). | 77 |
| Figure 4.2 Stress-strain responses of AZ31 bar under uniaxial tension and compression along ED. The experimental data are taken from (Agnew et al., 2006a). | 77 |
| Figure 4.3 Simulated and experimental lattice strains along the axial direction under uniaxial tension. | 78 |
| Figure 4.4 Relative activity of the various deformation modes under uniaxial tension. | 79 |

| | |
|---|-----|
| Figure 4.5 Simulated and experimental relative intensities along the axial direction under uniaxial tension. The origin is shifted by 1 unit parallel to abscissa so as to avoid congestion..... | 79 |
| Figure 4.6 Simulated and experimental lattice strains along the transverse direction under uniaxial tension. | 80 |
| Figure 4.7 Simulated and experimental relative intensities along the transverse direction under uniaxial tension. The origin is shifted by 1 unit parallel to abscissa so as to avoid congestion. | 81 |
| Figure 4.8 Activity of various deformation modes under uniaxial compression. | 81 |
| Figure 4.9 Simulated and experimental lattice strains along the axial direction under uniaxial compression..... | 82 |
| Figure 4.10 Simulated and experimental relative intensities along the axial direction under uniaxial compression. The origin is shifted by 1 unit parallel to abscissa so as to avoid congestion. | 82 |
| Figure 4.11 Simulated and experimental lattice strains along the transverse direction under uniaxial compression..... | 84 |
| Figure 4.12 Simulated and experimental relative intensities along the transverse direction under uniaxial compression. The origin is shifted by 1 unit parallel to abscissa so as to avoid congestion. | 84 |
| Figure 4.13 Stress and strain curves under monotonic loading and loading with relaxation. | 85 |
| Figure 4.14 Simulated lattice strains along the transverse direction under uniaxial tension with relaxation and without relaxation (monotonic). | 86 |
| Figure 4.15 Simulated lattice strains along the axial direction under uniaxial tension with relaxation (a) at $\epsilon_{11} = 0.18$; and (b) lattice strain for the $\{1\bar{1}20\}$ diffraction plane under various strain levels..... | 86 |
| Figure 4.16 Effect of strain rate sensitivity m on the simulated lattice strains along the axial direction for the $\{1\bar{1}20\}$ diffraction plane under uniaxial tension with relaxation at $\epsilon_{11} = 0.18$... | 87 |
| Figure 4.17 Stress and strain curves under uniaxial tension and compression with creep and without creep (monotonic). | 87 |
| Figure 4.18 Simulated lattice strains along the axial direction under uniaxial tension with creep (a) at $\sigma_{11} = 235$ MPa; and (b) lattice strain for the $\{10\bar{1}1\}$ diffraction plane under various stress levels..... | 88 |
| Figure 4.19 Effect of creep on the predicted lattice strains under uniaxial tension..... | 89 |
| Figure 4.20 Effect of creep on the predicted lattice strains under uniaxial compression..... | 90 |
| Figure 4.21 Simulated lattice strains along the axial direction under uniaxial tension with relaxation or creep at $\sigma_{11} = 235$ MPa..... | 91 |
| Figure 5.1 The geometry and convention employed in the FLD analysis..... | 98 |
| Figure 5.2 Plastic deformation modes in hexagonal structure: (a) Basal $\langle a \rangle$ slip systems, (b) Prismatic $\langle a \rangle$ slip systems, (c) Pyramidal $\langle c + a \rangle$ slip systems, and (d) extension twin. | 100 |
| Figure 5.3 Initial textures represented in terms of the $\{0001\}$ and $\{10\bar{1}0\}$ pole figures. | 100 |
| Figure 5.4 The intensity of basal texture as a function of tilted angle α | 102 |
| Figure 5.5 True stress and plastic strain curves under uniaxial tension/compression along the RD. The experimental data are taken from Jain and Agnew (2007)..... | 103 |

| | |
|--|-----|
| Figure 5.6 Predicted forming limit diagrams for the reference sheet based on various polycrystal plasticity models..... | 104 |
| Figure 5.7 Predicted critical groove orientations for the reference sheet based on various polycrystal plasticity models. | 104 |
| Figure 5.8 Influence of the material rate sensitivity parameter m on the predicted FLDs for the reference sheet based on the Affine model..... | 105 |
| Figure 5.9 Influence of texture evolution on the predicted FLDs for the reference sheet based on the Affine model..... | 106 |
| Figure 5.10 Influence of initial texture on the predicted FLDs based on the Taylor model..... | 106 |
| Figure 5.11 Influence of initial texture on the predicted FLDs based on the Affine model..... | 107 |
| Figure 5.12 Influence of initial texture on the predicted FLDs based on the meff model..... | 107 |
| Figure 5.13 Predicted critical groove orientations for the initial texture rotated 45° around TD based on various polycrystal plasticity models. | 108 |
| Figure 5.14 Influence of basal texture on the predicted limit strain under in-plane plane strain tension ($\rho = 0$). | 108 |
| Figure 5.15 Predicted FLDs for the reference sheet pre-strained to different levels in uniaxial tension ($\rho = -0.5$) based on the Affine model..... | 109 |
| Figure 5.16 Predicted FLDs for the reference sheet pre-strained to different levels in in-plane plane strain tension ($\rho = 0$) based on the Affine model..... | 109 |
| Figure 5.17 Predicted FLDs for the reference sheet pre-strained to different levels in equi-biaxial tension ($\rho = 1$) based on the Affine model..... | 110 |
| Figure 5.18 Predicted limit stresses for the reference sheet pre-strained in various different pre-straining paths indicated by different symbols based on the Affine model..... | 110 |

Table of Tables

| | |
|--|-----|
| Table 1.1 Crystallographic data for some HCP metals (Partridge, 1967). | 3 |
| Table 1.2 Independent slip systems in HCP metals (Partridge, 1967). | 5 |
| Table 1.3 CRSS values reported for magnesium and its aluminum-zinc-manganese alloys. | 17 |
| Table 3.1 List of material constants for various self-consistent models..... | 58 |
| Table 4.1 Values of the material parameters for the slip and twin systems used in the EVPSC model. The parameter h^t lists latent hardening effect of twinning activity upon the other deformation modes. All other latent hardening parameters in Eq. 4.4 are 1. | 77 |
| Table 5.1 List of values of material constants for various polycrystal plasticity models..... | 100 |

Chapter 1. General introduction

1.1 Background

The interest on magnesium and its alloys started before World War II. In the two decades after the war, magnesium alloys was enhanced by varying the additions from aluminum, zinc and tin to the rare earth elements. These alloys have been used in both wrought and cast applications. For the next forty years, the development of magnesium alloys almost ceased while the development of wrought aluminum-based alloys boomed (Bettles and Gibson, 2005). In recent years, the interest on magnesium alloys has been revived mainly due to the current pressure to reduce green house gas emissions from the transportation sector through vehicle weight reduction. On average magnesium materials are 35% lighter than aluminum alloys and 80% lighter than steels per volume. Therefore, the North American automobile industry has set an objective to reduce vehicle weight by substitution of components typically made of aluminum or steel with magnesium. For example, a 10-15% weight saving yields 10-15% fuel savings, which further reduces 10-15% the greenhouse gas emissions. In addition to the primary advantage of light weight, a number of other attributes such as high specific strength, high die casting rates, electromagnetic interference shielding properties, parts consolidation, dimensional accuracy, good corrosion performance, and excellent machinability (Mordike and Ebert, 2001) make magnesium alloys more attractive.

Use as a structural material is one main application of magnesium alloys. In this case, the major inhibiting factor may be the hexagonal close packed (HCP) crystal structure. It has an axial ratio, $c/a=1.624$, slightly smaller than the theoretical value for incompressible sphere model, 1.633, thereby restricting the number of deformation slip and twinning modes at ambient temperature. At elevated temperatures, many more slip planes are easily activated and extensive deformation is possible. Therefore, pure magnesium and some of its alloys exhibit poor ductility at ambient temperatures but excellent ductility at elevated temperatures. Improving the ductility of magnesium and its alloys at lower temperatures is necessary to establish the application of magnesium alloys commercially. It is suggested that an appropriate alloying solution, such as zirconium, refinement of the grain size via some severe plastic deformation processing technique, and texture control may significantly increase the performance of magnesium and its alloys (Bettles and Gibson, 2005; King, 2007).

It is no doubt that magnesium has been increasingly taken into consideration in various areas where weight savings are crucial. Japan, Germany, and the UK have proposed their own roadmaps for development and applications of magnesium (Kojima, 2000; Potzies et al., 2003; King, 2005). However, knowledge of aluminum and steel is far more advanced than that of magnesium. To utilize magnesium and its alloys more effectively requires an understanding of the behaviour of magnesium in alloying

aluminum, iron and steel processing, and as a structural material. Thereafter, establishing the application of magnesium commercially will be possible. Based on acquired knowledge from appropriate constitutive modeling in materials such as aluminum and steel, it has been established that it is an important and necessary step in building up the knowledge of magnesium and its alloys. As a result, this thesis considers the constitutive modeling of magnesium and its alloys.

Each chapter of this thesis, except for this chapter and the last chapter, is an independent paper, which has been published or submitted, or is to be submitted to an international journal for publication. However, a uniform layout and referring system will be used throughout the thesis, with all references collected at the end.

1.2 Crystallography of HCP metals

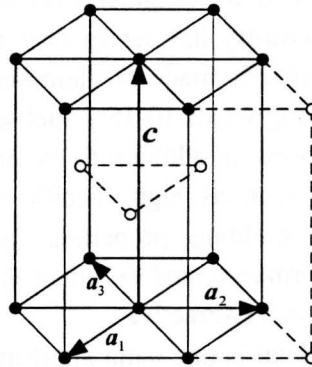


Figure 1.1 The hexagonal close packed unit cell.

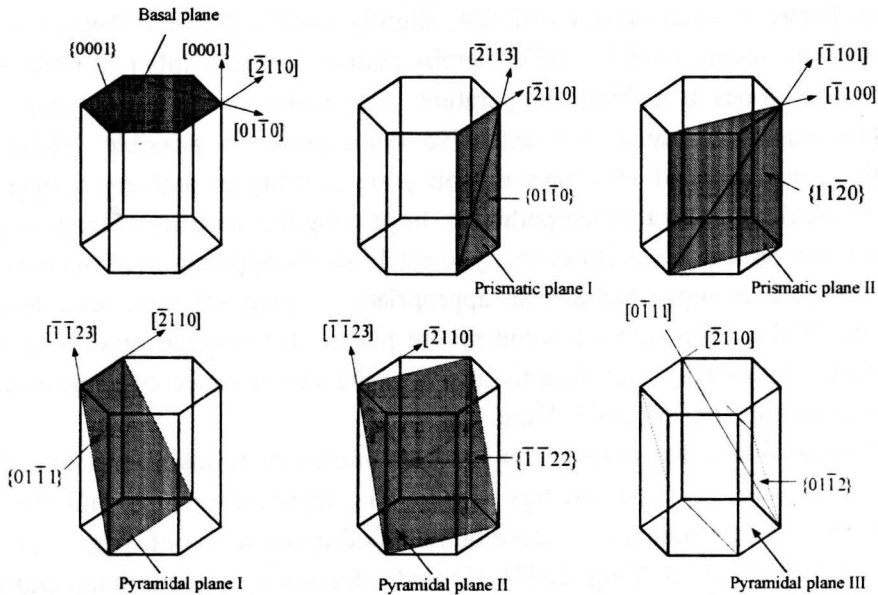


Figure 1.2 Important planes and directions in the hexagonal system (Patridge, 1967).

The crystallography of HCP metals has been thoroughly discussed by Partridge (1967). As shown in **Figure 1.1**, the primitive hexagonal unit cell consists of the axes a_1 , a_2 , a_3 and c with $|a_1| = |a_2| = |a_3| = a$ and $|c| = c$ ($a \neq c$). The angles between a_1 , a_2 and a_3 are equally 120° , while the angles between a_i ($i=1,2,3$) and c are equally 90° . The hexagonal symmetry in the lattice is usually illustrated by means of the hexagonal prism (solid lines in **Figure 1.1**). The atom positions in the HCP structure are at the lattice points and at coordinates $(1/3, 0, -1/3, 1/2)$, $(1/3, -1/3, 0, 1/2)$, and $(0, 1/3, -1/3, 1/2)$ as shown in **Figure 1.1**, where the Miller-Bravais indices based on a_1 , a_2 , a_3 and c have been used. The following notations are used for representing the Miller-Bravais indices for the HCP structure: crystallographic equivalent planes are represented as $\{ \}$, single directions are represented as $[]$ and crystallographic equivalent directions are represented as $\langle \rangle$. **Figure 1.2** gives the important planes and directions.

If the atoms (spheres in **Figure 1.1**) are assumed to be incompressible spheres in contact with each other, then the structure is considered to be ideal with a coordination number (i.e. the number of nearest-neighbour atoms) of twelve and a c/a ratio of $\sqrt{8/3} = 1.633$. Though none of the pure HCP metals exhibit this ideal c/a ratio, magnesium and cobalt are quite close (**Table 1.1**). The interplanar spacing is the distance between the planes of the same set. For example, the interplanar spacing of $\{0001\}$ is $c/2$. If c/a is greater than the ideal value (e.g. cadmium and zinc), each atom of the metals has 6 nearest neighbours in the basal plane and 3 nearest neighbours above and below the basal plane at slightly greater distances. The $\{10\bar{1}0\}$ planes have the smallest interplanar spacing for these metals. If c/a is less than the ideal value (e.g. magnesium and zirconium), each atom has the 3 nearest neighbours above and below at slightly closer distances than those in the basal planes. The $\{0001\}$ planes have the smallest interplanar spacing for these metals.

Table 1.1 Crystallographic data for some HCP metals (Partridge, 1967).

| Metal | a | c | c/a | Ratio of interplanar spacings $d_{\{10\bar{1}0\}}/d_{\{0002\}}$ |
|-------|-------|-------|--------|---|
| Cd | 2.972 | 5.605 | 1.8859 | 0.918 |
| Zn | 2.659 | 4.936 | 1.8563 | 0.933 |
| IDEAL | ---- | ---- | 1.6330 | 1.061 |
| Co | 2.502 | 4.061 | 1.6230 | 1.067 |
| Mg | 3.203 | 5.200 | 1.6230 | 1.067 |
| Re | 2.760 | 4.458 | 1.6150 | 1.072 |
| Zr | 3.231 | 5.147 | 1.5930 | 1.087 |
| Ti | 2.950 | 4.683 | 1.5873 | 1.091 |
| Hf | 3.194 | 5.051 | 1.5810 | 1.095 |
| Be | 2.281 | 3.576 | 1.5680 | 1.105 |

1.3 Deformation of HCP metals

The crystallography of HCP metals affects both their elastic and plastic behaviors. In this section, the elastic anisotropy and possible slip and twinning systems will be discussed.

1.3.1 Elastic behavior

To completely describe the elastic behavior, five independent elastic constants are required due to the symmetry of HCP structure. This behavior is shown in the following equation:

$$\begin{bmatrix} \sigma_{11} \\ \sigma_{22} \\ \sigma_{33} \\ \sigma_{23} \\ \sigma_{13} \\ \sigma_{12} \end{bmatrix} = \begin{bmatrix} C_{11} & C_{12} & C_{13} & 0 & 0 & 0 \\ C_{12} & C_{11} & C_{13} & 0 & 0 & 0 \\ C_{13} & C_{13} & C_{33} & 0 & 0 & 0 \\ 0 & 0 & 0 & C_{44} & 0 & 0 \\ 0 & 0 & 0 & 0 & C_{44} & 0 \\ 0 & 0 & 0 & 0 & 0 & (C_{11} - C_{12})/2 \end{bmatrix} \begin{bmatrix} \varepsilon_{11} \\ \varepsilon_{22} \\ \varepsilon_{33} \\ 2\varepsilon_{23} \\ 2\varepsilon_{13} \\ 2\varepsilon_{12} \end{bmatrix} \quad (1.1)$$

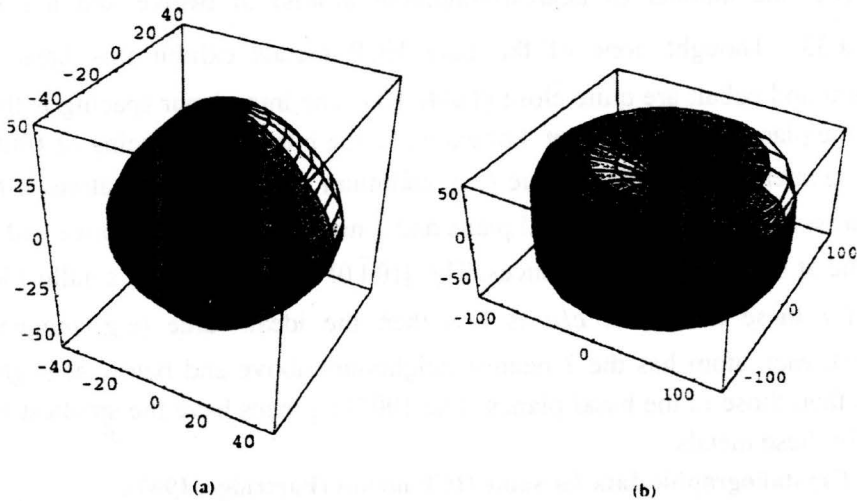


Figure 1.3 Anisotropy of Young's modulus in (a) magnesium and (b) zinc (Schmid and Boas, 1950).

The left hand side of equation 1.1 is the stress vector. The right hand side is the product of elastic stiffness tensor and strain vector. For an isotropic material, one would have $C_{11}=C_{33}=\lambda+2\mu$, $C_{12}=C_{13}=\lambda$, $C_{44}=\mu$, where $\lambda=E\nu/(1+\nu)(1-2\nu)$ and $\mu=E/2(1+\nu)$ are the Lamè constants in terms of Young's modulus E and Poisson's ratio ν . The elastic stiffness tensor in (1.1) shows that all HCP metals are elastically isotropic in the basal plane; however, the elastic properties perpendicular to the basal plane can vary considerably from those parallel to it, resulting a pronounced elastic anisotropy. Therefore, a single grain's deformation depends strongly on the orientation of its

crystallographic axes with respect to the direction of the applied stress. If a polycrystalline aggregate is considered, it is expected that the elastic behavior exhibited will depend on the degree of preferred orientation in the material. **Figure 1.3** shows how the modulus of elasticity varies with crystallographic direction in magnesium and in zinc. It is clearly illustrated that the degree of elastic anisotropy can vary considerably between materials.

1.3.2 Deformation slip

One plastic deformation mechanism in HCP materials is slip. The slip will be activated when the applied resolved shear stress acting on the slip plane reaches a critical value known as the critical resolved shear stress (CRSS). Deformation by slip arises on an individual slip plane, where atomic displacements on each plane can ultimately be much larger than lattice spacing. Slip deformation induces gradual crystal reorientation, and reverses its deformation direction when stress is applied in the opposite direction.

Table 1.2 Independent slip systems in HCP metals (Partridge, 1967).

| Slip system | Burgers vector type | Slip direction | Slip plane | No. of slip systems | |
|-------------|---------------------|------------------------------|------------------|---------------------|-------------|
| | | | | Total | Independent |
| 1 | <i>a</i> | $\langle 11\bar{2}0 \rangle$ | {0001} | 3 | 2 |
| 2 | <i>a</i> | $\langle 11\bar{2}0 \rangle$ | {10 $\bar{1}$ 0} | 3 | 2 |
| 3 | <i>a</i> | $\langle 11\bar{2}0 \rangle$ | {10 $\bar{1}$ 1} | 6 | 4 |
| 4 | <i>c+a</i> | $\langle 11\bar{2}3 \rangle$ | {11 $\bar{2}$ 2} | 6 | 5 |
| 5 | <i>c</i> | $\langle 0001 \rangle$ | {10 $\bar{1}$ 0} | 3 | 2 |
| 6 | <i>c</i> | $\langle 0001 \rangle$ | {11 $\bar{2}$ 0} | 3 | 2 |

A slip system is defined by its Burgers vector and slip plane normal. The important Burgers vector in the HCP metals can be described by the bi-pyramidal shown in **Figure 1.4**. The shortest Burgers vectors of type *a* are associated with the three glide directions *AB*, *BC* and *AC*. These vectors lay in the close-packed directions and are coplanar in the basal plane. The slip systems associated with these Burgers vectors are easily activated due to the relatively low CRSS. Another two important Burgers vectors include *c* and *c+a*, which are associated with the glide direction *ST* and *ST+AB*, respectively. They do not lie in a close-packed direction. Therefore slip systems associated with these Burgers vector require more energy to be activated due to their relatively high CRSS values. The six types of slip systems which have been observed in HCP metals are listed in **Table 1.2**. Slip systems of type 1 and 2 would yield a total of four independent slip systems, equivalent to those offered by type 3 (Groves and Kelley, 1963). In addition, slip systems of type 1, 2 or 3 cannot accommodate deformation along the *c* direction since they all involve $\langle 11\bar{2}0 \rangle$ slip directions, which are normal to the *c*

axis. The Taylor criterion (Taylor, 1938) requires the activation of five independent easy slip systems to accommodate an arbitrary shape change in a crystal material. As a result, at least one slip system of type 4, 5, or 6 must be activated to satisfy the requirement for an arbitrary strain to occur.

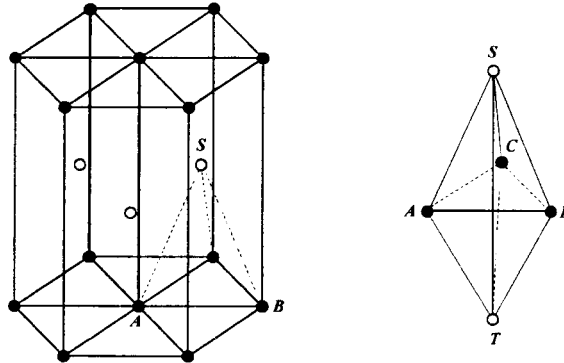


Figure 1.4 Bi-pyramidal construction for the HCP lattice (Berghezan et al., 1961).

Poirier and Le Hazif (1976) have studied the slip systems in HCP metals based on transmission electron microscopy. They indicated that each HCP metal has a primary slip system which is easily activated as well as one or more secondary systems which have a significantly higher CRSS. The primary system is either $\{0001\}\langle 11\bar{2}0 \rangle$ (or basal $\langle a \rangle$) or $\{10\bar{1}0\}\langle 11\bar{2}0 \rangle$ (or prismatic $\langle a \rangle$). Some metals (e.g. cadmium, zinc, magnesium) have $\{0001\}\langle 11\bar{2}0 \rangle$ as the primary system (Schmid and Boas, 1950), and some others (e.g. zirconium, titanium) have $\{10\bar{1}0\}\langle 11\bar{2}0 \rangle$ as the primary system (Churchman, 1954; Rapperport, 1959). However, the stress strain curves and the dislocation configurations are very similar, whether the principal system is basal or prismatic. The $\{11\bar{2}2\}\langle 11\bar{2}\bar{3} \rangle$ (or second-order pyramidal $\langle c+a \rangle$) is believed to be the easiest secondary slip system, and commonly observed in some HCP metal, e.g. cadmium, zinc (Yoo and Wei, 1967). More details concerning slip in magnesium will be discussed in Section 1.4.

1.3.3 Deformation twinning

In addition to slip, twinning is another important deformation mechanism in HCP materials. Based on some review work (Cahn, 1954; Patridge, 1967; Mahajan and Williams, 1973), this section will briefly review some features in mechanical twinning, especially twinning in HCP material.

In contrast to slip, twinning involves a homogeneous shear evenly distributed over a portion of the lattice such that the lattice orientation in the twinned region is a mirror image of that of the matrix. The plastic strain is therefore accommodated by translation of a section of a crystal relative to another across a single twinning plane by an amount which is a multiple of Burgers vector. In addition, a twinning system can only activate in

one direction, which is known as polarization. Twinning results in a sudden reorientation of the crystal lattice, whereas slip causes a much more gradual reorientation.

As shown in Figure 1.5, a twin is usually described by four elements: the first undistorted plane (twin plane) K_1 , the direction of shear η_1 , the second undistorted plane K_2 , and η_2 . The twin plane K_1 , is identical in both the twin and matrix systems and is unchanged by the shear. The shear direction η_1 , is the direction where twinning occurs and lies in the plane K_1 . The plane containing η_1 and the normal to K_1 is defined as the plane of shear S . The second undistorted plane K_2 , rotates to K'_2 by twinning, and is unchanged both in shape and size. K_2 and K'_2 intersect K_1 and make angles of θ with K_1 during twinning. The intersection of S and K_2 (K'_2) is denoted as η_2 (η'_2).

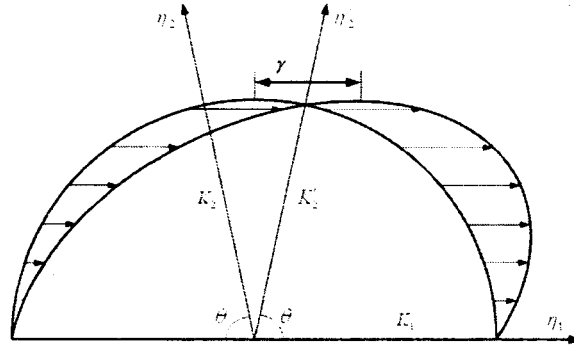


Figure 1.5 Crystallographic elements of twinning.

The magnitude of twinning shear, γ , is given by

$$\gamma = 2 \cot \theta \quad (1.2)$$

The homogeneously simple shear of matrix lattice does not produce a true mirror configuration with respect to K_1 . As a result, cooperative atom movement is induced so that atoms which are out of position move to form the mirror arrangement. This atom movement is generally small and called shuffle which is necessary in addition to the simple shear, to retain the same crystal lattice in twins as in matrix.

There are four types of twinning modes commonly observed in HCP metals. They are $\{10\bar{1}2\} \langle 10\bar{1}\bar{1} \rangle$, $\{10\bar{1}1\} \langle 10\bar{1}\bar{2} \rangle$, $\{11\bar{2}2\} \langle 11\bar{2}\bar{3} \rangle$, and $\{11\bar{2}1\} \langle \bar{1}\bar{1}26 \rangle$ (Yoo, 1981). The magnitude of twinning shear for each mode is determined by axial ratio c/a (Mathewson and Phillips, 1928). The most predominant twinning mode is $\{10\bar{1}2\} \langle 10\bar{1}\bar{1} \rangle$, which operates in all HCP metals. The elements of this twinning mode are illustrated in Figure 1.6, where the twinning plane K_1 is $\{10\bar{1}2\}$, twinning direction η_1 is $\langle 10\bar{1}\bar{1} \rangle$, and the plane of shear S is $\{11\bar{2}0\}$. Second undistorted plane K_2 and direction η_2 are crystallographically equivalent to K_1 and η_1 . The shear magnitude of this twinning mode is expressed as

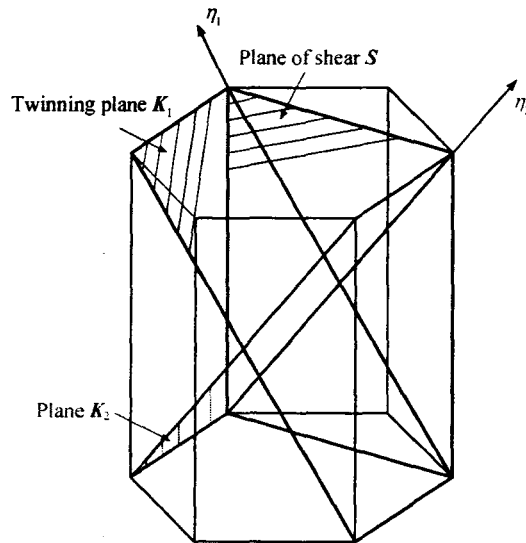


Figure 1.6 Twinning elements of twinning mode $\{10\bar{1}2\} \langle 10\bar{1}\bar{1} \rangle$.

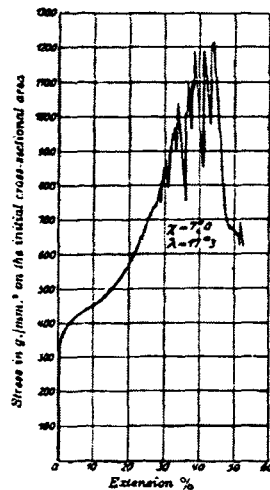


Figure 1.7 Stress-strain curve of a cadmium single crystal. Each serration corresponds to the formation of a twin (Schmid and Boas, 1950).

$$\gamma = \frac{3 - (c/a)^2}{\sqrt{3} c/a} \quad (1.3)$$

From (1.3), the twinning shear becomes zero when $c/a = \sqrt{3}$ at which no twin can be formed. If $c/a < \sqrt{3}$ as in magnesium, zirconium and titanium, the twinning mode activates under an extension stress along the c direction. Therefore, it is called "extension" twin, which elongates the c -axis. Vice versa, if $c/a > \sqrt{3}$ as in cadmium and zinc, "contraction" twin operates under a compressive stress along the c direction. It is worth mentioning that the twinning shear magnitude is small, varying from -0.175 for

cadmium with $c/a=1.89$ to 0.186 for beryllium with $c/a=1.57$. In magnesium, this type of twinning results in a shear of 0.129 and a lattice reorientation of approximately 87° .

Deformation twins convert portion of the grain into the twin orientation. The formed twins consist of thin lenticular plates separated by the parent material. The shape of deformation may be attributed to the overall change in energy as the twin forms. One of the main energy changes is the surface energy associated with the formation of the twin boundary. This energy is minimized when the aspect ratio (ratio of length to thickness) is unity (a sphere shape). Another main energy change is strain energy due to inhomogeneous plastic deformation in the twinned and untwinned regions. The mismatch between the twins and the matrix must be accommodated by elastic distortion of the parent and/or slip in the parent phase. This energy is minimized when the aspect ratio of the twins is the highest. Therefore, the final shape of the twin will depend on the relative magnitudes of the surface energy and strain energy.

As shown in **Figure 1.7**, deformation twins form over a small increment of deformation and can produce sharp load drops in a tensile test. Each serration in the stress-strain curve corresponds to the formation of a twin. It is ambiguous as to which yield criterion is appropriate for twinning. Most analytical studies assume a CRSS criterion. However some investigations have questioned the soundness of such a criterion. Uncertainties from the shear stress criterion may be due to the prerequisite slip to nucleate twinning or to the dependence of the stress normal to the twin plane as well as the resolved shear stress. This could be particularly important for twinning in HCP metals in which the atoms do not all move in the direction of the shear but have a component of their displacement normal to the twin plane. Bell and Cahn (1957) observed a large scatter in CRSS of zinc single crystals and sensed that there is no single CRSS existing for twinning. A possible explanation for their observation is that the scatter is caused by stress concentration from surface notches, internal defects, etc. (Meyers et al., 2001). It has been extensively reported that twinning occurs on the system with the highest resolved shear stress for many materials (Thompson and Millard, 1952; Chin et al., 1969; Gharghoury et al., 1999). Therefore, the CRSS criterion for twinning is used in this study.

It is important to recognize that the stresses for twin nucleation and for twin growth may be very different. Usually, a much higher stress is required to nucleate a twin than to propagate a twin. As a twin is nucleated, its surface to volume ratio is very high and the work required to generate the surface must come from the mechanical work expended, which is the product of required shear stress, twinning shear (constant) and volume of the twinning region. A high surface to volume ratio will induce a high required shear stress (Hosford, 1993). Therefore, a fine grain size or a second phase within the grains which cannot be easily sheared by the twins, will result in a higher shear stress for nucleation. Other metallurgical conditions like temperature, strain rate, pre-strain and

precipitates, which may affect the twin nucleation and growth have been thoroughly reviewed by Christian and Mahajan (1995). They have observed that the actual magnitude of the twinning stress changes rather slowly with temperature but is very sensitive to the strain rate. Experimental evidence showed that twinning in iron (Altshuler and Christian, 1966), niobium (Boucher and Christian, 1972) and chromium (Marcinkowski and Lipsitt, 1962) can be suppressed by a pre-strain at higher temperature.

Mahajan and Williams(1973) have inferred that slip was favored by more mobile dislocations produced in pre-straining during the competition of twinning and slip. The interpretation indicates that reducing the density of mobile dislocations increases the capability to twin. The effect of precipitates on twinning is similar, because they facilitate slip (Chun et al., 1969).

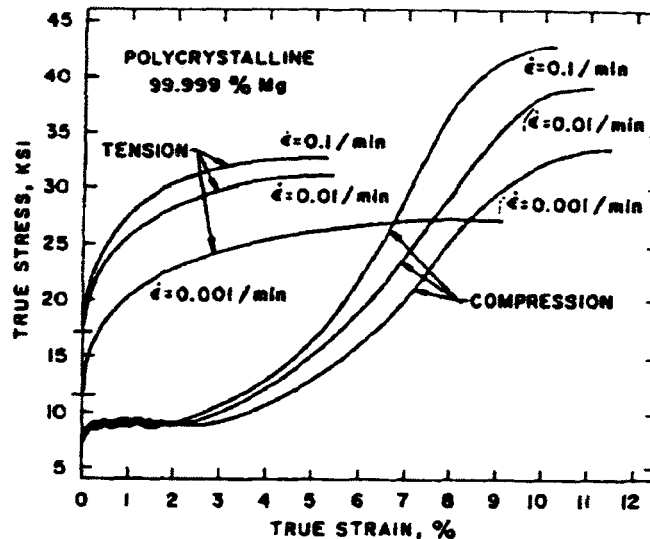


Figure 1.8 Effect of texture on the stress-strain curves of highly textured pure magnesium (Reed-Hill, 1973).

In a polycrystalline material, the grain size and texture can have a profound influence on the formation and growth of twins. Finer grain sizes diminish the serrations of the macroscopic stress-strain curves caused by twins and require higher average stress to nucleate twins. Twins formed in fine-grained materials are smaller. As a consequence, the relaxation caused by the deformation of a twin, results in an insignificant load drop compared to the load drop in a single crystal. Fine twins can form at grain boundaries of a fine-grained material which relax intergranular stresses that occur as a result of intergranular incompatibility.

In a textured material, a strong anisotropy of flow curves for tension and compression maybe observed due to the polarization of twinning. As shown in Figure 1.8, the extruded magnesium has a strong texture, with the basal poles oriented preferentially in a plane normal to the extrusion axis and the stress is applied in the extrusion direction.

In compression, $\{10\bar{1}2\} \langle 10\bar{1}1 \rangle$ twins are active which result in a plateau in the stress-strain curves. However, in tension, no twinning is active and the stress-strain curves are very different to those for compression.

To summarize, a large variety of deformation modes are possible in HCP metals. At least one non-basal slip mode with a c -component Burgers vector is required to accomplish the five independent slip modes necessary to accommodate arbitrary homogeneous deformation. Twinning can provide significant plastic deformation but may be restricted to particular stress condition due to its polar nature, if the material has a pronounced texture.

1.4 Deformation of Magnesium

The elastic constants for magnesium and its alloys have been collected by Simmons and Wang (1971). The elastic behavior is close to isotropic because the anisotropic ratios $C_{11}/C_{33} \approx 0.96$, $C_{66}/C_{44} \approx 0.98$ are both close to 1. Therefore, the elastic behavior is also often described by Young's modulus $E = 45$ GPa and shear modulus $G = 17$ GPa.

This section will briefly review the deformation mechanisms which can occur in magnesium and its alloys and the factors which affect them.

1.4.1 Plastic deformation of pure magnesium

Experimental works on pure magnesium single crystals at room temperature (Burke and Hibbard, 1952) have successfully isolated basal $\langle a \rangle$ slip $\{0001\} \langle 11\bar{2}0 \rangle$ from other slip modes. This has been accomplished by controlling the angle between basal plane and tensile axis to values between 6° and 72° , to keep the Schmid factor for basal $\langle a \rangle$ slip high and that for the others low. The CRSS for basal $\langle a \rangle$ slip was calculated about 0.46MPa.

Non-basal slip has been studied by deforming magnesium single crystal at -190°C , 25°C , 150°C and 286°C in tension (Reed-Hill and Robertson, 1957b; 1958). With the tensile axis oriented $2 \pm 1^\circ$ from a $\langle 10\bar{1}0 \rangle$ direction to suppress basal slip and $\{10\bar{1}2\} \langle 10\bar{1}1 \rangle$ twinning. Prismatic $\langle a \rangle$ slip $\{10\bar{1}0\} \langle 11\bar{2}0 \rangle$, accompanied with cross-slip on basal planes, was found to be dominant at -190°C . Prismatic-basal cross-slip was observed in the extremely strained region close to fracture. In the cases where the tensile axis inclined at 85° to the $\langle 0001 \rangle$ direction, and 18° to the $\langle 10\bar{1}0 \rangle$ direction, pyramidal $\langle a \rangle$ slip $\{10\bar{1}1\} \langle 11\bar{2}0 \rangle$ was observed at a test temperature of 25°C near fillets, grips, and fractures in the single crystals. However, it is unlikely that pyramidal $\langle a \rangle$ slip provides a large amount of plastic deformation at room temperature because the specimen preferentially oriented for pyramidal slip showed negligible ductility.

As discussed earlier, at least five independent slip systems are required for an arbitrary deformation to occur. The basal and non-basal $\langle a \rangle$ slips mentioned above can provide a total of four independent slip systems, which cannot accommodate deformations along the c -axis. Therefore, slip systems with the non-basal Burgers vectors $\langle c \rangle$ or $\langle c+a \rangle$ are required to provide the additional independent slip systems. The second order pyramidal $\langle c+a \rangle$ slip has been observed experimentally in the c -axis compression of magnesium single crystal in the temperature range of 77K to 450K (Stohr and Poirier, 1972). The CRSS for non-basal slip modes are two orders of magnitude higher than that for basal $\langle a \rangle$ slip (Kelley and Hosford, 1968b).

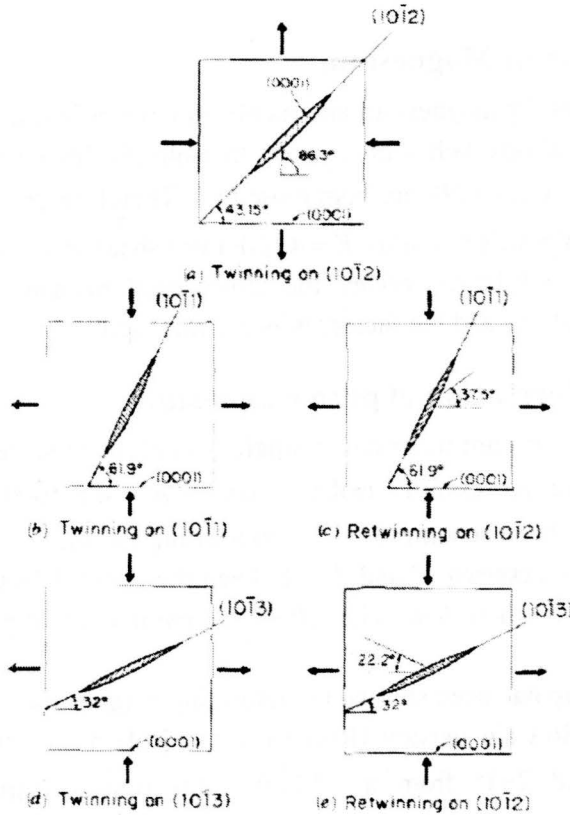


Figure 1.9 Some details of twinning in magnesium (a) Twinning on $\{10\bar{1}2\}$ occurs in tension perpendicular or compression parallel to the $\{0001\}$ basal plane and reorients the basal plane through 86.3° . (b) Under an opposite system of loading, a $\{10\bar{1}1\}$ twin can form and then retwin (c) on $\{10\bar{1}2\}$. A similar double twinning processes, (d)-(e), can occur on a $\{10\bar{1}3\}$ plane (Wonsiewicz and Backofen, 1967).

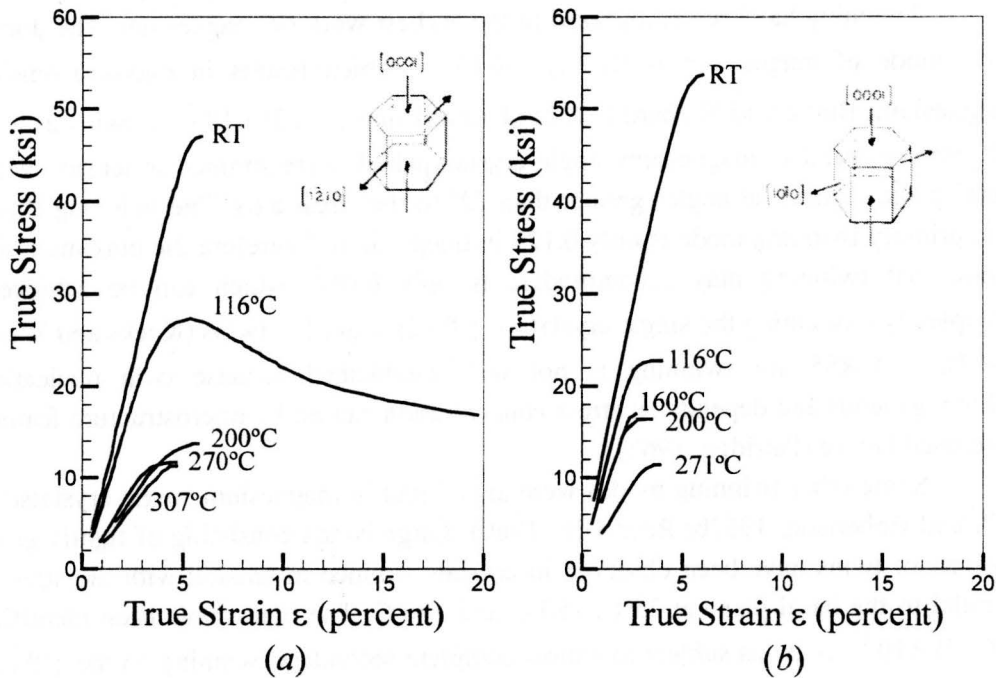


Figure 1.10 Stress-strain curves for magnesium crystals compressed along $\langle 0001 \rangle$ with expansion limited to (a) $\langle 1\bar{2}10 \rangle$ and (b) $\langle 10\bar{1}0 \rangle$ (Wonsiewicz and Backofen, 1967).

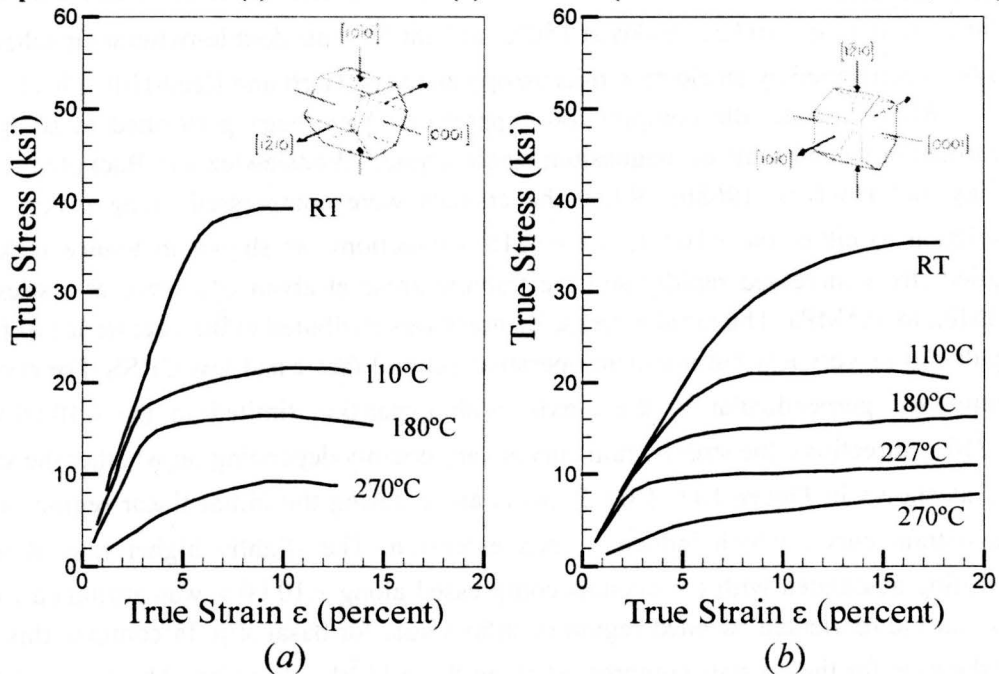


Figure 1.11 Stress-strain curves for magnesium crystals compressed along (a) $\langle 11\bar{2}0 \rangle$ and (b) $\langle 10\bar{1}0 \rangle$ with expansion limited parallel to the $\langle 0001 \rangle$ direction (Wonsiewicz and Backofen, 1967).

Twinning has been recognized in the earliest work on magnesium. The dominant twin mode of magnesium is $\{10\bar{1}2\} \langle 10\bar{1}1 \rangle$, which results in *c*-axis extension in magnesium. Burke and Hibbard (1952) observed fine $\{10\bar{1}2\} \langle 10\bar{1}1 \rangle$ twins as a result of grip constraint in magnesium single crystals which were strained in tension with the basal plane inclined at angles greater than 72° to the stress axis. The twinning shear for this primary twinning mode is only 0.129 in magnesium. Therefore the maximum tensile strain that twinning may accommodate is only 0.064, which can be achieved by completely reorienting the single crystal by $\{10\bar{1}2\} \langle 10\bar{1}1 \rangle$ twins (Kocks and Westlake, 1967). A CRSS for twinning is not well established because twin nucleation is inhomogeneous and depends on stress concentration caused by microstructure feature, as discussed before (Patridge, 1967).

Some other twinning modes were also found in magnesium single crystals (Reed-Hill and Robertson, 1957b; Reed-Hill, 1960). Large bands consisting of tightly grouped clusters of twins have been observed in crystals strained in tension with the stress axis parallel to the basal plane at 25°C , 150°C and 286°C . The twins have been identified as $\{10\bar{1}1\} \langle 10\bar{1}2 \rangle$ twins subject to almost complete secondary twinning on the $\{10\bar{1}2\}$ of the first order twin. The mechanism of the primary and secondary twinning is illustrated in **Figure 1.9**. Small $\{10\bar{1}3\}$ twins were observed near the region of fracture and in the vicinity of $\{10\bar{1}1\} \langle 10\bar{1}2 \rangle$ twins at 150°C and 286°C . This double-twinning mechanism has been confirmed by an electron microscopy analysis (Hartt and Reed-Hill, 1967).

Many channel die compression experiments have been performed to study the deformation mechanisms of magnesium single crystal (Wonsiewicz and Backofen, 1967; Kelley and Hosford, 1968b). When the crystals were compressed along *c*-axis, with restriction to either the $\langle 10\bar{1}0 \rangle$ or $\langle 1\bar{2}10 \rangle$ directions, as shown in **Figure 1.10**, the applied stress increased rapidly and the fracture arose at about 6% strain at a stress of 324MPa to 365MPa. The rapid increase in stress was attributed to the occurrence of basal slip due to its very low but non-zero operative Schmid factor and low CRSS. For crystals compressed perpendicular to the *c*-axis, with expansion limited to the $\langle 10\bar{1}0 \rangle$ or $\langle 1\bar{2}10 \rangle$ directions, the stress-strain curves vary notably depending on whether the stress axis as shown in **Figure 1.11**. $\{10\bar{1}2\}$ twins arose during the initial linear region of the stress-strain curve, which induced *c*-axis extension. The slightly higher rate of work hardening associated with the crystals compressed along $\langle 10\bar{1}0 \rangle$ was attributed to the fact that the reoriented twinned region is unfavorable for basal slip. In contrast, this was not the case for the crystals compressed along the $\langle 11\bar{2}0 \rangle$ direction. The larger plateau regions of the stress-strain curves were associated with the appearance of double twinning which proceeded to relieve the *c*-axis expansion generated by $\{10\bar{1}2\}$ twinning.

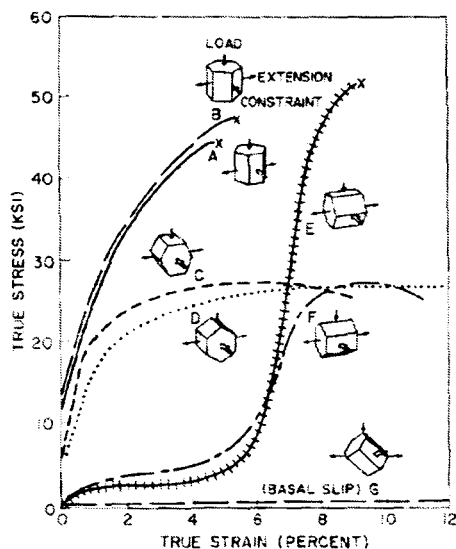


Figure 1.12 Stress-strain curves for pure magnesium under channel die compression (Kelley and Hosford, 1968b).

The stress-strain curves (Figure 1.12) for pure magnesium under channel die compression have also been carried out by Kelley and Hosford (1968b), which evidently showed that the stress-strain behaviour depends strongly on the compression and constraint directions. The results agreed well with those of Wonsiewicz and Backofen (1967) for cases where the same loading conditions and constraints were applied. In addition, the compression of the single crystals perpendicular to the c -axis with expansion limited to the $\langle 0001 \rangle$ direction (orientations E and F in Figure 1.12) have been carried out by Kelley and Hosford. In these cases, the primary twinning mode $\{10\bar{1}2\}$ proceeded and completed to about 6% strain. It is interesting to note that after the twinning, orientation E was only about 3.7° from orientation B and subsequently deformed as described for this orientation according to Wonsiewicz and Backofen. For orientation F, the twinned material was favourably oriented for basal slip which was resisted by the constraint. Near the end of the deformation, the double twinning mechanism became operative but contributed very little to the overall deformation. Meanwhile, no prismatic $\langle a \rangle$ slip was observed.

Besides studies on magnesium single crystal, polycrystals have also been investigated. Hauser et al. (1955) studied the deformation of polycrystalline magnesium with a texture in which the basal planes were favorably oriented parallel to the extrusion direction in tension at room temperature. Neither $\{10\bar{1}2\}$ twinning nor basal slip were favored in this polycrystal when strained in the extrusion direction. In all the tests, basal slip was observed exclusively within the grains, even in the grain which was unfavorably oriented for basal slip. $\{10\bar{1}2\}$ twinning occurred exclusively in the deformed specimens.

The deformation of variously oriented textured magnesium samples has been studied by uniaxial tension, compression and channel die compression (Kelley and Hosford, 1968a). The obtained stress-strain curves shown in **Figure 1.13** were analogous to those for single crystals (**Figure 1.12**) both in their general forms of anisotropy and stress levels. The anisotropic degree of the polycrystalline material was lower because of the orientations were distributed around an ideal basal texture.

In summary, basal slip is the easiest and most common slip mode in magnesium at room temperature. Prismatic slip and pyramidal slip contribute very little to overall deformation. As temperature increases, the prismatic slip and pyramidal slip systems become easier to be activated and contribute more to overall deformation. $\{10\bar{1}1\}$ twinning and some double twinning can produce limited deformation parallel to *c*-axis.

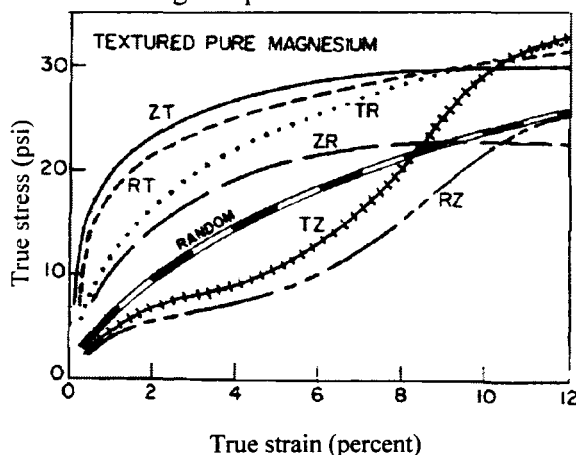


Figure 1.13 Stress-strain curves for textured magnesium under channel die compression.

The orientations are combinations of the letters R (rolling direction), T (transverse direction) and Z (thickness direction) with the first letter representing the loading direction and second letter the extension direction. (Kelley and Hosford, 1968a).

1.4.2 Deformation of magnesium alloys.

There are various magnesium alloys containing the alloying elements of aluminum, zinc, manganese, zirconium and rare earths, etc. **Table 1.3** summarizes CRSS values reported for magnesium and its alloys containing aluminum, zinc and manganese solutes. The upper section represents single crystal data for magnesium, magnesium-zinc and magnesium-manganese. Clearly, basal slip has the lowest CRSS, ranging from 0.45-0.81 MPa. Twinning has a CRSS 2-4 times larger, and prismatic slip has a CRSS much larger, 48-87 times. There is no single crystal data for AZ31B. Instead, CRSS values are obtained by fitting the macroscopic response with polycrystal plasticity models or by using in situ neutron diffraction to track lattice strain and peak intensity. Though the scatter is quite large, the general conclusion can be drawn that the additions raise the CRSS for all deformation mechanisms and reduce the ratios among them. For example,

the CRSS values of basal slip, twin and prismatic slip for magnesium alloys are 12-167, 7.5-17.5 and 1.4-2.8 times those of pure magnesium, respectively. The CRSS range for twinning (10-35MPa) is comparable to the range of basal slip (10-45MPa), while the ratio between them in pure magnesium is 2.5-4.4. Prismatic slip has even more scattered results, with CRSS varying from 1-5.5 times that of basal slip, as compared with 48-87 times in pure magnesium.

Table 1.3 CRSS values reported for magnesium and its aluminum-zinc-manganese alloys.

| Metal | Conditions | CRSS _{basal} (MPa) | CRSS _{twin} (MPa) | CRSS _{prism} (MPa) | CRSS _{twin} / CRSS _{basal} | CRSS _{prism} / CRSS _{basal} | CRSS _{basal} / CRSS _{basal-Mg} |
|-----------------------|--|---|--------------------------------|--------------------------------|---|--|---|
| Mg | SC | 0.81 ^a ;0.76 ^b ; 0.45 ^c ;0.65 ^d ; 0.52 ^e | 2 ^{f,g} | 39.2 ^f | 2.5-4.4 | 48-87 | |
| Mg 0.5 at. pct Zn | SC | | 2.7-2.8 ^h | | | | |
| Mg 5.1 at. Pct Zn | SC | | | | | | 5-10 ^p |
| Mg 1.24 at. Pct Mn | SC | | | | | | 10-40 ^q |
| AZ31B | PC,Taylor,EPSC, VPSC,XRD, ND,TEM, Schmid factor | 45',10' | 15',30', 25-35 ^m | 110',55' | 0.33',3',2 ^k | 2.4',5.5', 1-2.4 ^l ,1.1 ^l | 12-100 |
| AZ61 | PC,XRD | | | | | 1.5-2 ⁿ | |
| Mg 7.7 at. pct Al | PC,ND | 65-75 ^o | | | | | 80-167 |

SC, single crystal; PC, polycrystal; XRD, X-ray diffraction; ND, neutron diffraction; VPSC, visco-plastic self-consistent model; EPSC, elasto-plastic self-consistent model; Taylor, Taylor model.

- | | |
|-------------------------------------|-------------------------------------|
| a. (Schmid, 1931) | b. (Bakarian and Mathewson, 1943) |
| c. (Burke and Hibbard, 1952) | c. (Hsu and Cullity, 1954) |
| e. (Conrad and Robertson, 1957) | f. (Reed-Hill and Robertson, 1957a) |
| g. (Reed-Hill and Robertson, 1957b) | h. (Miura, 2004) |
| i. (Agnew, 2002) | j. (Agnew et al., 2003) |
| k. (Styczynski et al., 2004) | l. (Koike et al., 2003) |
| m. (Brown et al., 2005) | n. (Koike and Ohyama, 2005) |
| o. (Gharghouri, 1997) | p. (Byrne, 1963) |
| q. (Chun and Byrne, 1969) | |

As stated earlier, magnesium alloys show promise for applications in forming components with light weight. However, due to inadequate available slip systems at room temperature, the magnesium alloys show very limited formability (Emley, 1966). Their comparably low values of uniform elongation, tensile reduction of area, sheet forming limits, cold rollability and bendability constrain the wide use of magnesium alloys as a wrought metal (Avedesian and Baker, 1999). Those effects can be strengthened if the

material has a strong texture during the wrought processing. Both rolling process and extrusion process produce strong basal texture in which basal planes are oriented parallel to the rolling or extrusion directions. Grain size is another factor that influences the mechanical behavior of magnesium alloys.

The efforts to improve the room temperature formability of magnesium alloys can be mainly categorized to three methods: appropriate additions, grain refinement and texture control. The effect of various alloying additions on the room temperature tensile ductility of magnesium alloys has been studied in great detail (McDonald, 1940; Hauser et al., 1958; Agnew et al., 2006b). Room temperature tensile tests were performed on samples in which the tensile axis was aligned with the extrusion axis and the data are presented in **Figure 1.14**. Both Mg-Li and Mg-Y alloys have increased yield stresses, as compared to pure magnesium. The tensile elongations have increased while the overall work-hardening rates have simultaneously decreased.

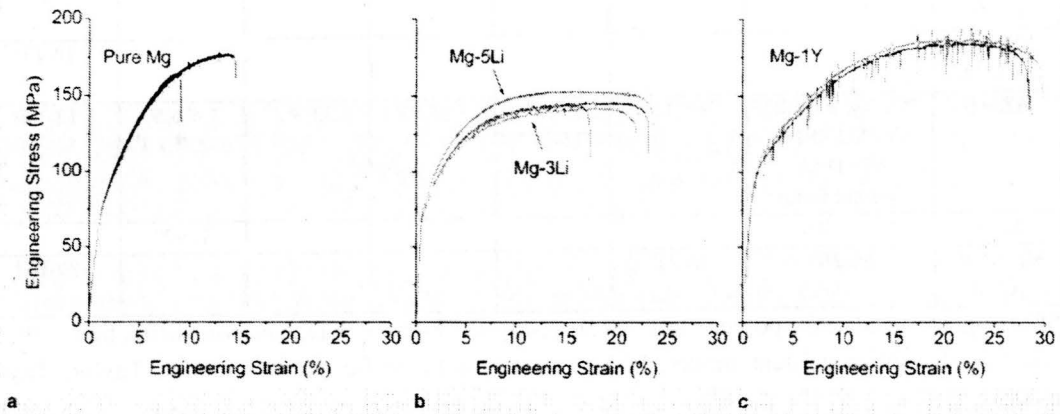


Figure 1.14 Tensile stress-strain curves for (a) pure magnesium, (b) Mg-Li, and (c) Mg-1Y alloys at room temperature (Agnew et al., 2006b).

Grain refinement has also been known to improve the ductility of magnesium and its alloys (Kubota et al., 1999). The elongations for magnesium alloy AZ91 and ZK60 have been improved by a factor of four by grain refinement (Kubota et al., 1999). Simultaneously, their strengths have also been enhanced. Both rare earth element additions (Emley, 1966) and severe plastic deformations can achieve grain refinement. Typical severe plastic deformation processes include equal channel angular extrusion (ECAE) (Agnew et al., 2004), high pressure torsion (Kai et al., 2008) and high reduction hot rolling (Perez-Prado et al., 2004).

Another method to improve the formability is through texture control. Mukai et al. (2001) and Agnew et al. (2004) have shown that enhanced ductility can be achieved through ECAE, where the basal planes are preferentially inclined $\sim 45^\circ$ to the extrusion direction. Chino et al. (2008) have observed enhanced tensile ductility of AZ31 bar through torsional extrusion (TE), where the basal poles are inclined $\sim 30^\circ$ to the extrusion

direction. Huang et al. (2008) have reported an increase in the uniform strain prior to necking in AZ31 sheet produced by differential speed rolling (DSR), where the basal poles are tilted $\sim 15^\circ$ in the rolling direction (RD). Another process like conform continuous extrusion (Zhang et al., 2008) and repeated unidirectional bending (Song et al., 2010) can also weaken the basal texture and improve the ductility of the magnesium alloy AZ31. These processes also involve significant grain refinement, which can enhance formability. However, through careful control of grain size, Mukai et al. (2001) demonstrated that ductility was drastically enhanced in AZ31 without refining its grain structure, implying that significant improvement can be made to the formability through texture optimization only. This can be confirmed by tension tests on extruded AZ61 for different tilt angles between extrusion and loading directions (Kleiner and Uggowitzer, 2004), where the tests were performed on the same material with various initial texture. The stress-strain curves (Figure 1.15) clearly show that when the extrusion direction is 45 degrees from the tensile axis maximizes the ductility, where the grains have been rotated to activate basal slip easiest.

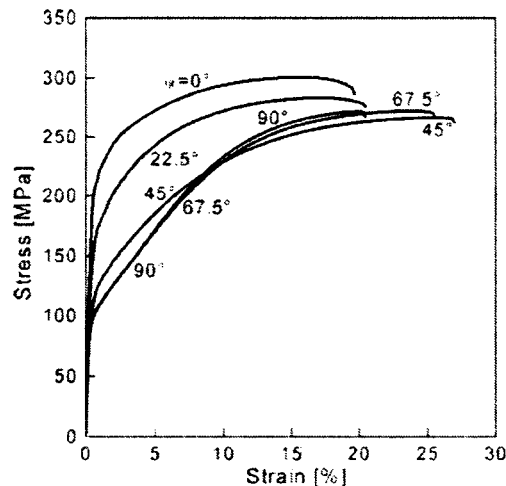


Figure 1.15 Tensile stress-strain curves of extruded AZ61 for different tilt angles between extrusion direction and loading direction (Kleiner and Uggowitzer, 2004).

Though a great deal of experimental works has been carried out, there are rare systematic analytical/numerical studies to investigate the influence of individual texture components on the formability of magnesium polycrystals. In a recent study, Wang et al. (2010c) investigated the influence of basal texture on the uniform strain under uniaxial tension and the limit strain under in-plane plane strain tension. This preliminary study suggested that formability can be significantly improved by controlling texture even without grain refinement. Chapter 5 carries out a detailed study on the effects of basal texture on FLDs.

As the test temperature increased, the formability of the magnesium alloys was extensively enhanced (Figure 1.16). The material did not fail when the strain reached

large values up to 100% at 200°C and 250°C. This is attributed to the decrease of the CRSS of non-basal slip systems. Therefore more slip systems are available to accommodate the deformation. In the compression test, strong sigmoidal hardening was observed at room temperature and moderate temperatures, while little hardening was observed at higher temperature. By comparing the stress-strain curves, the tension and compression asymmetry was reduced with increasing temperature. At 250°C, the material almost showed symmetric mechanical behavior under tension and compression. This was a result of the thermal suppression of twinning.

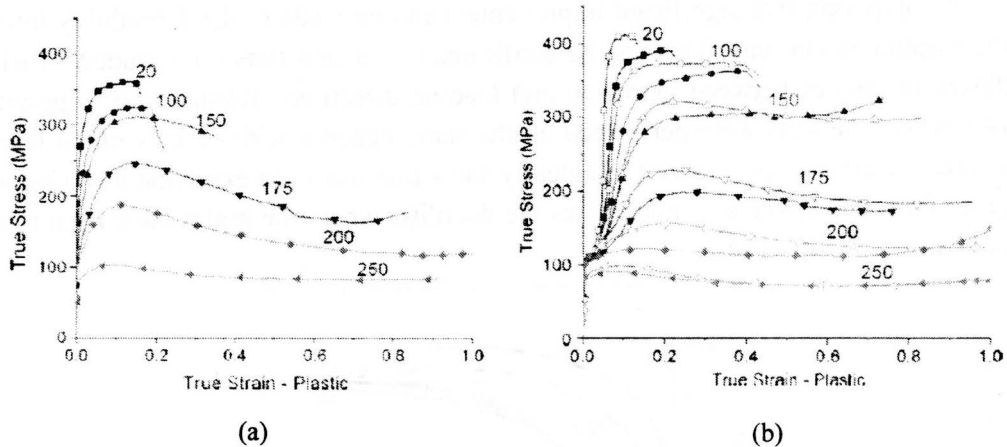


Figure 1.16 Stress-strain curves of (a) tension and (b) compression as a function of temperature (Jain and Agnew, 2007).

This section discusses the deformation of magnesium alloys. Magnesium alloys show higher CRSS for all deformation mechanisms than those of pure magnesium, while the ratios among them are compressed. Efforts have been made to increase the formability of magnesium alloys. Appropriate additions, grain refinement and texture controlling can enhance the formability of magnesium alloys at room temperature, while the properties at elevated temperature are already acceptable.

1.5 Constitutive modeling of polycrystalline materials

There are mainly two types of constitutive models for polycrystalline materials; continuum phenomenological models which involve proposing an appropriate yield surface, and polycrystal plasticity models which consider the polycrystal material as a composite composed of many grains.

1.5.1 Continuum phenomenological models

The conventional continuum phenomenological approach introduced the representative volume element (RVE) of material which is subjected to a near-uniform macroscopic stress. This continuum assumption neglects the local heterogeneity of the stress and strain within the RVE and works with averaged quantities, as the effect of the heterogeneity act

merely indirectly through a certain number of internal variables (Chaboche, 2008). At the continuum scale, a yield criterion, a flow rule and a hardening law are usually sufficient to describe the plastic deformation of metals. Conventional anisotropic continuum phenomenological models have mainly developed for materials with cubic structure (Hill, 1948; Barlat et al., 1991; Karafillis and Boyce, 1993; Barlat et al., 1997), which have a large number of identical slip systems and no deformation twinning. However, these models have been challenged by the general plastic behavior of HCP materials due to tension and compression yielding asymmetry. This phenomenon may be represented by the eccentricity of the yield surface (Kelley and Hosford, 1968a). The introduction of linear stress terms (Kelley and Hosford, 1968b) is appropriate for small eccentricity, but the compressive yield stress can be half of the tensile yield stress in magnesium alloys (Kelley and Hosford, 1968a). Isotropic yield criteria can be modified to permit orthotropic behavior including the third stress deviator invariant (Cazacu and Barlat, 2004), thus requiring 11 fit parameters, and linear transformations (Cazacu et al., 2006; Plunkett et al., 2008), requiring 6–16 fit parameters. A constant non-zero back stress has been used to deal with initial yield surface eccentricity (Yoon et al., 1998). Combined with an anisotropic yield function, this method has predicted earing of drawn cups sufficiently, but the complex hardening of magnesium alloys (Lou et al., 2007) is unlikely to be reproduced by a constant back stress. Different joint isotropic-kinematic constitutive models have been proposed in order to reproduce the Bauschinger effect and transient yield following abrupt strain path changes (Chaboche, 1986; 2008; Lee et al., 2008; Lee et al., 2009; Li et al., 2010).

In general, continuum phenomenological models are not computationally intensive and can be easily implemented in the FE codes. However, they are not able to describe the evolution of anisotropy due to grain level features, such as the texture evolution.

1.5.2 Polycrystal models

In polycrystal plasticity models, materials are considered as a composite composed of crystals or grains with a preferred orientation distribution, called crystallographic texture (Kocks et al., 1998). Each grain accommodates imposed deformation based on slip and twinning mechanisms in single crystal plasticity. To describe the deformation of a polycrystal, various homogenization schemes have been developed based on single crystal plasticity theories. The most popular ones consist of Taylor model (Taylor, 1938), Sachs model (Sachs, 1928) and Self Consistent (SC) models (Molinari et al., 1987; Lebensohn and Tomé, 1993; Turner and Tomé, 1994).

The Taylor model, well known as the upper bound model, assumes that the strains are equal in all the grains and ignores strains heterogeneity among grains. Therefore, Taylor model may cause high stress concentration and further activate unexpected

mechanisms with large CRSS in HCP metals. This effect is shown in the comparison between the predicted texture by Taylor model and experimental observations of rolled zircaloy-4 (Tomé et al., 1988). The Taylor model is mainly suitable to model the plastic response of cubic metals with small to moderate plastic heterogeneity. The Sachs model, on the other hand, well known as the lower bound model, assumes that the stresses are equal in all the grains and ignores stresses heterogeneity among grains. This model is suitable to model the materials with soft grains.

The SC approach considers all the grains with the same orientation as an inclusion embedded in a homogenous effective medium (HEM), which is an aggregate of all the inclusions. The external imposed stress and strain should coincide with the average of the aggregate. Interaction between an inclusion and the HEM depends on imposed stress, the overall behavior of HEM and the orientation of the inclusion. Among the SC models, the visco-plastic self-consistent (VPSC) model (Molinari et al., 1987; Lebensohn and Tomé, 1993) is the most popular and has been successfully applied to study the large strain behavior and texture evolution of HCP polycrystalline materials under various deformations (Lebensohn et al., 1996b; Agnew et al., 2001; Agnew and Duygulu, 2005; Proust et al., 2009). Elasto-plastic self-consistent (EPSC) model (Turner and Tomé, 1994) is another popular one, which has been applied to interpret the elastic lattice strain measured by neutron diffraction (Agnew et al., 2006a; Muransky et al., 2008). This model has been recently extended to approximately account for finite strain (Neil et al., 2010) and applied to study the elastic lattice strain for copper and stainless steel.

The elastic lattice strain measured by in situ neutron diffraction, which is generally accepted to be a very sensitive indicator, has been used to study the plastic deformation mechanisms of magnesium alloy AZ31 (Agnew et al., 2003; Brown et al., 2005; Agnew et al., 2006a). In a displacement controlled in situ neutron diffraction test, stress relaxation has been observed during 7-20 minutes hold times while diffraction data is collected. Viscoplastic models, such as VPSC, do not include elastic deformation and thus cannot be used to study the lattice strains. Most of the experimentally measured lattice strain data have been studied by using the elastic-plastic self-consistent (EPSC) model developed by Turner and Tomé (1994) and extended to approximately account for large strain by Neil et al. (2010). However, the rate-insensitive nature of the constitutive law in which EPSC models are based upon prevents us from addressing creep and stress relaxation in general, and the experimentally observed relaxation associated with finite hold times for data acquisition in particular. It is expected that such a macroscopic relaxation can only be accounted by a rate-sensitive elastic-plastic model. Ideally, plastic deformation mechanisms should be studied by analyzing elastic lattice strain data, in addition to macroscopic stress-strain curves and texture evolutions, in terms of a large strain elastic-viscoplastic model which includes interaction among grains. Therefore, a large strain elastic-viscoplastic self-consistent model for polycrystalline materials is

developed (Wang et al., 2010e). The details of this model will be discussed in Chapter 2. In Chapter 4, this model is used to study the lattice strain of magnesium alloy AZ31 and the effects of stress relaxation and creep on lattice strain.

When the relation between stress and strain rate is nonlinear, it is useful to assume a linear expression. The common linear forms are the Secant, Affine, Tangent and meff approximations. **Figure 1.17** gives the schematic representation of linearization of the strain-rate and stress response for different types of interaction assumptions. The secant approximation gives the compliance (slope of the Secant linear line) containing the origin and the point defined by the macroscopic strain rate and stress. The corresponding macroscopic back-extrapolated term is zero. On the other hand, Affine approximation gives the compliance of the tangential slope at the macroscopic strain rate and stress point. A nonzero macroscopic back-extrapolated term will be obtained (Masson et al., 2000; Lebensohn et al., 2004). In the case of Tangent approximation, the compliances are, formally, the same as in the Affine case. However, instead of using this compliance and to avoid the iterative adjustment of the macroscopic back-extrapolated term, Molinari et al. (1987) obtained the Tangent compliance through the Secant compliance in combination with the Tangent-Secant relation derived by Hutchinson (1976). Since the Secant and Tangent approaches have been proven to tend to a uniform strain and a uniform stress in the rate-insensitive limit, respectively, an effective- m approximation was proposed (Molinari and Tóth, 1994; Tomé, 1999). This approximation gives a polycrystal response in between the stiff Secant and the compliant Tangent, which remains intermediate with respect to the bounds in the rate-insensitive limit.

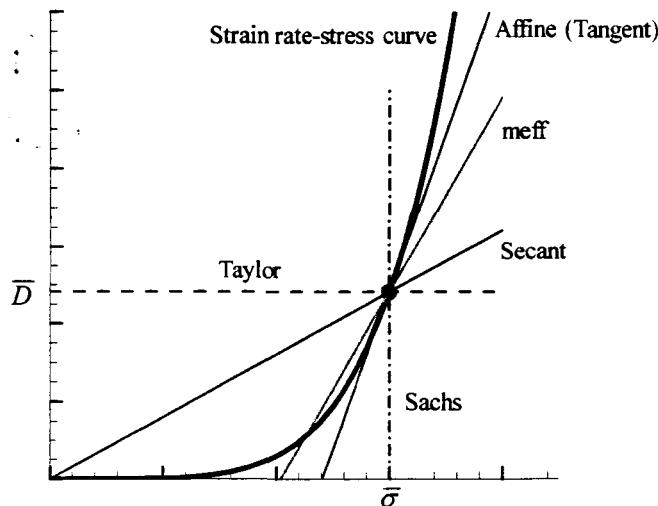


Figure 1.17 Schematic one dimensional representation of the linearization of strain rate against stress response in vicinity of the overall magnitudes ($\bar{\sigma}, \bar{D}$) for different types of interaction assumptions (Tomé, 1999).

However, it has been found that numerical results are extremely sensitive to the stiffness of the grain-matrix interaction associated with the various Self-Consistent Schemes (SCSs) for VPSC/EVPSC model (Wang et al., 2010e). Therefore, it is necessary to carry out an assessment of the predictive capability of the VPSC/EVPSC model with various SCSs including Secant, Affine, Tangent and the effective interaction m^{eff} . It is worth mentioning that various SCSs have been evaluated by comparing their predictions, in terms of mechanical responses and texture evolutions, with finite element calculations, full field simulations or available experimental evidence for polycrystals (Molinari and Toth, 1994; Tomé, 1999; Lebensohn et al., 2007). It has been found that Secant and Tangent SCSs, among the first-order SCSs, exhibit asymptotic trend to respectively the upper-bound and lower-bound in the rate-insensitive limit, and thus are not appropriate for highly anisotropic materials like HCP polycrystals. The intermediate SCSs, Affine and m^{eff} give better overall predictions, if appropriate artificial parameter m^{eff} is assigned according to results of finite element calculations (Molinari and Toth, 1994) or relative directional compliance approach (Tomé, 1999). It has to be noted that those evaluations were based on the assumption that all the material parameters at single crystal level are the same for various SCSs. A real challenge in modeling HCP polycrystals is that it is almost impossible to directly measure the single crystal properties. It has been generally accepted that the differences in stress experienced by differently orientated single crystals in an HCP polycrystal are mainly due to the orientation of a single crystal and the interaction of the single crystal with its surrounding grains. The interaction is, of course, dependent on the self-consistent scheme employed. Therefore, for a textured HCP polycrystal, the only practical way to determine the single crystal properties in a polycrystal plasticity model is by curve-fitting numerical simulations based on the polycrystal model to the corresponding macroscopic experimental data (Xu et al., 2008). The predicative capability of the polycrystal plasticity model is then assessed by comparing its predictions based on the fitted material constants to the corresponding experiment data other than those used in the fitting. To the best of the author's knowledge, an assessment for the VPSC and EVPSC models with various SCSs has not been systematically carried out for Mg alloys. However, it is clear that such an assessment is meaningful only if the number of experiments employed is large enough to cover various different deformation processes for a given material. In Chapter 3, we use for such matter the Mg alloy AZ31B in sheet form, thoroughly characterized experimentally by Jain and Agnew (2007).

It is important to mention that self-consistent polycrystal plasticity models consider the interaction between a given grain and a "homogeneous matrix" representing the rest of the materials, but they do not take into account the specific interaction between an individual grain and its neighbouring grains, or inhomogeneous deformation within the grain itself. When the phenomenon to be studied depends on the local characteristics

and heterogeneity of such interaction (stress-strain response, Lankford coefficient and texture evolution are not particularly sensitive to local effects), then crystal plasticity finite element models (CPFEM) may be required. In CPFEM simulation, an element of the finite element mesh represents either a single crystal or a part of a single crystal, and the constitutive response at an integration point is described by the single crystal constitutive model. This approach enforces both equilibrium and compatibility throughout the polycrystalline aggregate in the weak finite element sense (Anand and Kalidindi, 1994; Wu et al., 2004b). Furthermore, this approach facilitates taking into account grain morphology and modeling of inhomogeneous deformation at the crystal level (Wu et al., 2006; Wu et al., 2007a).

In this study, the method of polycrystal plasticity, more specifically, self-consistent method will be used. A large strain elastic-viscoplastic self-consistent (EVPSC) model is developed (Chapter 2). Then, this self-consistent polycrystal plasticity model is assessed for magnesium alloy AZ31B sheet (Chapter 3). A further assessment of EVPSC to investigate the lattice strain of magnesium alloy AZ31 is studied in Chapter 4. In Chapter 5, the EVPSC model is applied to study the formability of HCP materials. Chapter 6 gives the general conclusions of the thesis.

Chapter 2. A finite strain elastic-viscoplastic self-consistent model for polycrystalline materials

Abstract — A large strain elastic-viscoplastic self-consistent (EVPSC) model for polycrystalline materials is developed. At single crystal level, both the rate sensitive slip and twinning are included as the plastic deformation mechanisms, while elastic anisotropy is accounted for in the elastic moduli. The transition from single crystal plasticity to polycrystal plasticity is based on a completely self-consistent approach. It is shown that the differences in the predicted stress-strain curves and texture evolutions based on the EVPSC and the viscoplastic self-consistent (VPSC) model proposed by Lebensohn and Tomé (1993) are negligible at large strains for monotonic loadings. For the deformations involving unloading and strain path changes, the EVPSC predicts a smooth elasto-plastic transition, while the VPSC model gives a discontinuous response due to lack of elastic deformation. It is also demonstrated that the EVPSC model can capture some important experimental features which cannot be simulated by using the VPSC model.

2.1 Introduction

The plastic deformation in most Face Centered Crystals (FCC) and Body Centered Crystals (BCC) is dominated by crystallographic slip. In contrast, both slip and twinning contribute to the plastic deformation in Hexagonal Close Packed (HCP) crystals. Constitutive modeling of crystalline materials starts with developing a single crystal plasticity model to describe elastic and plastic deformation at grain level. However, the prediction of the mechanical behavior of polycrystalline materials from the responses of their single crystals has been a tremendous challenge for many years. The reason for this is that it is extremely difficult, if not impossible, to mathematically solve a boundary value problem with extremely high degrees of freedom due to interaction between grains. Therefore, the response of a polycrystal, consisting of many grains, is usually calculated by using some averaging/homogenizing methods.

Sachs (1928) and Taylor (1938) pioneered the development of polycrystal plasticity. The Sachs model, which is known as the lower bound model, assumes that each grain in the polycrystalline aggregate is under a uniform stress, equal to the macroscopic stress. The Taylor model, known as the upper bound model, assumes that all grains must accommodate the same plastic strain, equal to the macroscopically imposed strain. In these models, the actual heterogeneities that occur during deformation of polycrystals are neglected. More specifically, Sachs and Taylor-type models neglect either stress or strain variations from grain to grain, respectively, in the polycrystalline aggregate. The Sachs model has been extended to large viscoplastic and elastic-viscoplastic deformations (Ahzi et al., 1993). The Taylor model has been extended to

elastic-plastic deformations by Lin (1957), and to finite elastic-viscoplastic deformations by Asaro and Needleman (1985). More sophisticated hardening laws at slip system level and more efficient computational procedures have been implemented into the Taylor polycrystal plasticity model (Bassani and Wu, 1991; Kalidindi et al., 1992). The Taylor model has played an important role in the field of sheet metal forming (Wu et al., 1997; Dawson et al., 2003). Noticeable new advance in the Taylor polycrystal plasticity model has been the incorporation of deformation twinning (Kalidindi, 1998; Staroselsky and Anand, 1998; 2003; Wu et al., 2007b).

Another popular homogenizing method is the self-consistent approach, originally proposed by Kröner (1958). In general, self-consistent models assume that each grain is an ellipsoidal inclusion embedded in an infinite homogeneous equivalent medium (HEM). Based on the use of Eshelby's solution (Eshelby, 1957) for an ellipsoidal inclusion in a linear elastic matrix, Kröner (1961) and Budianski and Wu (1962) independently developed a small strain elastic-plastic self-consistent polycrystal model. This model neglects plastic interactions between the inclusions and the surrounding matrix because the matrix is assumed to be elastic. The plastic interactions were taken into account in an incremental self-consistent model for small elastic-plastic deformations proposed by Hill (1965). This model has been incorporated to simulate polycrystalline deformations (Hutchinson, 1970). An extension of Hill's incremental approach to study polycrystals at large elastic-plastic deformations was proposed by Iwakuma and Nemat-Nasser (1984). A small strain elastic plastic self-consistent model that accounts both slip and twinning as plastic deformation mechanisms was developed by Turner and Tomé (1994) for HCP polycrystals. Recently, Neil et al. (2010) have extended Turner and Tomé's formulation to approximate large strain deformation, accounting for texture evolution associated with slip and twinning reorientation.

The above mentioned self-consistent polycrystal plasticity models are time independent. An extension of Hill's incremental self-consistent scheme to viscoplastic deformation has been proposed by Hutchinson (1976) and used to simulate creep behavior of polycrystals. Molinari et al. (1987) developed a non-incremental self-consistent model by using the tangent modulus-based formulation and the integral equation method. This model has been used to simulate large plastic deformations in HCP polycrystals with a full anisotropic overall tangent modulus (Lebensohn and Tomé, 1993; 1994).

Elasticity has been included in various rate-dependent self-consistent models. Weng (1981; 1982; 1993) has clearly indicated that the Kröner-Budiansky-Wu self-consistent approach is exactly applicable to isotropically elastic creep materials. Following Weng's formulism, Nemat-Nasser and Obata (1986) developed an averaging technique to generalize Hill's self-consistent method for application to rate-dependent crystalline flow at finite deformations. However, Kouddane et al. (1991; 1993) and Zaoui

and Raphanel (1991) have indicated that the assumption of uniform relaxation stress in the matrix by Weng (1982) and by Nemat-Nasser and Obata (1986) leads to unrealistic strong matrix/inclusion interactions (Paquin et al., 2001), and to results which do not deviate much from those of an upper bound Taylor type formulation (Harren, 1991). To soften the inclusion/matrix interactions of the elastic-viscoplastic formulation, an approximate elastic-viscoplastic interaction law has been proposed by Li and Weng (1997; 1998a; 1998b) and by Molinari and coworkers (Kouddane et al., 1991; 1993; Molinari et al., 1997; Mercier et al., 2005; Mercier and Molinari, 2009), who applied it to linear and non-linear viscous solids using several simplifying assumptions, such as incompressible elasticity, two isotropic phases or isotropic grains, no texture evolution. An exact fully anisotropic elastic-linear-viscous (Maxwell) polycrystal model was developed by Turner and Tomé (1993) and applied to irradiation creep (linear) of zirconium alloys. In a subsequent paper, Turner, et al. (1994), consider the case of thermal creep of zirconium alloys (non-linear-viscosity), and show that the approximate interaction equations of Molinari et al. (1997) is applicable in the linear case when elastic and viscous moduli, plus stress and stress rate, obey the so called 'quasi-static' condition. Turner, et al. (1994) assume that the same conditions can be applied to the non-linear case, and adopt the same approximation of Molinari et al. (1997) for simulating thermal creep of aggregates. However, all the models discussed above are limited to small deformations. Most of these works were reviewed by Zaoui (2002).

Although self-consistent modeling has been the focus of attention for many years, recent efforts on development/improvement of self-consistent polycrystal plasticity models have been mainly animated by more accurately describing elastic-plastic deformations of HCP polycrystalline materials like magnesium and its alloys. In addition to the fact that both slip and twinning contribute to the plastic deformation, HCP material exhibits a very strong anisotropy due to its low symmetry of the crystallographic structure. It has been found that the critical resolved shear stresses are quite different between different slip systems (Yoo, 1981). As is well known, the Taylor assumption is reasonable for materials that exhibit a mildly anisotropic plastic response that is, comprised of crystals with many slip systems of comparable strength. However, using Taylor in other situations usually leads to prediction of excessively high stresses, incorrect texture evolutions, or both (Lebensohn et al., 2003). The modeling of HCP polycrystals is consistent with these trends. MacEwen et al. (1989; 1990) have shown that the upper bound approach does not work well for the prediction of residual grain-interaction stresses in zirconium alloys. On the other hand, it has been demonstrated that the evolution of internal strains and stresses in HCP polycrystalline AZ31 and Zircaloy-4 can be predicted with the aid of the elastic-plastic self-consistent model (Agnew et al., 2006a; Carr et al., 2007). In addition, while the full constraint Taylor approach does not consider the effect of grain morphology upon stress-strain accommodation, self-

consistent model accounts for grain morphology through the inclusion formalism. In general, it has become clear that a self-consistent approach is more suitable than the full constraint Taylor approach for constitutive modeling of HCP polycrystals. The viscoplastic self-consistent (VPSC) model, proposed by Lebensohn and Tomé (1993), has been successfully applied to simulate large strain behavior and texture evolution of HCP polycrystalline materials under various deformations (Agnew et al., 2001; Agnew and Duygulu, 2005; Jain and Agnew, 2007). Furthermore, the VPSC model has been constantly improving by incorporating more advanced slip and twinning models (Proust et al., 2009).

The current polycrystal plasticity models with both slip and twinning, including the VPSC and the model developed by Kalidindi (Wu et al., 2007b), involve a large number of fitting parameters, which may not be unequivocally determined. Therefore, to some extent, the predictive capability of such a polycrystal plasticity model relies on introducing more constraints such that the number of suitable parameter combinations could be significantly reduced. An efficient way to do so is that material parameters are obtained by not only fitting the macroscopic stress-strain curves and deformed textures but also *simultaneously* fitting elastic lattice strains measured from in situ neutron diffraction. It is generally accepted that a development of the elastic lattice strains during loading in different grain orientations can be used as a very sensitive indicator of plastic deformation mechanisms at microscopic levels. In a displacement-controlled in situ neutron diffraction test, a stress relaxation has been observed during 7–20 min hold times while diffraction data are collected (Agnew et al., 2006a; Muransky et al., 2008). The VPSC model does not include elastic deformation and thus cannot be used to study lattice strains. Most of the experimentally measured lattice strain data have been interpreted by using the elastic-plastic self-consistent (EPSC) model developed by Turner and Tomé (1994). However, the EPSC model works only for small deformation and does not include texture evolution especially the sudden reorientation due to twinning. On the other hand, the macroscopic true strain involved in an in situ neutron diffraction test could reach 12% (Agnew et al., 2006a). Very recently, Clausen et al., (2008) extended the EPSC model by including texture development and stress relaxation due to twinning. However, the rate-insensitive character of the constitutive law upon which EPSC is based, prevents us from addressing creep and stress relaxation in general, and the experimentally observed relaxation associated with finite hold times for data acquisition in particular. It is expected that such a macroscopic relaxation can only be accounted by a rate-sensitive elastic-plastic model. Ideally, plastic deformation mechanisms should be studied by analyzing elastic lattice strain data, in addition to macroscopic stress-strain curves and texture evolutions, in terms of a large strain elastic-viscoplastic model including interaction among grains. However, such a constitutive model has not yet been developed.

The purpose of the present Chapter is to develop a finite strain elastic-viscoplastic self-consistent (EVPSC) constitutive model for polycrystalline materials. At single crystal level, both the rate sensitive slip and twinning are included as the plastic deformation mechanisms, while elastic anisotropy is accounted in the elastic moduli. The transition from the single crystal plasticity to polycrystal plasticity is based on a completely self-consistent approach. The proposed EVPSC model is a completely general elastic-viscoplastic, fully anisotropic, self-consistent polycrystal model, applicable at large strain and to any crystal symmetry.

This Chapter is organized as follows. Section 2.2 formulates rather general constitutive equations for single crystals. Section 2.3 develops a large strain EVPSC model with the specific constitutive functions being presented in Section 2.4. Numerical examples and discussions, mainly to validate the EVPSC model and to reveal important differences between the EVPSC and VPSC models, are shown in Section 2.5. Conclusions are summarized in Section 2.6.

2.2 Constitutive relations for single crystals

Following Hill (1966), Hill and Rice (1972), Asaro and Rice (1977), and Asaro and Needleman (1985), the deformation in a crystal/grain is characterized by the deformation gradient tensor F and the velocity gradient tensor l :

$$F = \frac{\partial x}{\partial X} \quad (2.2.1)$$

$$l = \frac{\partial v}{\partial X} \quad (2.2.2)$$

where X is the initial coordinate of a point in the reference configuration; x is the current coordinate of the point in the deformed configuration; v is the velocity of the point x in the deformed crystal. It can be shown that:

$$\dot{F} = l \cdot F \quad (2.2.3)$$

The total deformation gradient F is decomposed into a plastic deformation gradient and an elastic deformation gradient:

$$F = F^e \cdot F^p \quad (2.2.4)$$

The velocity gradient can be decomposed into elastic and plastic parts:

$$l = l^e + l^p \quad (2.2.5)$$

where, $l^e = \dot{F}^e \cdot (F^e)^{-1}$, $l^p = F^e \cdot \dot{F}^p \cdot (F^p)^{-1} \cdot (F^e)^{-1}$, which can be further decomposed into symmetrical and asymmetrical parts:

$$l^e = d^e + w^e \quad (2.2.6)$$

$$l^p = d^p + w^p \quad (2.2.7)$$

where $d = d^e + d^p$ and $w = w^e + w^p$ are the symmetrical and asymmetrical parts of the velocity gradient tensor l , respectively.

The plastic deformation in a crystal is assumed to be due to slip and/or twinning. Assuming that $\dot{\gamma}^\alpha$ is the shear rate in slip/twinning system α , the plastic velocity gradient is given by

$$l^p = \sum_{\alpha} \dot{\gamma}^\alpha s^\alpha n^\alpha \quad (2.2.8)$$

where s^α and n^α denote the slip/twinning direction and normal direction of the slip/twinning system α in the current configuration, and are defined by $s^\alpha = F^e \cdot s_0^\alpha$ and $n^\alpha = n_0^\alpha \cdot (F^e)^{-1}$, where the unit vector s_0^α and n_0^α are the slip (twinning) and normal directions in the reference configuration, respectively. The plastic strain rate d^p and the plastic spin w^p are respectively the symmetrical and asymmetrical parts of l^p

$$d^p = \sum_{\alpha} \dot{\gamma}^\alpha P^\alpha, \quad P^\alpha = \frac{1}{2}(s^\alpha n^\alpha + n^\alpha s^\alpha) \quad (2.2.9)$$

$$w^p = \sum_{\alpha} \dot{\gamma}^\alpha R^\alpha, \quad R^\alpha = \frac{1}{2}(s^\alpha n^\alpha - n^\alpha s^\alpha) \quad (2.2.10)$$

The elastic constitutive equation for a crystal is specified by

$$\overset{\nabla}{\sigma}^* + \sigma \text{tr}(d^e) = L d^e \quad (2.2.11)$$

where L represents the elastic moduli, and $\overset{\nabla}{\sigma}^*$ is the Jaumann rate of the Cauchy stress tensor based on the lattice spin w^e :

$$\overset{\nabla}{\sigma}^* = \dot{\sigma} - w^e \cdot \sigma + \sigma \cdot w^e \quad (2.2.12)$$

The Jaumann rate of Cauchy stress based on the continuum spin w , $\overset{\nabla}{\sigma} = \dot{\sigma} - w \cdot \sigma + \sigma \cdot w$, can be expressed in terms of $\overset{\nabla}{\sigma}^*$ as

$$\overset{\nabla}{\sigma} = \overset{\nabla}{\sigma}^* - w^p \cdot \sigma + \sigma \cdot w^p \quad (2.2.13)$$

From (2.2.11-13), we have the Cauchy stress rate $\dot{\sigma}$:

$$\dot{\sigma}_{ij} = L'_{ijkl} l_{kl} - \dot{\sigma}_{ij}^0 \quad (2.2.14)$$

where $L'_{ijkl} = L_{ijkl} - \sigma_{ij} \delta_{kl} + \frac{1}{2} \delta_{ik} \sigma_{jl} - \frac{1}{2} \delta_{il} \sigma_{jk} - \frac{1}{2} \delta_{jl} \sigma_{ik} + \frac{1}{2} \delta_{jk} \sigma_{il}$

and

$$\dot{\sigma}_{ij}^0 = L_{ijkl} d_{kl}^p + w_{ik}^p \sigma_{kj} - \sigma_{ik} w_{kj}^p$$

Furthermore, (2.2.14) can be re-written as:

$$l_{ij} = A_{ijkl} \dot{\sigma}_{kl} + l_{ij}^b \quad (2.2.15)$$

where $A_{ijkl} = (L'_{ijkl})^{-1}$, $l_{ij}^b = A_{ijkl} \dot{\sigma}_{kl}^0$.

In order to complete the description of the plastic velocity tensor shown in (2.2.8), constitutive functions need to specify the shearing rate $\dot{\gamma}^\alpha$ on slip/twinning system α . $\dot{\gamma}^\alpha$ depends on, among other possible variables, the resolved shear stress τ^α and resistance τ_c^α of slip/twinning system α , as well as the strain rate sensitivity m . In general, $\dot{\gamma}^\alpha$ can be expressed as

$$\dot{\gamma}^\alpha = \dot{\gamma}^\alpha(\tau^\alpha, \tau_c^\alpha, m, \dots) \quad (2.2.16)$$

Here, the resolved shear stress τ^α is defined as

$$\tau^\alpha = \sigma \mathbf{P}^\alpha \quad (2.2.17)$$

The evolution of τ_c^α reflects the hardening (or softening) of the slip/twinning system and can be expressed in the following general form,

$$\dot{\tau}_c^\alpha = \dot{\tau}_c^\alpha(\tau_c^\alpha, \gamma^\beta, \dot{\gamma}^\beta, f^\beta, \dots) \quad (2.2.18)$$

Here, we use both superscripts α and β to indicate that the hardening of slip/twinning system α may be influenced by the slip/twinning activity on slip/twinning system β . In (2.2.18), f^β is the volume fraction of the twinned region of the crystal and is defined by its evolution equation:

$$\dot{f}^\beta = \frac{\dot{\gamma}^\beta}{\gamma^{tw}} \quad (2.2.19)$$

with γ^{tw} being the characteristic shear (constant) associated with twinning.

Since the shear rate $\dot{\gamma}^\alpha$ relates to the Cauchy stress through the resolved shear stress τ^α , the relation between l_{ij}^b and σ_{ij} in (2.2.15) can be expressed in a pseudo-linear form

$$l_{ij}^b = A_{ijkl}^v \sigma_{kl} + l_{ij}^0 \quad (2.2.20)$$

where A_{ijkl}^v and l_{ij}^0 are respectively the viscoplastic compliance and the back-extrapolated term, and can be chosen differently based on different linearization assumptions. The possible choices for the local linearized behavior will be discussed later in Section 2.4.

From (2.2.15) and (2.2.20), we obtain the strain rate \mathbf{d} and the spin \mathbf{w} tensors:

$$\mathbf{d}_{ij} = M_{ijkl}^e \dot{\sigma}_{kl} + M_{ijkl}^v \sigma_{kl} + \mathbf{d}_{ij}^0 \quad (2.2.21)$$

$$\mathbf{w}_{ij} = N_{ijkl}^e \dot{\sigma}_{kl} + N_{ijkl}^v \sigma_{kl} + \mathbf{w}_{ij}^0 \quad (2.2.22)$$

where $M_{ijkl}^e = \frac{1}{2}(A_{ijkl} + A_{jikl})$, $M_{ijkl}^v = \frac{1}{2}(A_{ijkl}^v + A_{jikl}^v)$, $\mathbf{d}_{ij}^0 = \frac{1}{2}(l_{ij}^0 + l_{ji}^0)$, $N_{ijkl}^e = \frac{1}{2}(A_{ijkl} - A_{jikl})$, $N_{ijkl}^v = \frac{1}{2}(A_{ijkl}^v - A_{jikl}^v)$, and $\mathbf{w}_{ij}^0 = \frac{1}{2}(l_{ij}^0 - l_{ji}^0)$.

These are rather general constitutive equations for single crystals. Suitable expressions for $\dot{\gamma}^\alpha$ and $\dot{\tau}_c^\alpha$ is required to complete the relations. More discussions about this will be presented in Section 2.4.

2.3 A large strain EVPSC model

In this section, we develop a completely self-consistent averaging scheme for an aggregate of single crystals whose mechanical behaviour are described by (2.2.21) and (2.2.22).

In the following formulation, whenever possible, the local and global quantities are respectively denoted by lower cases and capitals of the same letters. Alternatively, the local quantities are identified by superscript Ω , while the volume average is denoted by $\langle \dots \rangle$.

The local (single crystal) constitutive relations are now expressed as

$$d_{ij} = M_{ijkl}^{e\Omega} \dot{\sigma}_{kl} + M_{ijkl}^{v\Omega} \sigma_{kl} + d_{ij}^0 \quad (2.3.1)$$

$$w_{ij} = N_{ijkl}^{e\Omega} \dot{\sigma}_{kl} + N_{ijkl}^{v\Omega} \sigma_{kl} + w_{ij}^0 \quad (2.3.2)$$

Our objective is to obtain the corresponding constitutive relations for the overall strain rate tensor D , spin tensor W , and Cauchy stress rate tensor $\dot{\Sigma}$, which are respectively defined by

$$D = \langle d \rangle = \frac{1}{V} \int d dV \quad (2.3.3)$$

$$W = \langle w \rangle = \frac{1}{V} \int w dV \quad (2.3.4)$$

$$\dot{\Sigma} = \langle \dot{\sigma} \rangle = \frac{1}{V} \int \dot{\sigma} dV \quad (2.3.5)$$

where V denotes the volume of the aggregate.

Performing a homogenization on this linearized heterogeneous medium consists assuming a linear relation analogous to (2.3.1) at the effective medium (polycrystal) level:

$$D = M^e \dot{\Sigma} + M^v \Sigma + D^0 \quad (2.3.6)$$

where M^e , M^v and D^0 are the macroscopic elastic compliance, viscoplastic compliance and back extrapolated term, respectively. They are unknown a priori and need to be adjusted self-consistently.

Following Molinari et al. (1997) and Mercier and Molinari (2009), using $d = d^e + d^p$, (2.3.1) can be decomposed into the elastic and viscoplastic parts. The elastic part is linked to the Cauchy stress rate tensor $\dot{\sigma}$

$$d_{ij}^e = M_{ijkl}^{e\Omega} \dot{\sigma}_{kl} \quad (2.3.1a)$$

and the viscoplastic part is written as

$$d_{ij}^p = M_{ijkl}^{v\Omega} \sigma_{kl} + d_{ij}^0 \quad (2.3.1b)$$

In the following two sub-sections, we are going to seek the relations between microscopic quantities and the corresponding macroscopic quantities for the plastic part (Section 2.3.1) and elastic part (Section 2.3.2) separately. In Section 2.3.3, the results found in Sections 2.3.1 and 2.3.2 are merged to develop the relations between microscopic quantities and the corresponding macroscopic quantities for the elastic-viscoplastic response.

2.3.1 A rigid viscoplastic inclusion embedded in a homogeneous viscoplastic matrix

We first consider an ellipsoidal rigid viscoplastic single crystal Ω embedded in an infinitely extended homogeneous matrix V (Molinari et al., 1987; Lebensohn and Tomé, 1993). The constitutive relation for single crystal Ω is expressed by

$$d^p = M^{v\Omega} \sigma + d^0 \quad (2.3.7)$$

while the constitutive relation for the homogeneous matrix V is assumed as:

$$D^p = M^v \Sigma + D^0 \quad (2.3.8)$$

Invoking the concept of the equivalent inclusion (Mura, 1987), the local constitutive behavior can be re-written in terms of the homogeneous macroscopic moduli M^v and the fictitious eigen-strain-rate d^* :

$$d^p = M^v \sigma + D^p + d^* \quad (2.3.9)$$

Rearranging and subtracting (2.3.8) from (2.3.9) gives

$$\tilde{\sigma} = C^v (\tilde{d}^p - d^*) \quad (2.3.10)$$

Here, the symbol "~" denotes local deviations of the corresponding tensor from their macroscopic values and $C^v = (M^v)^{-1}$.

The equilibrium and far condition can be expressed as

$$\sigma \cdot \nabla = 0 \quad (2.3.11)$$

$$\tilde{\sigma} = 0 \text{ as } |x| \rightarrow \infty \quad (2.3.12)$$

Furthermore, the Green's functions are defined by

$$C_{imkl}^v G_{kj,lm}(x - x') = -\delta_{ij} \delta(x - x') \quad (2.3.13)$$

The above equation assumes that Green's functions exist in the usual sense, which is the case as long as the operator in (2.3.13) is elliptic. When this operator ceases to be elliptic, Green's functions cannot be obtained and we may have overall instability.

From (2.3.6) and (2.3.10), and with the aid of the Green's functions, we obtain

$$\tilde{d}_{ij}^p = J_{ijmn}^{v\Omega} C_{mnkl}^v d_{kl}^* = T_{ijkl}^{v\Omega} d_{kl}^* \quad (2.3.14)$$

where

$$J_{ijmn}^{v\Omega} = \int_{\Omega} G_{in,mj}(x - x') dx'$$

and

$$T_{ijkl}^{v\Omega} = J_{ijmn}^{v\Omega} C_{nmkl}^v$$

Combining (2.3.10) and (2.3.14) and eliminating the fictitious eigen-strain-rate d^* , the following interaction equation is obtained:

$$\tilde{d}_{ij}^p = d_{ij}^p - D_{ij}^p = -\hat{M}_{ijkl}^{v\Omega} \tilde{\sigma}_{kl} \quad (2.3.16)$$

with

$$\hat{M}_{ijkl}^{v\Omega} = (I_{ijmn} - T_{ijmn}^{v\Omega})^{-1} T_{mnpq}^{v\Omega} M_{pqkl}^v \quad (2.3.17)$$

Using the local and overall constitutive relations (2.3.7) and (2.3.8) and the interaction equation (2.3.16), the following localization equation is obtained:

$$\sigma_{ij} = B_{ijkl}^{v\Omega} \Sigma_{kl} + b_{ij} \quad (2.3.18)$$

where the localization tensors are defined as:

$$B_{ijkl}^{v\Omega} = (M_{ijmn}^{v\Omega} + \hat{M}_{ijmn}^{v\Omega})^{-1} (M_{mnpq}^v + \hat{M}_{mnpq}^{v\Omega}) \quad (2.3.19)$$

$$b_{ij} = (M_{ijmn}^{v\Omega} + \hat{M}_{ijmn}^{v\Omega})^{-1} (D_{mn}^0 - d_{mn}^0) \quad (2.3.20)$$

2.3.2 An elastic inclusion embedded in a homogeneous elastic matrix

We now consider an ellipsoidal elastic single crystal Ω embedded in an infinitely extended homogeneous matrix V , based on an approach used by (Nemat-Nasser and Obata, 1986). The constitutive relation for single crystal Ω is expressed by

$$d^e = M^{e\Omega} \dot{\sigma} \quad (2.3.21)$$

and the corresponding constitutive relation for the homogeneous matrix V is assumed as:

$$D^e = M^e \dot{\Sigma} \quad (2.3.22)$$

Using the equilibrium condition

$$\dot{\sigma} \cdot \nabla = 0 \quad (2.3.23)$$

and the far condition

$$\tilde{\sigma} = \dot{\sigma} - \dot{\Sigma} = 0 \text{ as } |x| \rightarrow \infty \quad (2.3.24)$$

in their rate forms, as well as the Green's functions similar to those shown in (2.3.13), the following interaction equation is obtained

$$\tilde{d}_{ij}^e = d_{ij}^e - D_{ij}^e = -\hat{M}_{ijkl}^{e\Omega} \tilde{\sigma}_{kl} \quad (2.3.25)$$

where $\hat{M}_{ijkl}^{e\Omega}$ is calculated from solving the Green's functions by using M^{e-1} . From (2.3.21), (2.3.22) and (2.3.25), we obtain the following localization equation:

$$\dot{\sigma}_{ij} = B_{ijkl}^{e\Omega} \dot{\Sigma}_{kl} \quad (2.3.26)$$

with the localization tensor being defined as:

$$B_{ijkl}^{e\Omega} = (M_{ijmn}^{e\Omega} + \hat{M}_{ijmn}^{e\Omega})^{-1} (M_{mnpq}^e + \hat{M}_{mnpq}^{e\Omega}) \quad (2.3.27)$$

2.3.3 An elastic-viscoplastic inclusion embedded in a homogeneous elastic-viscoplastic matrix

The derivations presented above solve the problems of a viscoplastic inclusion embedded in a viscoplastic effective medium (Section 2.3.1), and an elastic inclusion embedded in an elastic effective medium (Section 2.3.2), subjected to external loading conditions. For an elastic-viscoplastic inclusion embedded in an elastic-viscoplastic effective medium under remote loading conditions, the relations between microscopic quantities and the corresponding macroscopic quantities can be developed from the associated results derived in Sections 2.3.1 and 2.3.2. Following the interaction equation proposed by (Molinari et al., 1997), from (2.3.16) and (2.3.25) we have

$$d_{ij} - D_{ij} = -\hat{M}_{ijkl}^{e\Omega}(\dot{\sigma}_{kl} - \dot{\Sigma}_{kl}) - \hat{M}_{ijkl}^{v\Omega}(\sigma_{kl} - \Sigma_{kl}) \quad (2.3.28)$$

The above interaction equation is the same as in Turner et al. (1994), in which they show that (2.3.28) is a valid approximation for the exact Maxwell solid (linear viscosity), provided that a relation between viscous modulus, elastic modulus, stress, and stress rate, is fulfilled ('quasi-elastic' approach). In this Chapter, as in Turner et al. (1994), we assume that (2.3.28) remains valid for non-linear viscosity if the same relation is fulfilled.

Enforcing the condition (2.3.4) and using (2.3.18), (2.3.26) and the macroscopic constitutive equation (2.3.6), we obtain

$$\begin{aligned} M_{ijmn}^e \dot{\Sigma}_{mn} + M_{ijmn}^v \Sigma_{mn} + D_{ij}^0 \\ = \langle M_{ijkl}^{e\Omega} B_{klmn}^{e\Omega} \rangle \dot{\Sigma}_{mn} + \langle M_{ijkl}^{v\Omega} B_{klmn}^{v\Omega} \rangle \Sigma_{mn} + \langle M_{ijkl}^{v\Omega} b_{kl} \rangle + d_{ij}^0 \end{aligned} \quad (2.3.29)$$

Respectively equating the linear and independent terms in (2.3.30) leads to the following self-consistent equations for the homogeneous compliances and back-extrapolated term:

$$M_{ijkl}^e = \langle M_{ijmn}^{e\Omega} B_{mnlk}^{e\Omega} \rangle \quad (2.3.30a)$$

$$M_{ijkl}^v = \langle M_{ijmn}^{v\Omega} B_{mnlk}^{v\Omega} \rangle \quad (2.3.30b)$$

$$D_{ij}^0 = \langle M_{ijkl}^{v\Omega} b_{kl} \rangle + d_{ij}^0 \quad (2.3.30c)$$

If the grains/ellipsoids have the same shape and orientation, it can be shown that the same equations are obtained from the condition that the average of the local stresses coincides with the macroscopic stresses. If the grains have each a different shape, they have associated different interaction tensors, and $\hat{M}_{ijkl}^{e\Omega}$ and $\hat{M}_{ijkl}^{v\Omega}$ cannot be factored from the averages. In this case, the following general self-consistent expressions should be used (Walpole, 1969; Lebensohn et al., 1996a; Lebensohn et al., 2004):

$$M_{ijkl}^e = \langle M_{ijmn}^{e\Omega} B_{mnpq}^{e\Omega} \rangle \langle B_{pqkl}^{e\Omega} \rangle^{-1} \quad (2.3.31a)$$

$$M_{ijkl}^v = \langle M_{ijmn}^{v\Omega} B_{mnpq}^{v\Omega} \rangle \langle B_{pqkl}^{v\Omega} \rangle^{-1} \quad (2.3.31b)$$

$$D_{ij}^0 = \langle M_{ijkl}^{v\Omega} b_{kl} + d_{ij}^0 \rangle - M_{ijkl}^v \langle b_{kl} \rangle \quad (2.3.31c)$$

The self-consistent equations (2.3.30) are a special case of (2.3.31). From a numerical point of view, (2.3.31) are more robust and improve the speed and stability of the convergence procedure, even when solving a problem where all the inclusions have the same shape ((Walpole, 1969; Lebensohn et al., 1996a; Lebensohn et al., 2004).

When the local stress rate and strain rate are obtained, the local spin and overall spin are obtained through (2.3.2) and (2.3.5).

If a stationary state is attained, where the rates of stresses are negligible (for example in a creep problem), the viscous response dominates, i.e. $d - D = d^p - D^p$, and the present model is thus reduced to a viscoplastic self-consistent model.

2.4 Specific constitutive functions

The elastic stiffness tensor L is a fourth order tensor. Due to its symmetric properties $L_{ijkl} = L_{jikl} = L_{ijlk}$, the elasticity tensor can be presented in terms of the following 6×6 matrix

$$L = \begin{bmatrix} L_{1111} & L_{1122} & L_{1133} & L_{1112} & L_{1113} & L_{1123} \\ & L_{2222} & L_{2233} & L_{2212} & L_{2213} & L_{2223} \\ & & L_{3333} & L_{3312} & L_{3313} & L_{3323} \\ & & & L_{1212} & L_{1213} & L_{1223} \\ & & & & L_{1313} & L_{1323} \\ \text{sym} & & & & & L_{2323} \end{bmatrix} \quad (2.4.1)$$

For an isotropic material one would have

$$\begin{aligned} L_{1111} &= L_{2222} = L_{3333} = \lambda + 2\mu \\ L_{1122} &= L_{1133} = L_{2233} = \lambda \\ L_{1212} &= L_{1313} = L_{2323} = \mu \end{aligned} \quad (2.4.2)$$

with the other components being zero, and where $\lambda = E\nu/(1+\nu)(1-2\nu)$ and $\mu = E/2(1+\nu)$ are the Lamè constants in terms of the Young's modulus E and the Poisson's ratio ν . The elastic anisotropy of single crystals can be included by using the crystal elastic constants C_{ij} (Wang and Mora, 2008). For HCP materials,

$$\begin{aligned} L_{1111} &= L_{2222} = C_{11}, \quad L_{3333} = C_{33} \\ L_{1122} &= C_{12}, \quad L_{1133} = C_{13} \\ L_{1212} &= C_{66}, \quad L_{1313} = L_{2323} = C_{44} \end{aligned} \quad (2.4.3)$$

The proposed EVPSC model is a general rate-sensitive self-consistent polycrystal plasticity model valid at arbitrary large deformations. Although EVPSC is very flexible to implement more sophisticated descriptions for slip and twinning, in the present

Chapter, without losing generality, the specific constitutive functions for describing slip/twinning are taken to be the same as in the VPSC model (Lebensohn and Tomé, 1993). This will make it easy for us to validate the EVPSC model because the difference in predictions between EVPSC and VPSC at large strains is expected to be small. The shearing rate on the slip/twinning system (2.2.16) is thus assumed to obey a power law form (Tomé et al., 1991). For slip systems,

$$\dot{\gamma}^\alpha = \dot{\gamma}_0 \left| \tau^\alpha / \tau_c^\alpha \right|^{(1/m)} \text{sgn}(\tau^\alpha) \quad (2.4.4)$$

while for twinning systems

$$\begin{aligned} \dot{\gamma}^\alpha &= \dot{\gamma}_0 (\tau^\alpha / \tau_c^\alpha)^{(1/m)} & \text{for } \tau^\alpha > 0 \\ \dot{\gamma}^\alpha &= 0 & \text{for } \tau^\alpha \leq 0 \end{aligned} \quad (2.4.5)$$

where $\dot{\gamma}_0$ is a reference value of slip/twinning rate, m is the rate sensitivity, sgn is the sign function. The evolution of τ_c^α is taken in the form

$$\dot{\tau}_c^\alpha = \frac{d\hat{\tau}^\alpha}{d\Gamma} \sum_\beta h^{\alpha\beta} \dot{\gamma}^\beta \quad (2.4.6)$$

where γ_{ac} is the accumulated shear strain in the grain, $h^{\alpha\beta}$ are the latent hardening coupling coefficients which empirically account for the obstacles on system α associated with system β activity. In (2.4.6), $\hat{\tau}^\alpha$ is the threshold stress:

$$\hat{\tau}^\alpha = \tau_0^\alpha + (\tau_1^\alpha + h_1^\alpha \gamma_{ac})(1 - \exp(-h_0^\alpha \gamma_{ac} / \tau_1^\alpha)) \quad (2.4.7)$$

The pseudo-linear forms for plastic strain rate and spin are written as

$$d_{ij}^p = M_{ijkl}^p \sigma_{kl} \quad (2.4.8)$$

$$w_{ij}^p = N_{ijkl}^p \sigma_{kl} \quad (2.4.9)$$

where $M_{ijkl}^p = \dot{\gamma}_0 \sum_\alpha (1/\tau_c^\alpha) \left| \tau^\alpha / \tau_c^\alpha \right|^{(1/m-1)} P_{ij}^\alpha P_{kl}^\alpha$, $N_{ijkl}^p = \dot{\gamma}_0 \sum_\alpha (1/\tau_c^\alpha) \left| \tau^\alpha / \tau_c^\alpha \right|^{(1/m-1)} R_{ij}^\alpha R_{kl}^\alpha$.

The Predominant Twin Reorientation (PTR) scheme proposed by Tomé et al. (1991) is used in the present Chapter to model the twinning activities. Within each grain Ω , the PTR scheme tracks the shear strain $\gamma^{\alpha,\Omega}$ contributed by each twin system α , and the associated volume fraction $V^{\alpha,\Omega} = \gamma^{\alpha,\Omega} / \gamma^{tw}$ as well. The sum over all twin systems associated with a given twin mode, and then over all the grains, represents the 'accumulated twin fraction' $V^{acc,mode}$ in the aggregate for the particular twin mode:

$$V^{acc,mode} = \sum_\Omega \sum_\alpha V^{\alpha,\Omega} \quad (2.4.10)$$

Since it is not numerically feasible to consider each twinned fraction as a new orientation, the PTR scheme adopts a statistical approach. At each incremental step, some grains are fully reoriented by twinning provided certain conditions are fulfilled. The

'effective twinned fraction' $V^{eff,mode}$ is the volume associated with the fully reoriented grains for the mode, and a threshold volume fraction is defined as

$$V^{th,mode} = A^{th1} + A^{th2} \frac{V^{eff,mode}}{V^{acc,mode}} \quad (2.4.11)$$

where A^{th1} and A^{th2} are two material constants. After each deformation increment a grain is randomly selected and the twin system with the highest accumulated volume fraction is identified. If the latter is larger than the threshold $V^{th,mode}$ the grain is allowed to reorient, and $V^{eff,mode}$ and $V^{acc,mode}$ are updated accordingly. The process is repeated until either all grains are checked or the effective twin volume exceeds the accumulated twin volume. In the latter case reorientation by twinning is ceased and the next deformation step is considered. Two things are achieved in this process: a) only the historically most active twin system in each grain is considered for reorienting the whole grain by twinning, and b) the twinned fraction is consistent with the shear activity that the twins contribute to deformation.

As stated earlier, different choices are possible for the local linearized behavior at grain level [see (2.2.20)]. Evidently, results of the self-consistent scheme depend on this choice. The following are the linearization schemes commonly implemented in self-consistent models and are used in the present Chapter.

a) Secant (Hutchinson, 1976):

$$A_{ijkl}^{v\Omega,sec} = A_{ijpq}^{\Omega} (L_{pqmn}^{\Omega} M_{mnl}^{p\Omega} + N_{pmkl}^{p\Omega} \sigma_{mq}^{\Omega} - \sigma_{pm}^{\Omega} N_{mqkl}^{p\Omega}), \quad l_{ij}^{0\Omega,sec} = 0 \quad (2.4.12)$$

b) Affine (Masson et al., 2000; Lebensohn et al., 2004):

$$A_{ijkl}^{v\Omega,aff} = A_{ijkl}^{v\Omega,sec} / m, \quad l_{ij}^{0\Omega,aff} = (1 - 1/m) A_{ijkl}^{v\Omega,sec} \sigma_{kl}^{\Omega} \quad (2.4.13)$$

c) Tangent (Lebensohn and Tomé, 1993):

$$A_{ijkl}^{v\Omega,tg} = A_{ijkl}^{v\Omega,sec} / m, \quad l_{ij}^{0\Omega,tg} = 0 \quad (2.4.14)$$

The interaction tensor (3.17) is thus given by

$$\hat{M}^{v\Omega} = (\mathbf{I} - \mathbf{T}^{v\Omega})^{-1} \mathbf{T}^{v\Omega} \mathbf{M}^{v,sec} / m \quad (2.4.15)$$

d) 'm-effective' scheme (Tomé, 1999):

This scheme is modified from the Tangent scheme by replacing the rate sensitivity m with m^{eff} :

$$\hat{M}^{v\Omega} = (\mathbf{I} - \mathbf{T}^{v\Omega})^{-1} \mathbf{T}^{v\Omega} \mathbf{M}^{v,sec} / m^{eff} \quad (2.4.16)$$

Here, m^{eff} is introduced to allow the strength of interaction between the inclusion and the HEM to be adjustable. The scheme would produce a rigid upper bound solution when $m^{eff} = \infty$. If $m^{eff} = m$ is assumed, this scheme reduces to the Tangent scheme.

2.5 Results and Discussions

The proposed EVPSC model has been implemented in a Material Point Simulator, EVPSC_MPS. Numerical results reported in this section are mainly for validation of the EVPSC model. As mentioned previously, the proposed EVPSC model is a general rate-sensitive self-consistent polycrystal plasticity model valid at arbitrary large deformations. With the specific constitutive functions for describing slip/twinning hardening in the present Chapter being taken to be the same as in the VPSC model (see Section 2.4), the main difference between the EVPSC and VPSC is the elastic deformation, which becomes negligible at large strains. It is thus expected that the difference in predictions between EVPSC and VPSC at large strains is small for proportional loadings. Therefore, the EVPSC model can be efficiently validated by comparing its predictions to those based on the VPSC model. However, some cases in which the VPSC model cannot be applied but the EVPSC works well, will be also considered here.

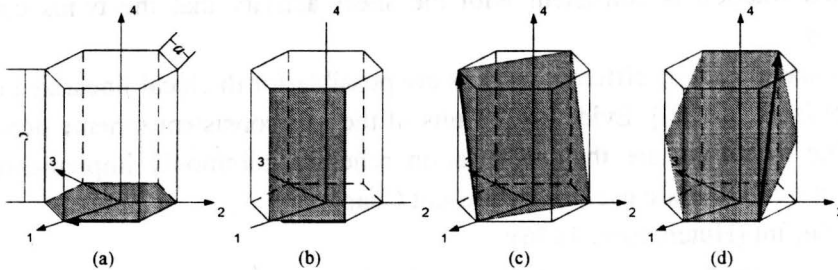


Figure 2.1 Plastic deformation modes in hexagonal structure, (a) Basal; (b) Prismatic; (c) Pyramidal; and (d) extension Twin.

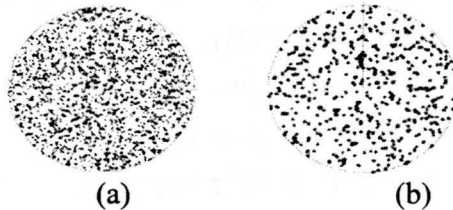


Figure 2.2 (a) Initial texture of the FCC polycrystal with 2000 grains in terms of $\{111\}$ pole figures, and (b) HCP polycrystal with 500 grains in terms of $\{0001\}$ pole figure.

We consider both FCC and HCP polycrystals with randomly distributed grain orientations in their initial states. The plastic deformation in FCC materials is assumed to be resulted from slip in the usual $\{111\}\langle 110 \rangle$ slip systems. For HCP materials we assume that plastic deformation is due to slip in the in the Basal $\langle a \rangle$ ($\{1001\}\langle 11\bar{2}0 \rangle$), Prismatic $\langle a \rangle$ ($\{10\bar{1}0\}\langle 11\bar{2}0 \rangle$) and Pyramidal $\langle c+a \rangle$ ($\{\bar{1}\bar{1}22\}\langle \bar{1}\bar{1}23 \rangle$) slip systems, and the $\{10\bar{1}2\}\langle \bar{1}011 \rangle$ extension twin system (see **Figure 2.1**). It is noted that Pyramidal $\langle a \rangle$ ($\{\bar{1}\bar{1}01\}\langle 11\bar{2}0 \rangle$) slip system is frequently referred to in the

magnesium literature. However, it has been reported that the Prismatic $\langle a \rangle$ is more important than Pyramidal $\langle a \rangle$ slip (Ward Flynn et al., 1961). Furthermore, as pointed out by Agnew et al. (2001), the kinds of deformations and crystallographic textures induced by Pyramidal $\langle a \rangle$ slip could also be resulted from a combination of Basal $\langle a \rangle$ slip and Prismatic $\langle a \rangle$ slip. Therefore, Pyramidal $\langle a \rangle$ is not included here.

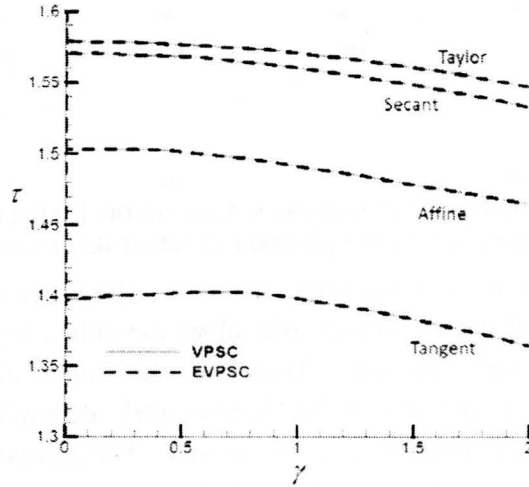


Figure 2.3 Predicted shear stress - strain curves under simple shear (2.5.3) for the FCC polycrystal.

Figure 2.2a shows the initial random textures in $\{111\}$ pole figure using 2000 grains for the FCC polycrystal, and in $\{0001\}$ pole figure in terms of 500 crystals for the HCP polycrystal. The following homogeneous deformations, governed by the velocity gradient I , are considered.

Axisymmetric tension/compression:

$$I_{ij} = \dot{\epsilon} \begin{bmatrix} 1 & 0 & 0 \\ 0 & -0.5 & 0 \\ 0 & 0 & -0.5 \end{bmatrix} \quad (2.5.1)$$

Plane strain tension/compression:

$$I_{ij} = \dot{\epsilon} \begin{bmatrix} 1 & 0 & 0 \\ 0 & 0 & 0 \\ 0 & 0 & -1 \end{bmatrix} \quad (2.5.2)$$

Simple shear:

$$I_{ij} = \dot{\gamma} \begin{bmatrix} 0 & 1 & 0 \\ 0 & 0 & 0 \\ 0 & 0 & 0 \end{bmatrix} \quad (2.5.3)$$

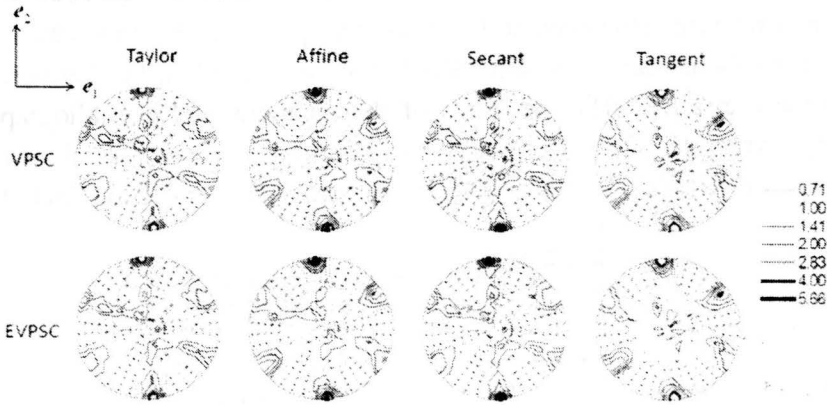


Figure 2.4 Predicted deformation textures in terms of the $\{111\}$ pole figure for the FCC polycrystal under simple shear (2.5.3) at shear strain of 2.

It is noted that the deformations considered above are incompressible. For an incompressible material, a constitutive model alone can only determine the stress state up to an arbitrary hydrostatic pressure. Therefore, the true/applied stress tensor $\bar{\sigma}$ is decomposed into the stress tensor σ that is completely determined by the constitutive model and an additional pressure p , i.e. $\bar{\sigma} = \sigma + pI$. The additional pressure p is to be determined from the boundary conditions. For example, under the plane strain compression (2.5.2), the boundary condition $\bar{\sigma}_{11} = \sigma_{11} + p = 0$ results in $p = -\sigma_{11}$. Therefore, the applied compression stress is calculated by $\bar{\sigma}_{33} = \sigma_{33} - \sigma_{11}$. However, it is important to be noted that using $\bar{\sigma}$ or σ to present numerical results is not critical here because the main purpose of this section is to validate the proposed EVPSC model and to demonstrate its unique constitutive features.

Although anisotropic elasticity (2.4.3) is included in the EVPSC model, numerical results presented in this section assume that elasticity is isotropic to simplify the discussion. We use a Young's modulus $E = 2 \times 10^5$ MPa and Poisson's ratio $\nu = 0.3$. We further assume that the reference value of the slip/twinning rate is $\dot{\gamma}_0 = 0.001 \text{ s}^{-1}$, and the rate sensitivity is taken to be $m = 0.05$. In all the simulations, stresses and stress associated quantities are in the unit of MPa.

We start by considering the FCC polycrystal without twinning. The hardening parameters are chosen as: $\tau_0 = 1$, $\tau_1 = 0$, $h_0 = 0$, $h_1 = 0$ and $h^{\alpha\beta} = 1$, which implies that there is no hardening at the slip system level. It is noted that with the values of the Young's modulus and the initial critical resolved shear stress used, $E/\tau_0 = 2 \times 10^5$, responses of the FCC polycrystal are expected to be nearly rigid plastic, and the predictions based on the EVPSC model should be almost the same as those based on the VPSC model, even at small strains. **Figure 2.3** shows the predicted shear stress $\tau = \sigma_{12}$ and shear strain $\gamma = 2\varepsilon_{12}$ curves, based on both the EVPSC and VPSC models with

various self-consistent schemes, for the FCC polycrystal under simple shear (2.5.3) with $\dot{\gamma} = 0.001 \text{ s}^{-1}$. For a comparison, the Taylor (or full constraint) model is also included. It is clear that the results based on the EVPSC and VPSC are almost identical. Among the self-consistent schemes, the Tangent gives a very soft response, while the prediction based on the Secant scheme is very hard and close to the one according to the Taylor mode. The calculated shear stress and shear strain curve using the Affine method is in between those based on the Tangent and Secant schemes. The predicted deformed textures at shear strain $\gamma = 2$ are presented in Figure 2.4. It is found that they are all the typical shear texture in FCC polycrystals, and that the differences in predicted textures between the EVPSC and VPSC are negligible.

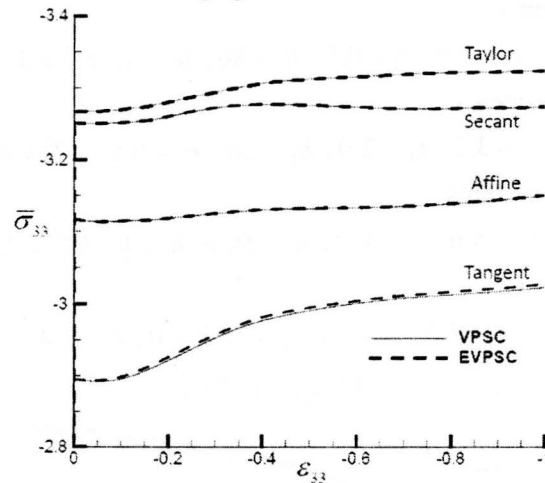


Figure 2.5 Predicted stress - strain curves under plane strain compression (2.5.2) for the FCC polycrystal.

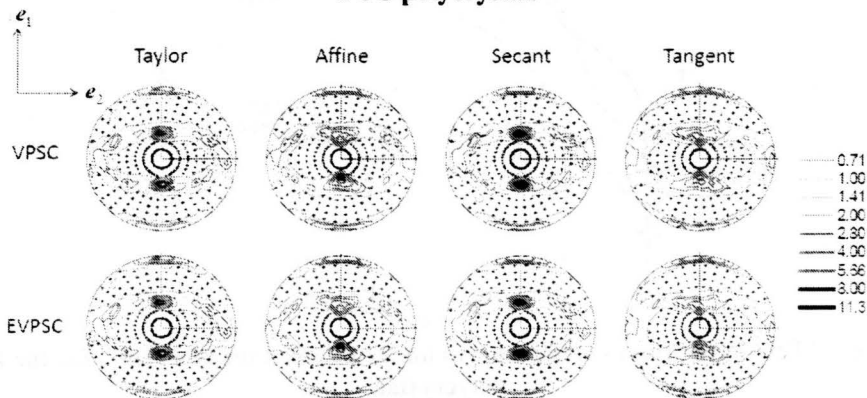


Figure 2.6 Predicted deformation textures in terms of the $\{111\}$ pole figure for the FCC polycrystal under plane strain compression (2.5.2) at compressive strain of -1.

The responses of the FCC polycrystal under plane strain compression (2.5.2) with $\dot{\epsilon} = 0.001 \text{ s}^{-1}$ are shown in Figure 2.5 and Figure 2.6. From the predicted stress $\bar{\sigma}_{33}$ and strain $\bar{\epsilon}_{33}$ curves in Figure 2.5, it is found that there is no noticeable difference between

the EVPSC and VPSC. Furthermore, as already found in the simple shear shown in **Figure 2.3**, the Secant scheme is very stiff and close to the Taylor, the Tangent is very soft, while the Affine is in between the Secant and Tangent. Again, differences in the predicted deformed textures at $\varepsilon_{33} = -1$ between the EVPSC and VPSC are very small. However, it is interesting to note that the Affine self-consistent scheme captures the diffuse 'peanut-like' shape in the experimental $\{111\}$ pole figure for FCC polycrystalline materials.

We proceed by studying an HCP polycrystal with the initial texture shown in **Figure 2.2b**. The values of the hardening parameters are those reported by Jain and Agnew for magnesium AZ31B sheet at room temperature, namely:

Basal slip systems:

$$\tau_0 = 1.0, \tau_1 = 0.5, h_0 = 80, h_1 = 3, h^{\alpha\beta} = 4$$

Prismatic slip systems:

$$\tau_0 = 3.2, \tau_1 = 2.0, h_0 = 20, h_1 = 0.5, h^{\alpha\beta} = 4$$

Pyramidal slip systems:

$$\tau_0 = 5.0, \tau_1 = 6.0, h_0 = 500, h_1 = 0, h^{\alpha\beta} = 2$$

Twinning systems:

$$\tau_0 = 1.5, \tau_1 = 0, h_0 = 0, h_1 = 0, h^{\alpha\beta} = 4$$

$$A^{th1} = 1, A^{th2} = 0$$

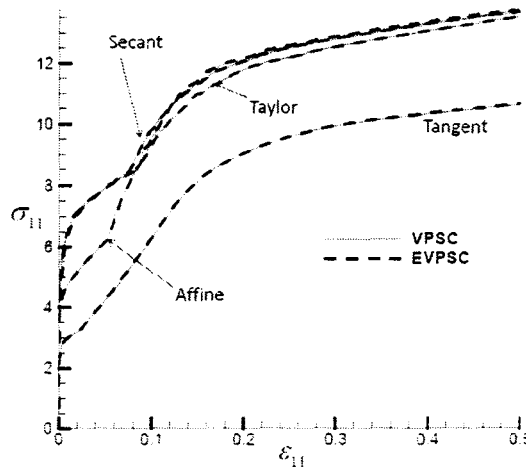


Figure 2.7 Predicted stress - strain curves under uniaxial tension (2.51) for the HCP polycrystal.

Figure 2.7 shows the predicted stress and strain curves, in terms of σ_{11} and ε_{11} , for the HCP polycrystal under axisymmetric tension (2.5.1) with $\dot{\varepsilon} = 0.001s^{-1}$. It is observed that EVPSC and VPSC give virtually the same results. Among the various self-consistent schemes, the Tangent method predicts a very soft response. At small strains,

the Secant is very close to the Taylor and shows a high stiffness, and the Affine is in between the Tangent and Secant. However, at large strains, the prediction based on the Affine is very close to that by the Secant method and is above the Taylor model. **Figure 2.8** presents the predicted deformed textures at $\epsilon_{11} = 0.5$. The differences in between the EVPSC and VPSC are negligible. It is interesting to note that the crossings of Affine with Taylor and Secant as well as Secant with Taylor, shown in **Figure 2.7**, are due to the twinning. In the corresponding simulations without the twinning, these crossings are disappeared (see **Figure 2.9**). **Figure 2.10** and **Figure 2.11** show the predicted stress and strain curves (in terms of $\bar{\sigma}_{33}$ and ϵ_{33}) and deformed textures at $\epsilon_{33} = -0.5$ for the HCP polycrystal under plane strain compression (2.5.2) with $\dot{\epsilon} = 0.001 \text{ s}^{-1}$, respectively. Again, EVPSC and VPSC predict quite similar results.

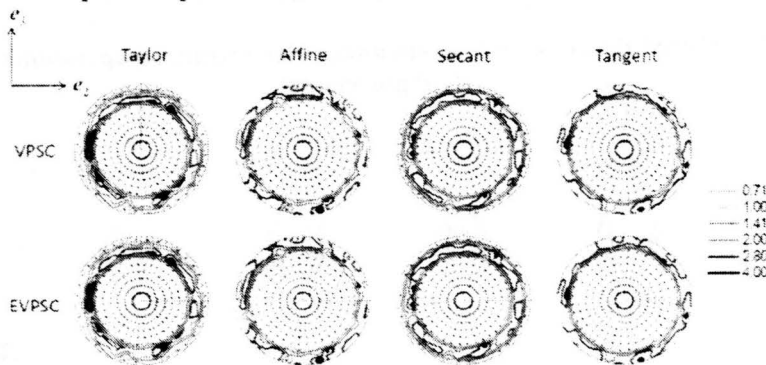


Figure 2.8 Predicted deformation texture in terms of the {0001} pole figure for the HCP polycrystal under axisymmetric tension (2.5.1) at tensile strain of 0.5.

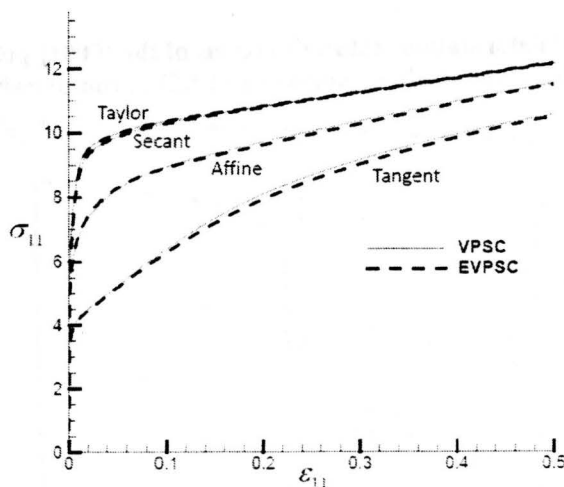


Figure 2.9 Predicted stress - strain curves under axisymmetric tension (2.5.1) for the HCP polycrystal.

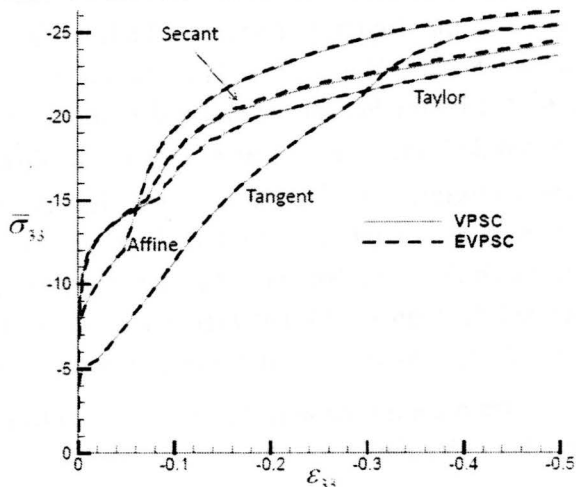


Figure 2.10 Predicted stress - strain curves under plane strain compression (2.5.2) for the HCP polycrystal.

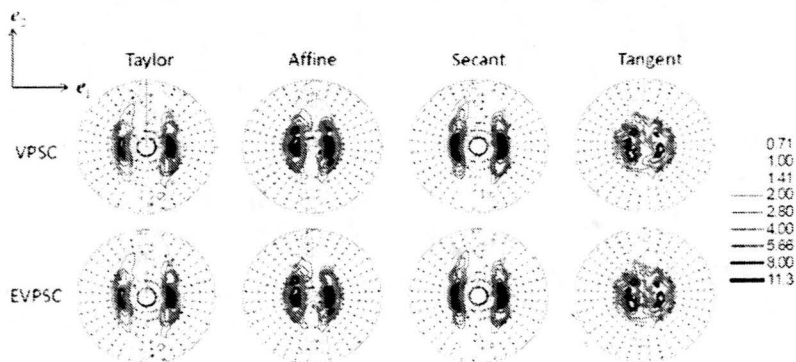


Figure 2.11 Predicted deformation textures in terms of the {0001} pole figure for the HCP polycrystal under plane strain compression (2.5.2) at compressive strain of -0.5.

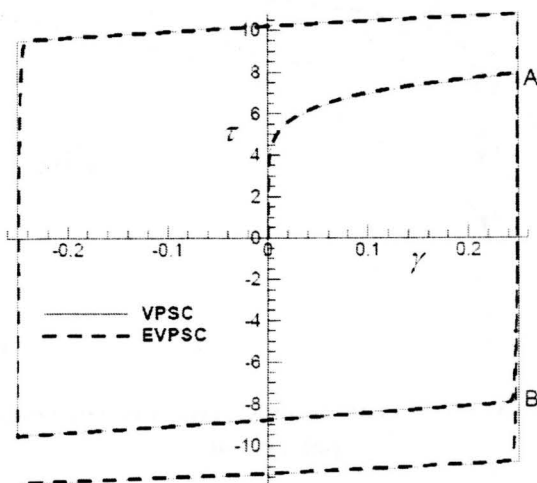


Figure 2.12 Predicted shear stress - strain curves under cyclic simple shear (2.5.3) for the HCP polycrystal.

The deformations in all the above simulations are monotonic, and the differences between EVPSC and VPSC are very small at large strains. In the following two examples, we will analyze a case showing intrinsic differences between EVPSC and VPSC. In these examples, we consider the HCP polycrystal but the plastic deformation is assumed to be accommodated entirely by slip. In other words, extension twinning is not included. Among the linearization schemes presented in Section 2.4, only the Affine method is considered.

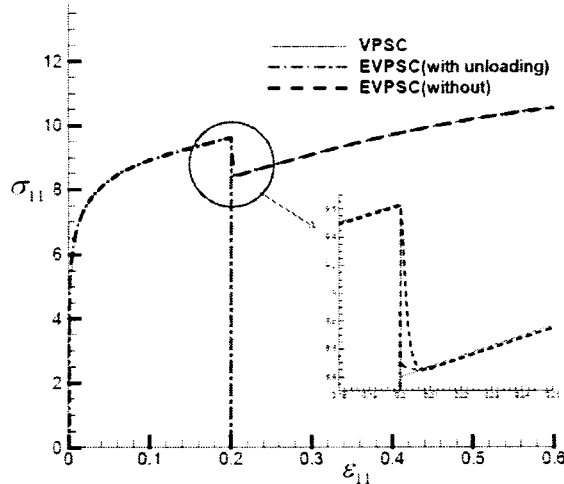


Figure 2.13 Predicted effect of axisymmetric tension pre-straining (2.5.1) on subsequent plane strain tension (2.5.2) for the HCP polycrystal.

Figure 2.12 presents the calculated shear stress τ and shear strain γ curves for the HCP polycrystal under cyclic simple shear (2.5.3) with $\dot{\gamma} = \pm 0.001 \text{ s}^{-1}$. The main difference, small but significant, between EVPSC and VPSC is observed at the moment when the applied shear rate $\dot{\gamma}$ is reversed, where an elastic unloading is expected. More specifically, EVPSC shows a smooth transition due to the elastic deformation when the applied shear rate $\dot{\gamma}$ is reversed. Based on the VPSC model, however, the shear stress on the shear stress and shear strain curve has to jump from A to B with $\tau_B = -\tau_A$ (see Figure 2.12), because stresses intermediate between points A and B cannot be obtained when the shear rate is discontinuously reversed from 0.001 s^{-1} to -0.001 s^{-1} .

Figure 2.13 shows the effect of strain path change on the calculated stress and strain curves. In the simulations, the HCP polycrystal is first stretched in axisymmetric tension (2.5.1) with $\dot{\epsilon} = 0.001 \text{ s}^{-1}$ up to $\epsilon_{11} = 0.2$ and then is loaded in plane strain tension (2.5.2) with $\dot{\epsilon} = 0.001 \text{ s}^{-1}$ up to $\epsilon_{11} = 0.6$. Two types of strain path changes are considered: in one the strain path is immediately changed from axisymmetric tension to plane strain tension at $\epsilon_{11} = 0.2$; in the other, following axisymmetric tension up to $\epsilon_{11} = 0.2$, the HCP polycrystal is first unloaded completely and then re-loaded in plane

strain tension. Due to the fact that the VPSC model lacks elasticity, it cannot distinguish any differences between performing or not the unloading after the pre-straining. Furthermore, VPSC shows no smooth transition in the calculated stress strain curve upon the strain path change, but a discontinuous jump from uniaxial yield tension to plane strain yield tension. Based on the EVPSC model, the differences in the transition region between unloading or not are clearly observed. Although not shown here, the textures predicted by EVPSC and VPSC are quite similar, since the elastic deformations associated with the unloading and strain path change are small.

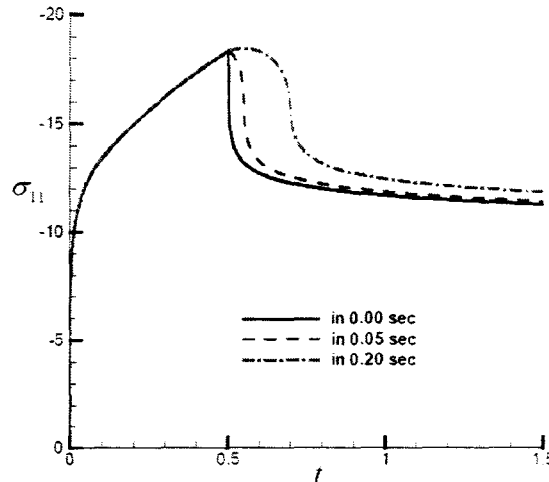


Figure 2.14 Predicted stress - time curves for a stress relaxation test during axisymmetric compression (2.5.1) of the HCP polycrystal.

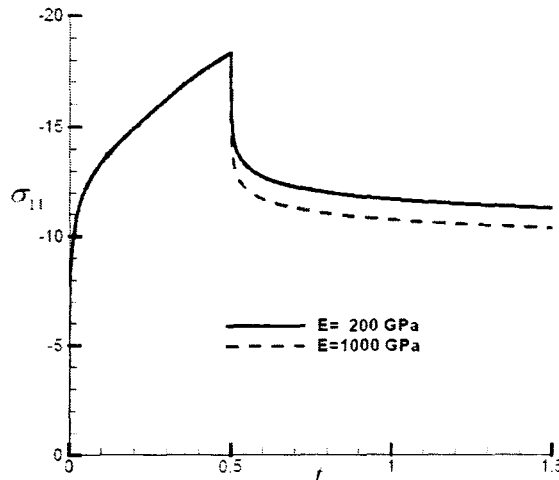


Figure 2.15 Predicted effect of Young's modulus E on stress responses for a stress relaxation test during axisymmetric compression (2.5.1) of the HCP polycrystal.

Finally, we will present a case, in which the VPSC model cannot be applied but EVPSC works well. Figure 2.14 shows the predicted stress σ_{11} and time t curves for a stress relaxation test following uniaxial compression (2.5.1) of the HCP polycrystal with

$\dot{\epsilon} = -1.0 \text{ s}^{-1}$ of the HCP polycrystal. The HCP polycrystal is deformed under uniaxial compression up to time $t = 0.5 \text{ s}$. The imposed macroscopic strain rate is then reduced to zero linearly in three different time intervals: 0.0 s, 0.05 s and 0.20 s. To maintain the constant applied deformation, due to the viscous nature of the EVPSC model, the inelastic strains during relaxation increase with time at the expense of the reduction of the elastic strains. The stress level decays with time as the elastic strains relax, with the shape of the stress vs. time curve depending on the reduction time of the load. Nevertheless, the different curves in the relaxation stage will eventually merge.

Figure 2.15 presents the effect of Young's modulus E on the predicted stress and time curves. In the simulations, the imposed macroscopic deformation rate is reduced to zero instantaneously at time $t = 0.5 \text{ s}$. The results reported in **Figure 2.15** are a direct consequence of the dependence of the relaxation time on the ratio of the effective viscosity of the plastic behavior to the elastic modulus. If the VPSC model is applied, the stress will instantaneously jump vertically down to zero, because no elastic strain is included in this model. It is also worthwhile to be mentioned that the extended EPSC model by Neil et al. (2010) is not able to simulate the stress relaxation test because the rate-insensitive character of the constitutive laws upon which EPSC is based.

2.6 Conclusions

In this Chapter, we have developed a finite strain elastic-viscoplastic self-consistent model (EVPSC) for polycrystalline materials. At the grain level, both slip and twinning are included as the plastic deformation mechanisms, while elastic anisotropy is accounted for in the elastic moduli. The transition from single crystal to polycrystal is based on a completely self-consistent approach based on an approximate interaction equation originally proposed by Kouddane et al (1993). The elastic-viscoplastic response was formulated self-consistently combining the results of the elastic and the viscoplastic self-consistent formulations described in Section 2.3.

We have numerically validated the proposed EVPSC model. As expected, at large monotonic strains elasticity saturates and the EVPSC model gives results very close to the VPSC model: the differences in the predicted stress-strain curves and texture evolution are negligible for monotonic loadings. For deformations involving elastoplastic transients associated with unloading and strain path changes, EVPSC predicts clear and gradual transitions, while VPSC gives stress discontinuities due to lack of elastic deformation. We have also demonstrated, through the simulation of a stress relaxation test in HCP, that the proposed EVPSC model captures the effect of strain rate and elastic stiffness in the macroscopic mechanical response.

We would like to emphasize that the main contribution of the present Chapter is a completely general elastic-viscoplastic, fully anisotropic, self-consistent polycrystal model, applicable at large strain and to any crystal symmetry. The proposed EVPSC

model is very flexible to implement sophisticated descriptions for slip, twinning, and hardening. Future work contemplates using the EVPSC model to predict the evolution of lattice strains during loading, and to validate the model by comparing the predicted lattice strains to those measured experimentally. Among other things, we expect to elucidate the influence that holding times and stress relaxation may have during in situ neutron diffraction experiments. This work is in progress and will be reported elsewhere.

Finally, it is worthwhile to mention that Finite Element (FE) crystal plasticity models are sometimes used as an alternative to the effective medium polycrystal plasticity model described in this work. In FE simulations an element of the finite element mesh represents either a single crystal or a part of a single crystal, and the constitutive response at an integration point is described by the single crystal constitutive model. This approach enforces both equilibrium and compatibility throughout the polycrystalline aggregate in the weak finite element sense (Anand and Kalidindi, 1994; Wu et al., 2004b). This approach facilitates taking into account grain morphology and modeling of localized deformations in single and polycrystals (Wu et al., 2006; Wu et al., 2007a). In addition, the validity of a polycrystal plasticity model can be assessed by comparing numerical results predicted by the polycrystal plasticity theory and the corresponding FE simulation. However, such an FE simulation is computationally much more intensive than the corresponding self-consistent calculation.

Chapter 3. Evaluation of self-consistent polycrystal plasticity models for magnesium alloy AZ31B sheet

Abstract — Various self-consistent polycrystal plasticity models for hexagonal close packed (HCP) polycrystals are evaluated by studying the deformation behavior of magnesium alloy AZ31B sheet under different uniaxial strain paths. In all employed polycrystal plasticity models both slip and twinning contribute to plastic deformation. The material parameters for the various models are fitted to experimental uniaxial tension and compression along the rolling direction (RD) and then used to predict uniaxial tension and compression along the traverse direction (TD) and uniaxial compression in the normal direction (ND). An assessment of the predictive capability of the polycrystal plasticity models is made based on comparisons of the predicted and experimental stress responses and R values. It is found that, among the models examined, the self-consistent models with grain interaction stiffness halfway between those of the limiting Secant (stiff) and Tangent (compliant) approximations give the best results. Among the available options, the Affine self-consistent scheme results in the best overall performance. Furthermore, it is demonstrated that the R values under uniaxial tension and compression within the sheet plane show a strong dependence on imposed strain. This suggests that developing anisotropic yield functions using measured R values must account for the strain dependence.

3.1 Introduction

Constitutive modeling of the plastic deformation of Hexagonal Close Packed (HCP) crystals is much more complicated than that in most Face Centered Cubic (FCC) and Body Centered Cubic (BCC) crystals. More specifically, plastic deformation in most FCC and BCC materials is dominated by crystallographic slip, while both slip and twinning contribute to plastic deformation in HCP crystals. Furthermore, due to its low symmetry of crystallographic structure, different types of slip systems exist in an HCP crystal although very few slip systems could be activated at room temperature. At the polycrystal level, an additional difficulty in constitutive modeling for HCP polycrystals is that one must carefully take into account the details of the interaction between crystals/grains, because the effects of these details are more significant than in FCC and BCC materials due to low crystallographic symmetry and high anisotropy in the mechanical behavior of individual grains.

Various polycrystal plasticity models have been developed for polycrystals. Among them, the classic Taylor model (Taylor, 1938) has been the most used, for historic reasons and because of its easy implementation. The Taylor model assumes that all grains must accommodate the same plastic strain equal to the macroscopically imposed strain. This implies that the Taylor model neglects strain variations from grain to

grain in the polycrystalline aggregate. As a consequence, the Taylor model does not consider the interaction between crystals, which is believed to be less significant in FCC and BCC materials due to their high crystallographic symmetries. The Taylor model has played an important role in the field of modeling of forming of aluminum and steel sheets (Wu et al., 1997; Dawson et al., 2003; Eyckens et al., 2009; Levesque et al., 2010). For metals like HCP polycrystals with low crystallographic symmetry, stress and strain variations from grain to grain and interaction among grains in a polycrystalline aggregate are significant and cannot be neglected in an attempt to accurately describe deformation behavior. Consequently, polycrystal plasticity models based on the self-consistent approach originally proposed by Kröner (1958), for the elastic case, and later extended to the elastoplastic (Hill, 1965) and viscoplastic (Hutchinson, 1976), are becoming more popular than the Taylor model when modeling HCP polycrystals. In general, self-consistent models allow for different strain response in each grain, depending on the relative stiffness between the grain and a surrounding homogeneous equivalent medium (HEM). The consistency conditions require that the averaged behavior over all the grains must be the same as the macroscopically imposed one. Among various self-consistent plasticity models, the Visco-Plastic Self-Consistent (VPSC) model developed by Molinari et al. (1987) and extended by Lebensohn and Tomé (1993; Lebensohn and Tomé, 1994) to account for anisotropy, has been widely used to simulate large strain behavior and texture evolution of HCP polycrystalline Mg under various deformation modes (Agnew and Duygulu, 2005; Jain and Agnew, 2007; Neil and Agnew, 2009; Proust et al., 2009; Signorelli et al., 2009). Recently, Wang et al. (2010e) have developed a finite strain Elastic-Viscoplastic Self-Consistent (EVPSC) model for polycrystalline materials. The EVPSC model is a completely general elastic-viscoplastic, fully anisotropic, self-consistent polycrystal model, applicable at large strain and to any crystal symmetry. However, it has been found that numerical results are extremely sensitive to the stiffness of the grain-matrix interaction associated with the various Self-Consistent Schemes (SCSs) (Wang et al., 2010e). Therefore, it is necessary to carry out an assessment of the predictive capability of the VPSC/EVPSC model with various SCSs including Secant, Affine, Tangent and the effective interaction m^{eff} .

It is worth mentioning that various SCSs have been evaluated by comparing their predictions, in terms of mechanical responses and texture evolutions, with finite element calculations, full field simulations or available experimental evidence for polycrystals (Molinari and Toth, 1994; Tomé, 1999; Lebensohn et al., 2007). It has been found that Secant and Tangent SCSs, among the first-order SCSs, exhibit asymptotic trend to respectively the upper-bound and lower-bound in the rate-insensitive limit, and thus are not appropriate for highly anisotropic materials like HCP polycrystals. The intermediate SCSs, Affine and m^{eff} give better overall predictions, if appropriate artificial parameter m^{eff} is assigned according to results of finite element calculations (Molinari and Toth,

1994) or relative directional compliance approach (Tomé, 1999). It has to be noted that those evaluations were based on the assumption that all the material parameters at single crystal level are the same for various SCSs. A real challenge in modeling HCP polycrystals is that it is almost impossible to directly measure the single crystal properties. It has been generally accepted that the differences in stress experienced by differently orientated single crystals in an HCP polycrystal are mainly due to the orientation of a single crystal and the interaction of the single crystal with its surrounding grains. The interaction is, of course, dependent on the self-consistent scheme employed. Therefore, for a textured HCP polycrystal, the only practical way to determine the single crystal properties in a polycrystal plasticity model is by curve-fitting numerical simulations based on the polycrystal model to the corresponding macroscopic experimental data (Xu et al., 2008). The predicative capability of the polycrystal plasticity model is then assessed by comparing its predictions based on the fitted material constants to the corresponding experiment data other than those used in the fitting. To the best of our knowledge, an assessment for the VPSC and EVPSC models with various SCSs has not been systematically carried out for Mg alloys. However, it is clear that such an assessment is meaningful only if the number of experiments employed is large enough to cover various different deformation processes for a given material. Here, we use for such matter the Mg alloy AZ31B in sheet form, thoroughly characterized experimentally by Jain and Agnew (2007).

In the present study, various self-consistent polycrystal plasticity models for HCP polycrystals are evaluated by studying large strain behavior of magnesium alloy AZ31B sheet under different deformation processes. In all the polycrystal plasticity models employed, both slip and twinning are assumed to contribute to plastic deformations. Values of the material parameters for the various models are fitted to experimental uniaxial tension and compression along the rolling direction (RD) and then used to predict uniaxial tension and compression along the traverse direction (TD) and uniaxial compression in the normal direction (ND). An assessment of the predictive capability of the polycrystal plasticity models is made based on comparisons of the predicted and experimental stress responses and R values. Differences between the predictions of different models are emphasized. For the polycrystal plasticity model with the so-called effective interaction “ m^{eff} ” scheme, a broader set of parameters is obtained by best fitting to the experimental stress-strain curves and R values under slip dominated cases of uniaxial tension along the RD and TD and uniaxial compression along the ND. This final exercise permits illustration of the continuum of results which are possible and, notably, span the space between the secant and tangent approximations.

3.2 Polycrystal plasticity models

Wang et al. (2010e) have shown that the differences in the predicted stress-strain curves and texture evolutions based on the EVPSC and the VPSC models are negligible at large strains for monotonic loadings. For deformations involving unloading and strain path changes, the EVPSC predicts a continuous elasto-plastic transition, while the VPSC model gives a discontinuous response due to the lack of elastic deformation. It has been also demonstrated that the EVPSC model can capture some important experimental features associated with elasto-plastic transitions, stress relaxation, and unload, which cannot be simulated with the VPSC model (Wang et al., 2010e). Since the deformations studied in the present Chapter do not involve unloading or strain path changes, our assessment of the predictive capability of the VPSC model with various SCSs also applies to the EVPSC model with the corresponding SCS. For simplicity, the polycrystal SCSs described in what follows refer to the VPSC case.

Plastic deformation of a crystal is assumed to be due to the crystallographic slip and twinning on slip and twinning systems (s^α, n^α). Here, s^α and n^α are respectively the slip/twinning direction and normal direction of the slip/twinning system α in the present configuration. The following equation gives the grain (crystal) level plastic strain rate d^g (Asaro and Needleman, 1985):

$$d^g = \sum_{\alpha} \dot{\gamma}^{\alpha} P^{\alpha} \quad (3.1)$$

where $\dot{\gamma}^{\alpha}$ is the shear rate of slip (twinning) system α , and P^{α} is the associated Schmid tensor:

$$P^{\alpha} = (s^{\alpha} n^{\alpha} + n^{\alpha} s^{\alpha})/2 \quad (3.2)$$

For slip,

$$\dot{\gamma}^{\alpha} = \dot{\gamma}_0 \left| \tau^{\alpha} / \tau_{cr}^{\alpha} \right|^{(1/m)} \text{sgn}(\tau^{\alpha}) \quad (3.3)$$

and for twinning,

$$\dot{\gamma}^{\alpha} = \begin{cases} \dot{\gamma}_0 (\tau^{\alpha} / \tau_{cr}^{\alpha})^{(1/m)} & \text{for } \tau^{\alpha} > 0 \\ 0 & \text{for } \tau^{\alpha} \leq 0 \end{cases} \quad (3.4)$$

where $\dot{\gamma}_0$ is a reference value of slip/twinning rate, m is the slip/twinning rate sensitivity, and τ^{α} is the resolved shear stress defined by the product of Cauchy stress σ^g in grain g and P^{α} :

$$\tau^{\alpha} = \sigma^g : P^{\alpha} \quad (3.5)$$

τ_{cr}^{α} is the critical resolved shear stress (CRSS), sgn is the sign function. The evolution of τ_{cr}^{α} is taken in the form of

$$\dot{\tau}_{cr}^{\alpha} = \frac{d\hat{\tau}^{\alpha}}{d\gamma_{ac}} \sum_{\beta} h^{\alpha\beta} \dot{\gamma}^{\beta} \quad (3.6)$$

where $\gamma_{ac} = \sum_{\alpha} |\gamma^{\alpha}|$ is the accumulated shear strain in the grain, $h^{\alpha\beta}$ is the latent hardening coupling coefficient which empirically accounts for the obstacles on system α associated with system β . $\hat{\tau}^{\alpha}$ is the threshold stress and is characterized by

$$\hat{\tau}^{\alpha} = \tau_0^{\alpha} + (\tau_1^{\alpha} + h_1^{\alpha} \gamma_{ac}) (1 - \exp(-h_0^{\alpha} \gamma_{ac} / \tau_1^{\alpha})) \quad (3.7)$$

Here, τ_0 , h_0 , h_1 and $\tau_0 + \tau_1$ are the initial CRSS, the initial hardening rate, the asymptotic hardening rate and the back-extrapolated CRSS, respectively. More complex hardening laws have been proposed for Zr by Beyerlein and Tomé (2008) and Proust et al. (2009). These laws regard grains as composite inclusions consisting of parent grain and twin bands and are not considered here. The main purpose of this Chapter is to analyze the grain-matrix interaction effects on mechanical response of HCP polycrystals rather than the role played by the hardening law.

Various homogenization methods have been developed to characterize the mechanical behavior of a polycrystalline aggregate from the responses of their single crystals. Among them, the most popular Taylor model assumes that the strains of each grain are equal to the imposed macroscopic strains, and the macroscopic stresses are the average of the stresses over all the grains. Another popular homogenizing method is the self-consistent approach, which assumes each grain as an ellipsoidal inclusion embedded in a homogeneous effective medium (HEM), which is the aggregate of the grains. The Eshelby inclusion formalism (Eshelby, 1957), modified for incompressible media by Lebensohn et al. (1998) is used to describe the interaction between each grain and the aggregate. During each deformation step, the single crystal constitutive rule, which describes the grain-level response, and the self-consistency criteria are solved simultaneously. This enables the grain-level stresses and strain rates to be consistent with the boundary conditions imposed on the surrounding polycrystalline aggregate.

To apply the inclusion formalism, in connection with the non-linear visco-plastic response, it is first necessary to linearize the response. For a comprehensive discussion and comparison of the different linearization procedures the reader is referred to Lebensohn et al. (2007). In this Section we only report the relevant equations and in the following Sections we concentrate on discussing the predictions of the different approaches for Mg AZ31, by comparison with available experimental information. The linearized behavior of an inclusion (single crystal) can be written as

$$\mathbf{d}^g = \mathbf{M}^g : \boldsymbol{\sigma}^g + \mathbf{d}_0^g \quad (3.8)$$

where \mathbf{M}^g and \mathbf{d}_0^g are the visco-plastic compliance and the back-extrapolated term of grain g , respectively. The linearized behavior of the HEM (polycrystal) is analogous to the inclusion and is written as

$$\mathbf{D} = \bar{\mathbf{M}} : \boldsymbol{\Sigma} + \mathbf{D}_0 \quad (3.9)$$

where $\bar{\mathbf{M}}$, \mathbf{D} , $\boldsymbol{\Sigma}$ and \mathbf{D}_0 are the visco-plastic compliance, strain rate, stress and the back-extrapolated term of the HEM, respectively.

Different SCSs depend on different choices for the linearization. Among various SCSs, the Secant SCS employs the following linearization:

$$\mathbf{M}_{ijkl}^{g,secant} = \dot{\gamma}_0 \sum_{\alpha} (\tau^{\alpha} / \tau_{cr}^{\alpha})^{(1/m-1)} P_{ij}^{\alpha} P_{kl}^{\alpha} / \tau_{cr}^{\alpha}, \quad \mathbf{d}_{0ij}^{g,secant} = 0 \quad (3.10)$$

while the Affine SCS applies the linearization:

$$\mathbf{M}_{ijkl}^{g,affine} = (\dot{\gamma}_0 / m) \sum_{\alpha} \sum_{\alpha} (\tau^{\alpha} / \tau_{cr}^{\alpha})^{(1/m-1)} P_{ij}^{\alpha} P_{kl}^{\alpha} / \tau_{cr}^{\alpha}, \quad \mathbf{d}_{0ij}^{g,affine} = (1 - 1/m) \mathbf{d}_{ij}^g \quad (3.11)$$

The relation of grain-level stress and strain rate to the aggregate response is obtained self-consistently by

$$(\mathbf{d}^g - \mathbf{D}) = -\tilde{\mathbf{M}} : (\boldsymbol{\sigma}^g - \boldsymbol{\Sigma}) \quad (3.12a)$$

with the interaction tensor $\tilde{\mathbf{M}}$ being given by

$$\tilde{\mathbf{M}} = (\mathbf{I} - \mathbf{S})^{-1} : \mathbf{S} : \bar{\mathbf{M}} \quad (3.12b)$$

where \mathbf{S} is the Eshelby tensor for a given grain, \mathbf{I} is the identity tensor. The condition that $\mathbf{D} = \langle \mathbf{d}^g \rangle$ and $\boldsymbol{\Sigma} = \langle \boldsymbol{\sigma}^g \rangle$ (where $\langle \dots \rangle$ denotes the volume average), leads to a self-consistent equation giving the macroscopic compliance as:

$$\bar{\mathbf{M}} = \langle \mathbf{M}^g : \mathbf{B}^g \rangle : \langle \mathbf{B}^g \rangle^{-1} \quad (3.13a)$$

with

$$\mathbf{B}^g = (\mathbf{M}^g + \tilde{\mathbf{M}}) : (\bar{\mathbf{M}} + \tilde{\mathbf{M}})^{-1} \quad (3.13b)$$

As can be seen in Eq. 3.12b, the interaction tensor $\tilde{\mathbf{M}}$ is approximately proportional to the macroscopic visco-plastic compliance $\bar{\mathbf{M}}$, which is itself given by a weighted average of the visco-plastic compliances, \mathbf{M}^g , of grains (Eq. 3.13a). As a consequence, a larger visco-plastic compliance for Affine SCS leads to a larger interaction tensor $\tilde{\mathbf{M}}$ and, as Eq. 3.12 indicates, will have associated a higher strain heterogeneity compared to Secant SCS. Clearly, since the macroscopic compliance is a weighted average of the single grain compliances, it will be of the same order of magnitude. An example of this is the relation: $\bar{\mathbf{M}}^{tangent} = \bar{\mathbf{M}}^{secant} / m$ (Hutchinson, 1976). As a consequence, the interaction tensor in the Tangent self-consistent scheme is given by:

$$\tilde{\mathbf{M}} = (\mathbf{I} - \mathbf{S})^{-1} : \mathbf{S} : \bar{\mathbf{M}}^{secant} / m \quad (3.14)$$

Based on the upper and lower limits represented by the Secant and Tangent approaches, Molinari and Tóth (1994) and Tomé (1999) explore using an empirical adjustable parameter m^{eff} , such that $m < m^{eff} < 1$. The m^{eff} scheme provides an intermediate interaction tensor:

$$\tilde{\mathbf{M}} = (\mathbf{I} - \mathbf{S})^{-1} : \mathbf{S} : \overline{\mathbf{M}}^{secant} / m^{eff} \quad (3.15)$$

For details concerning the self-consistent equations associated with the different visco-plastic self-consistent algorithms, we refer the interested reader to Lebensohn et al. (2007).

The Predominant Twin Reorientation (PTR) scheme proposed by Tomé et al. (1991) is used in the present Chapter to model the reorientation by twinning. Within each grain g , the PTR scheme tracks the shear strain $\gamma^{\alpha,g}$ contributed by each twinning system α , and the associated volume fraction $V^{\alpha,g} = \gamma^{\alpha,g} / \gamma^{tw}$ as well. Here γ^{tw} is the characteristic shear (constant) associated with twinning. Crystallographically equivalent twins belong to the same twin mode. For example, the $\{10\bar{1}2\}$ twinning systems which are activated by c-axis tension constitute the extension twin mode. The sum over all twin systems associated with a given twin mode, and then over all the grains, represents the 'accumulated twin fraction' $V^{acc,mode}$ in the aggregate for the particular twin mode:

$$V^{acc,mode} = \sum_g \sum_{\alpha} V^{\alpha,g} \quad (3.16)$$

In the PTR scheme developed by Tomé et al. (1991), after each deformation increment, a grain is randomly selected to check if the predominant twinning system exceeds a threshold value. If so, the grain is entirely reoriented to a new orientation according to predominant twinning system. The volume fraction of this reoriented grain is added to the so called 'effective twin fraction', $V^{eff,mode}$. The process is repeated until either all grains are checked or the effective twin fraction exceeds the accumulated twin fraction. In the latter case, the reorientation by twinning is ceased and the next deformation step is considered. The aforementioned threshold value is defined as

$$V^{th,mode} = A^{th1} + A^{th2} \frac{V^{eff,mode}}{V^{acc,mode}} \quad (17)$$

where A^{th1} and A^{th2} are two material constants. This approach statistically solves the practical problem that the number of orientations would grow continually if each activated twinning system was represented by a new orientation. Additionally, it maintains the twinned volume fraction at a level that is consistent with the shear activity of the twins contributing to the deformation.

For simplicity, VPSC models with Affine, Secant, Tangent and m^{eff} SCSs are respectively called Affine, Secant, Tangent and meff models in the rest of the present Chapter.

3.3 Results and Discussions

Table 3.1 List of material constants for various self-consistent models.

| Model | Mode | τ_0 | τ_1 | h_0 | h_1 | Latent | A^{th1} | A^{th2} |
|---------------------------|----------------|----------|----------|-------|-------|--------|-----------|-----------|
| Affine | Basal | 9 | 1 | 5000 | 25 | 4 | 0.72 | 0 |
| | Prismatic | 79 | 40 | 590 | 50 | 4 | | |
| | Pyramidal | 100 | 100 | 5000 | 0 | 2 | | |
| | Extension Twin | 47 | 0 | 0 | 0 | 4 | | |
| Secant | Basal | 13 | 4 | 5000 | 30 | 4 | 0.82 | 0 |
| | Prismatic | 73 | 35 | 400 | 60 | 4 | | |
| | Pyramidal | 110 | 83 | 2500 | 0 | 2 | | |
| | Extension Twin | 31 | 0 | 0 | 0 | 4 | | |
| meff ($m^{eff}=0.1$) | Basal | 17 | 6 | 3800 | 100 | 4 | 0.81 | 0 |
| | Prismatic | 77 | 33 | 650 | 50 | 4 | | |
| | Pyramidal | 148 | 35 | 9600 | 0 | 2 | | |
| | Extension Twin | 33 | 0 | 0 | 0 | 4 | | |
| Tangent | Basal | 21 | 5 | 3000 | 140 | 4 | 0.81 | 0 |
| | Prismatic | 90 | 15 | 580 | 70 | 4 | | |
| | Pyramidal | 145 | 30 | 9600 | 0 | 2 | | |
| | Extension Twin | 38 | 0 | 0 | 0 | 4 | | |

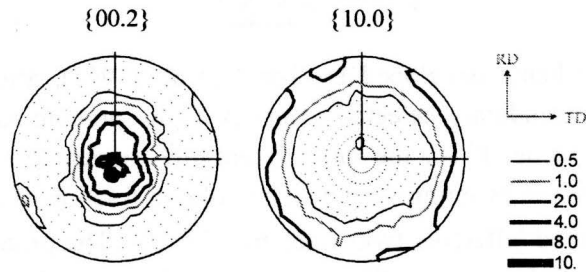


Figure 3.1 Initial texture of AZ31B sheet represented in terms of the $\{0001\}$ pole figure (a) and $\{10\bar{1}0\}$ pole figure (b).

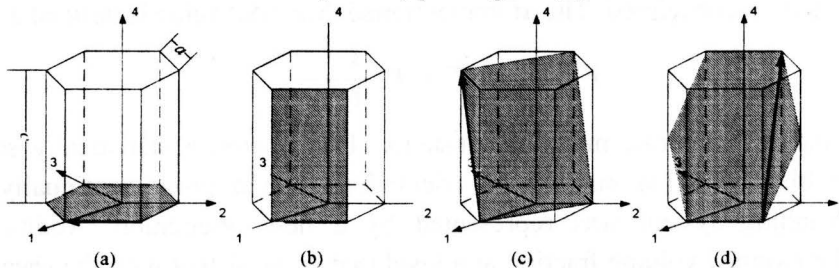


Figure 3.2 Plastic deformation modes in hexagonal structure: (a) Basal $\langle a \rangle$ slip systems, (b) Prismatic $\langle a \rangle$ slip systems, (c) Pyramidal $\langle c + a \rangle$ slip systems, and (d) extension twin.

The material studied in the present Chapter is magnesium alloy AZ31B sheet, which has a hexagonal crystallographic structure with $c/a=1.624$. The initial texture, shown in

Figure 3.1 as $\{0001\}$ and $\{10\bar{1}0\}$ pole figures, and the room temperature mechanical behavior of the sheet have been reported by Jain and Agnew (2007). Plastic deformation of AZ31B sheet is assumed to be due to Basal $\langle a \rangle$ ($\{0001\}\langle 11\bar{2}0 \rangle$), Prismatic $\langle a \rangle$ ($\{10\bar{1}0\}\langle 11\bar{2}0 \rangle$) and Pyramidal $\langle c+a \rangle$ ($\{11\bar{2}2\}\langle 11\bar{2}3 \rangle$) slip systems, and $\{10\bar{1}2\}\langle 10\bar{1}1 \rangle$ extension twin system (Figure 3.2). In all the numerical simulations reported in the present Chapter, uniaxial tension/compression is characterized by imposing the strain rate in the loading direction, while the only non-zero stress component is the normal stress along the loading direction. Thus, in addition to the normal strains in the width and thickness directions, three shear strains are allowed to develop in uniaxial tension/compression. The true stress and true plastic strain curves are plotted in terms of their absolute values.

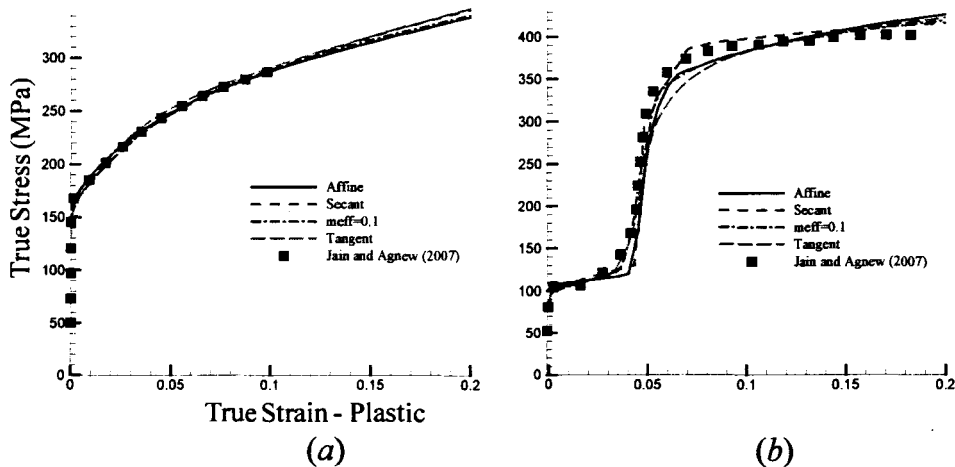


Figure 3.3 Stress and strain curves under (a) uniaxial tension, and (b) uniaxial compression along the RD.

In the present Chapter, the reference slip/twinning rate $\dot{\gamma}_0$ and rate sensitivity m are assumed to be the same for all slip/twinning systems, and are taken as $\dot{\gamma}_0=0.001s^{-1}$ and $m=0.05$, respectively. Values of the other material parameters in the Taylor and VPSC model with various SCSs are estimated by curve-fitting numerical simulations of uniaxial tension and compression along the RD to the corresponding experimental data. Although the fitting is done manually, using a systematic approach facilitates doing so. For example, during in-plane uniaxial tension of a sheet with strong basal texture, extension twinning and pyramidal slip occur rarely. Thus, uniaxial tension along the RD allows us to independently fit the material parameters associated with the basal and prismatic slip systems. On the other hand, uniaxial compression along the RD is dominated by twinning at small strains, while at large strains pyramidal slip becomes very active. Therefore, the measured stress and strain curve under uniaxial compression

along the RD at small and large strains allows us to respectively determine the material parameters associated with the extension twinning and pyramidal slip.

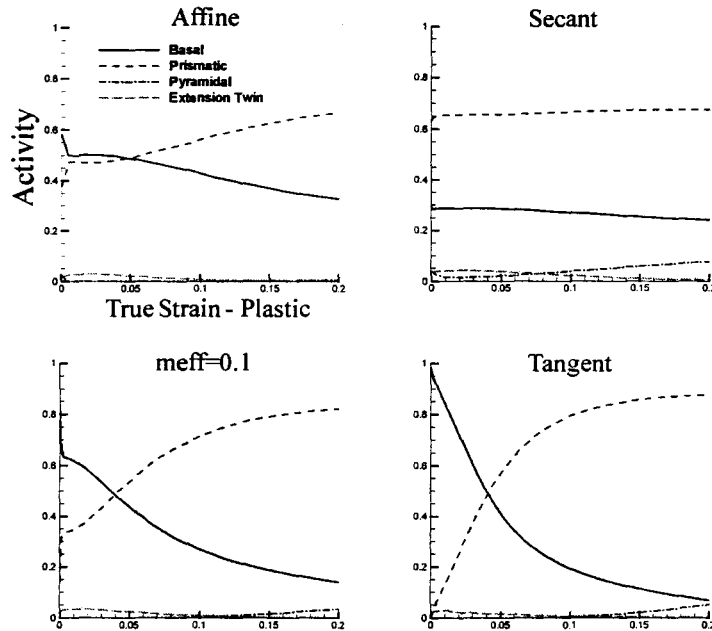


Figure 3.4 Predicted slip/twinning activities for the sheet under uniaxial tension along the RD based on various polycrystal plasticity models.

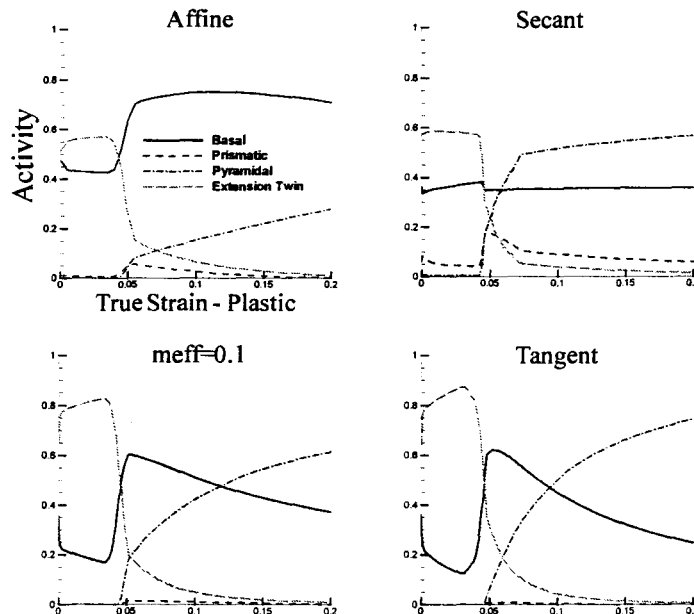


Figure 3.5 Predicted slip/twinning activities for the sheet under uniaxial compression along the RD based on various polycrystal plasticity models.

The determined values of the material constants are listed in Table 3.1. It is important to point out that the values of the material parameters for the Taylor and Secant

models are found to be the same, and the predictions of these two models are almost the same for all the deformation processes studied in the present Chapter. An assessment of the predictive capability of the VPSC model with the Secant scheme also applies to the classic Taylor model. Consequently, the results obtained for the Secant approach will be identified with those given by the Taylor model and the latter will not be presented in the present Chapter.

Figure 3.3 presents the uniaxial tension and compression stress and strain curves along the RD, respectively. It is found that all the models employed can reasonably fit the experimental curves. **Figures 3.4 and 3.5** present relative activities of slip/twinning under uniaxial tension and compression along the RD, respectively. As expected, there is negligible twinning activity under uniaxial tension (**Figure 3.4**), while twinning is very active at small strains in all the models under uniaxial compression (**Figure 3.5**). All models predict that, under uniaxial tension along the RD, mostly Basal and Prismatic slip accommodate the plastic deformation. Little or no Pyramidal slip or extension twinning activity is predicted by any model. Under uniaxial compression along the RD and at strains $|\epsilon| < 0.04$, extension twinning is very active, most grains reorient their c -axis along the RD, and the remaining plasticity is accommodated by Basal slip. When the extension twinning activity is dramatically reduced, at a strain $\epsilon \approx -0.04$, the Basal slip activity significantly increases in Affine, the Tangent and $m^{eff}=0.1$ models, while it slightly decreases in Secant model. For strains $|\epsilon| > 0.04$ all the models predict increasing Pyramidal slip activity and little to no Prismatic slip. Both observations are a consequence of the previous twinning activity, which reorients the grains for tension along the c -axis. **Figure 3.6** shows the predicted deformation textures under uniaxial compression along the RD at strain $\epsilon = -0.11$. Since texture evolution is dominated by twinning reorientation, the deformation textures given by the various models are very close and are similar to the deformed texture measured experimentally (Jain and Agnew, 2007).

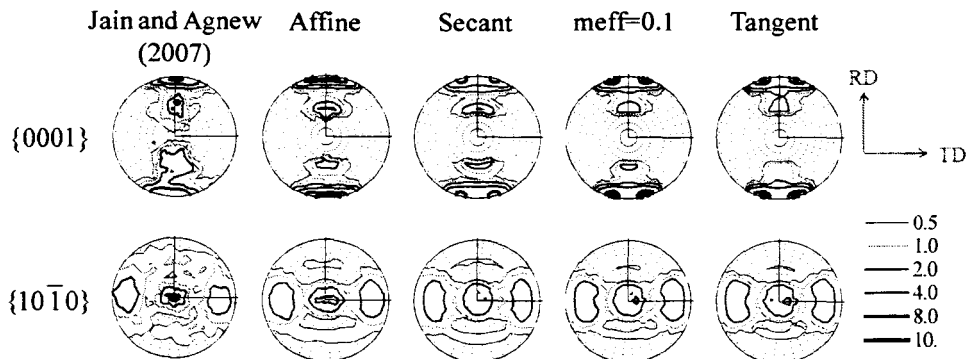


Figure 3.6 Deformed textures under uniaxial compression along the RD at strain of -0.11.

We proceed by numerically predicting the behavior of the sheet under uniaxial tension and compression (**Figure 3.7**) along the TD, using the models and the

corresponding values of material parameters determined above. It is clear that all the models numerically reproduce, with reasonable accuracy, the experimental stress and strain curves along the TD. **Figure 3.8** shows the predicted deformation textures under uniaxial compression along the TD at strain $\varepsilon = -0.11$. It is again found that the deformation textures predicted by the various models are all similar to the measured textures (Jain and Agnew, 2007).

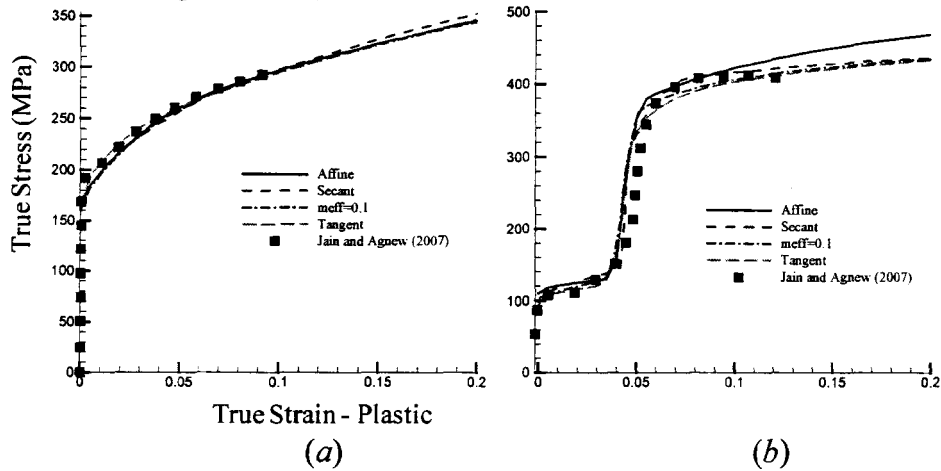


Figure 3.7 Stress and strain curves under (a) uniaxial tension, and (b) uniaxial compression along the TD.

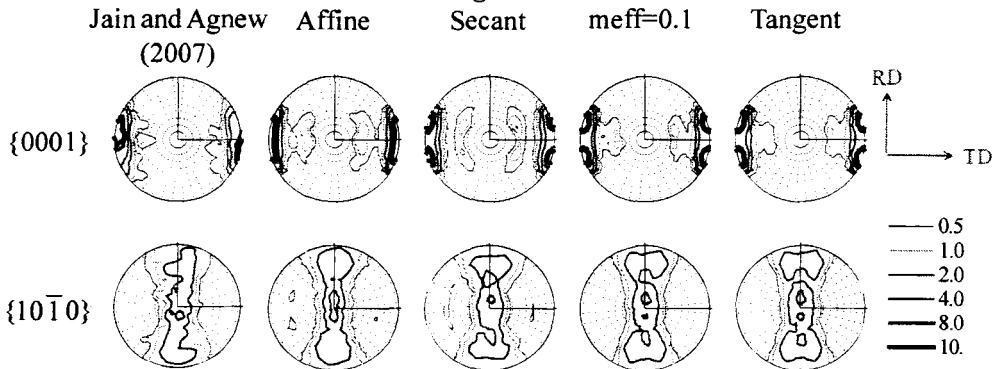


Figure 3.8 Deformed textures under uniaxial compression along the TD at strain $\varepsilon = -0.11$.

Figure 3.9 presents the predicted and measured stress and strain curves under uniaxial compression along the ND. This comparison is an independent test of the model parameters. It is found that the Affine and Secant models give close agreement with the experimental curve at strains $|\varepsilon| < 0.05$. At large strains, the Affine shows a non-zero hardening rate and overestimates the flow stress. The Tangent and $m^{eff}=0.1$ models remarkably underestimate the flow stress when $|\varepsilon| < 0.05$ and slightly overestimate the hardening at large strains. Although the stress and strain curves based on various models are quite different, the predicted textures, not shown here, are found to be very similar

because twinning is not active and little texture evolution takes place at these strains. The differences in the predicted stress responses between various models (Figure 3.9) result from the different slip activities in these models. Figure 3.10 presents relative activities of slip/twinning under uniaxial compression along the ND. It is seen that the predicted activities in Prismatic slip and extension twinning are low or zero for all the models throughout the deformation process. The Basal and Pyramidal activities, however, differ substantially from model to model: while Basal slip is the most important contributor (65-80%) in the Affine, Pyramidal slip dominates and contributes about 60% of the plastic deformation in the Secant. The predicted slip/twinning activities in the Tangent and $m^{eff}=0.1$ models are quite similar, but different from Secant and Affine: Basal slip dominates when deformation is small and Pyramidal slip is the most active slip system at large strain. The prevalence of Basal slip at small strains results in the very low flow stresses predicted by the Tangent and $m^{eff}=0.1$ models at small strains.

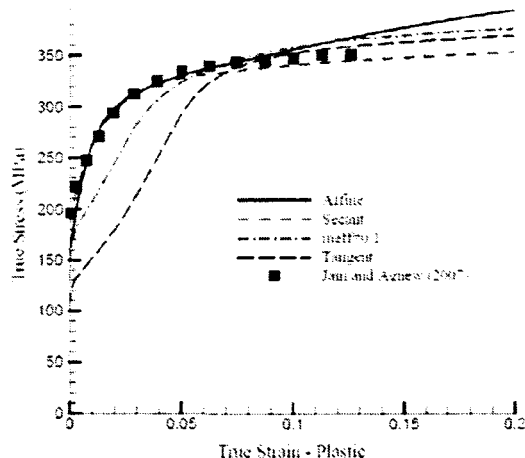


Figure 3.9 Stress and strain curves under uniaxial compression along the ND.

In the sheet metal forming industry, the so-called R value, defined as transverse-to-thickness plastic strain-ratio under uniaxial tension within the sheet plane, is often used to characterize the anisotropy of the sheet. The measured R values are often used to calculate material parameters involved in anisotropic yield functions (Wu et al., 2003; Barlat et al., 2007; Plunkett et al., 2008). Here, the prediction of R values will provide an independent test of the validity of each model. Figure 3.11 shows the predicted and measured in-plane R value vs. angle with respect to the RD, for uniaxial tension at strain $\varepsilon = 0.11$. It is important to point out that the results in Figure 3.11a and Figure 3.11b are the same but plotted in different scales. It is observed that the Secant model (also the Taylor model) grossly overestimates the R values (Figure 3.11a). The results based on the Affine and $m^{eff}=0.1$ models are in good agreement with the experimental data, while the Tangent model underestimates R slightly (Figure 3.11b). As mentioned previously, the measured R values are often used to calculate material parameters involved in anisotropic

yield functions. These anisotropic yield functions are such that R is often assumed to be constant with strain. This assumption, although not necessary, is reasonable in the yield functions designed for FCC and BCC polycrystalline sheets because variations in R values with applied deformation are relatively small (Barlat et al., 2007). However, for HCP materials, such as the magnesium alloy AZ31B sheet studied in the present Chapter, the predicted R value evolves significantly with straining, as shown in **Figure 3.12** for the sheet under uniaxial tension along the TD. It is very important to point out that the variation in R value with imposed extension straining shown in **Figure 3.12** is confirmed by the experimental works on magnesium alloys at room temperature (Avery et al., 1965; Kaiser et al., 2003; Agnew and Duygulu, 2005; Hartig et al., 2005; Lou et al., 2007; Del Valle and Ruano, 2009). One may argue that significant change in R value with deformation is mainly due to texture evolution. However, even when texture evolution is excluded in the numerical simulations, the predicted R value still noticeably evolves with deformation, except in the simulation based on Affine model, where a constant R value ($R \approx 3.6$) is calculated. In short, **Figure 3.12** clearly indicates that the assumption of constant in-plane R value under uniaxial tension for determining material constants in anisotropic yield functions for HCP polycrystalline sheets is not appropriate. One may then ask a question: is it appropriate to use the in-plane R value under uniaxial compression for developing anisotropic yield functions for HCP polycrystalline sheets?

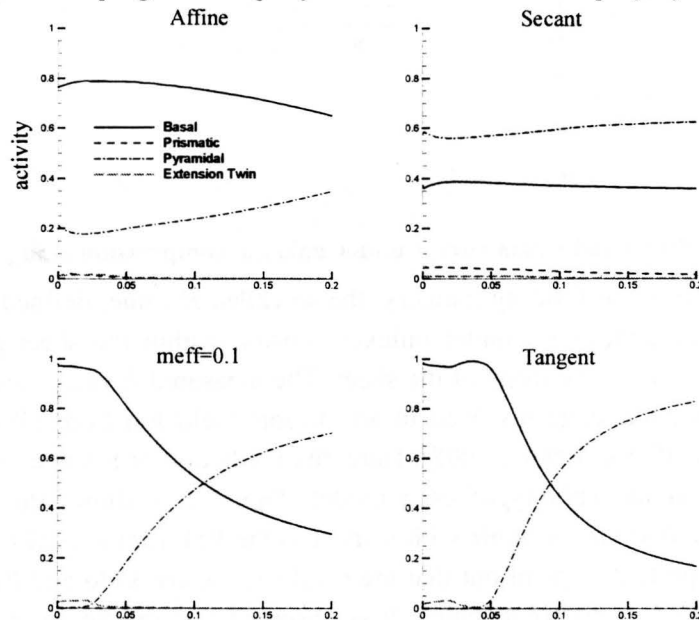


Figure 3.10 Predicted slip/twinning activities for the sheet under uniaxial compression along the ND based on various polycrystal plasticity models.

Figure 3.13 plots the predicted R value vs. true plastic strain, based on the Affine model, under uniaxial compression along 0° , 45° and 90° with respect to the RD. It is found that the predicted R values at small strain is negative. For isotropic materials and

anisotropic FCC and BCC sheet metals under uniaxial compression, the width strain ε_w and thickness strain ε_t are both tensile. However, in the AZ31B sheet under uniaxial compression, the Affine model predicts $\varepsilon_w < 0$ and $\varepsilon_t > 0$ at small strains when the extension twinning occurs (see Figure 3.8). At large strains, the predicted R value becomes positive because the width strain ε_w and thickness strain ε_t are both tensile. The other models predicted R value trends similar to those shown in Figure 3.13. It should be pointed out that the predicted negative R at small strain shown in Figure 3.13 is not an artifact of rigid, viscoplastic formulation of the VPSC model. The calculated R values predicted by the EVPSC model (when elasticity is accounted for) with the Affine self-consistent scheme are very close to the ones shown in Figure 3.13 even at very small plastic strains. The predicted and measured R values under uniaxial compression within the sheet plane are presented in Figure 3.14. It is seen that the $m^{eff}=0.1$ and Tangent models give the best prediction, the Affine reasonably reproduces the experimental data, and the Secant model underestimates the experimental R value under uniaxial compression along the TD.

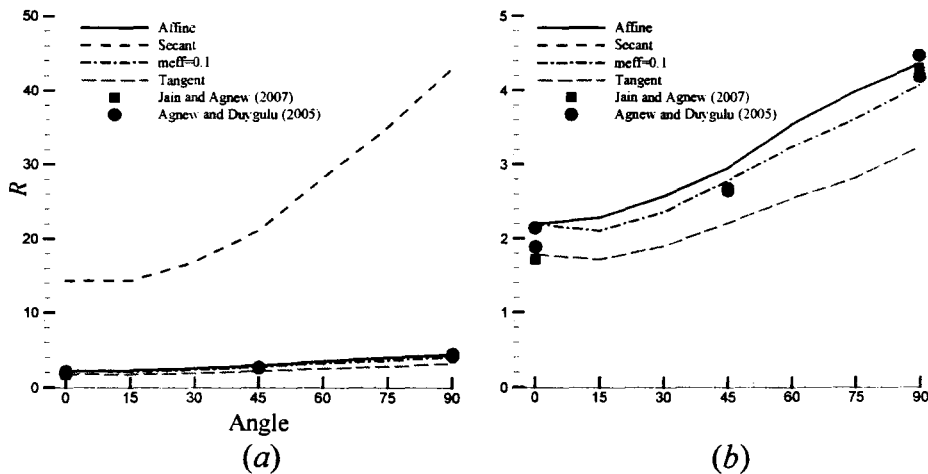


Figure 3.11 R values under uniaxial tension within the sheet plane. Same results are plotted in different scales in (a) and (b).

Under uniaxial compression along the ND, the R value is defined as the ratio of plastic strain in the RD to the plastic strain in the TD (Jain and Agnew, 2007). Figure 3.15 shows the predicted R values based on the models and their comparison with the corresponding experimental R . It is found Figure 3.15 R values under uniaxial compression along the ND that the predicted R values are below, but relatively close to, the experimental R value. Detailed observation indicates that the Affine, $m^{eff}=0.1$ and Tangent models give better agreement than the Secant.

We recall that Secant model predicts extremely high R values under uniaxial tension within the sheet plane (Figures 3.11a and 3.12). Our numerical testing indicates

that the predicted in-plane R value under uniaxial tension monotonically decreases with increasing CRSS ratio of Prismatic slip to Basal slip (Agnew and Duygulu, 2005), and monotonically increases with increasing CRSS ratio of Pyramidal slip to Prismatic slip. Based on these observations, we tried adjusting the values of the material parameters in Secant model to model the measured R values and the uniaxial tensile stress curve along RD. However, we found that there was no combination of parameters for which the Secant model could simultaneously predict reasonably the R values and measured stress-strain curves along the TD and ND. We also recall that the Tangent and $m^{eff}=0.1$ models significantly underestimate the measured flow stress at small strains under uniaxial compression along ND (Figure 3.9). We adjusted the material parameters in these models and found that, while the prediction of uniaxial compression along ND was truly improved, the predictions of other strain paths worsened. It seems that values of the material parameters, determined by fitting uniaxial tension and compression stress curves along the RD and listed in Table 3.1, give the best overall performance for each individual model.

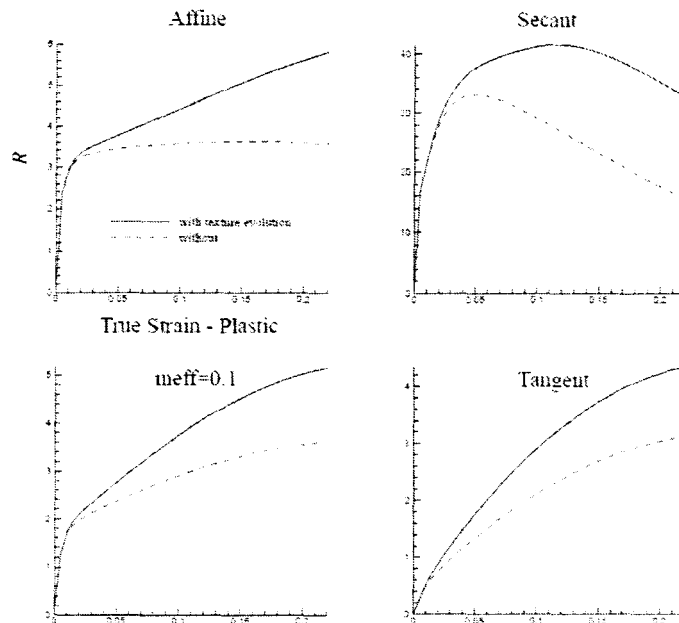


Figure 3.12 Predicted R value vs. true plastic strain curves under uniaxial tension along the TD based on various polycrystal plasticity models.

Based on the numerical results, it can be concluded that among the examined models, those with interaction stiffness halfway between the Secant (stiff) and Tangent (compliant) give the best results. In particular, no model gives a better overall performance than the Affine self-consistent. The fact that the Affine gives a good overall performance is a promising indication, because the Affine model requires no artificial “tuning” like the m^{eff} , but is based on a formal Tangent linearization of the response of

grains and medium, as opposed to making the Tangent modulus proportional to the Secant modulus as suggested by Hutchinson (1976).

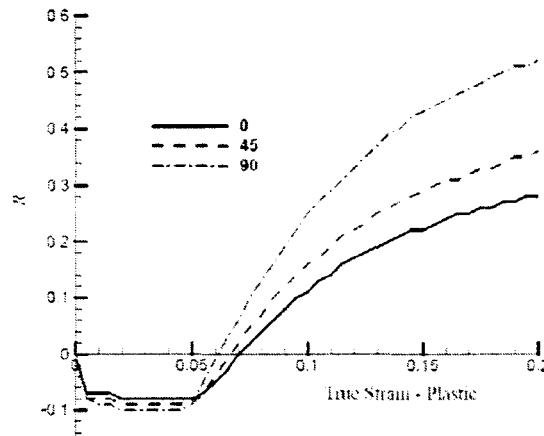


Figure 3.13 Predicted R value vs. true plastic strain curves under uniaxial compression within the sheet plane based on Affine model.

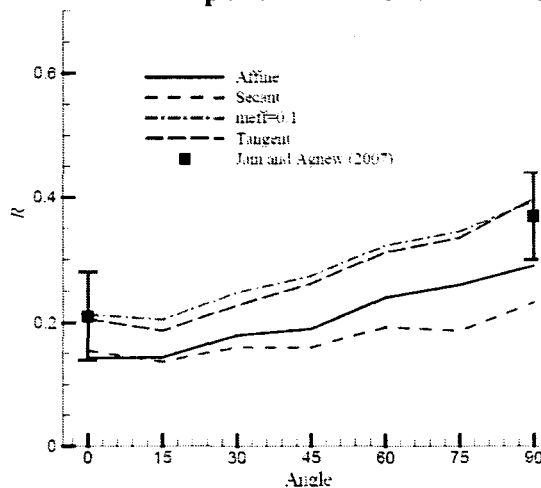


Figure 3.14 R values under uniaxial compression within the sheet plane.

The advantage of the Affine scheme over the m^{eff} is further demonstrated in Figure 3.16. In this figure, the dependence of the critical resolved shear stress (CRSS) ratios of non-Basal, namely Prismatic slip and Pyramidal slip to Basal slip are depicted for different m^{eff} values. The grain-matrix interaction stiffness (see Eq. 3.15) is adjusted within the range $m^{eff}=0.002-0.5$, which includes the compliant Tangent approximation $m^{eff}=0.05$ and approaches the stiff Secant approximation, $m^{eff}=1$. For this final aspect of the study, the slip system hardening parameters which give the best overall fits to the slip-dominated cases (uniaxial tension along RD and TD and uniaxial compression along ND) are determined. The cases involving significant twinning (e.g., in-plane compression) were avoided in order to simply characterize the impact of grain interaction stiffness on the slip system fit parameters. As the m^{eff} scheme is tuned to a stiffer grain-matrix

interaction, i.e. as the m^{eff} value goes up, the non-Basal to Basal CRSS ratios necessary to obtain a good fit to the experimental results also increases. Interestingly, the best overall fits to the experimental data were obtained for the meff scheme when $0.1 < m^{eff} \leq 0.2$, and the CRSS ratios obtained within this range of m^{eff} values are very similar to those obtained via the Affine scheme.

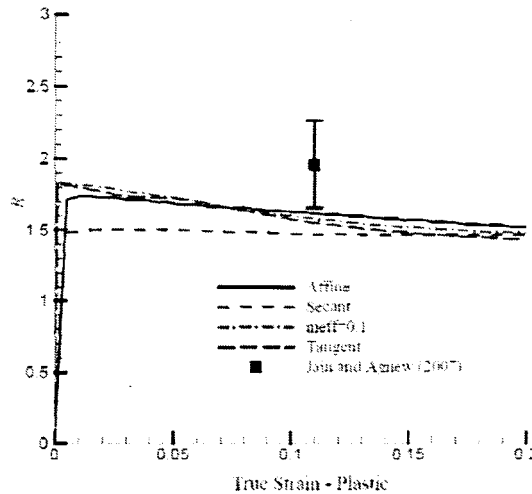


Figure 3.15 R values under uniaxial compression along the ND.

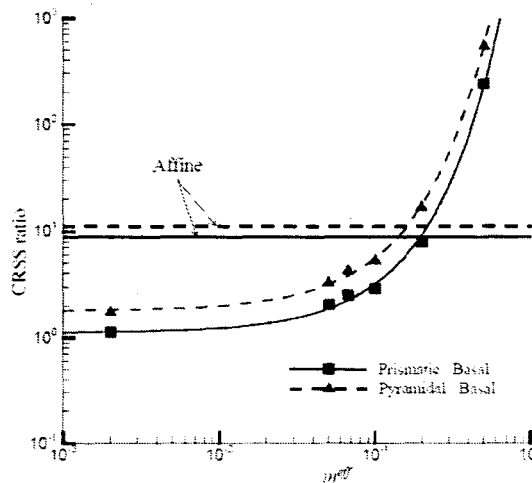


Figure 3.16 Dependence of the fitted critical resolved shear stress (CRSS) ratios of Prismatic and Pyramidal slips to Basal slip on the grain interaction stiffness (different m^{eff} values). CRSS values determined from fits to experimental stress-strain curves and R values of slip-dominated strain paths. Corresponding ratios for Affine self-consistent scheme also depicted.

Finally, we would like to underscore the previously observed fact that the relative strengths of slip systems determined from polycrystal simulations of magnesium alloys have been found to be at odds with historical single crystal magnesium results (Koike and Ohyama, 2005). As an example, the non-basal to basal CRSS ratios obtained in the present study for the initial CRSS's associated with the Affine linearization schemes are

in the range of 8 to 12. This range of ratios is higher than those of many recently published reports, which emphasizes the importance of the interaction stiffness in such studies. Nevertheless, it is still much lower than those empirically measured on pure Mg single crystals (Sheely and Nash, 1960; Yoshinaga and Horiuchi, 1964; Akhtar and Teghtsoonian, 1969a; b; Obara et al., 1973). We attribute such difference to the fact that a single crystal deforms mainly by single slip, dislocations have to overcome only the Peierls stress, and they can exit through the free surface of the crystal. For a grain within the bulk of an aggregate, on the other hand, dislocations are arrested at grain boundaries, which induce reaction stresses, cross slip, a rapid increase of the dislocation population and a rapid hardening rate.

3.4 Conclusions

In this study, various self-consistent polycrystal plasticity models have been evaluated by studying large strain behavior of magnesium alloy AZ31B sheet under different deformation processes. In all the polycrystal plasticity models considered, both slip and twinning contribute to plastic deformations. The material parameters for the various models were first fitted to experimental uniaxial tension and compression curves along the RD and then used to predict uniaxial tension and compression along the TD and uniaxial compression in the ND. An assessment of the predictive capability of the polycrystal plasticity models has been made based on comparisons of the predicted and experimental stress responses and R values. It is interesting to point out that the estimated values of the material parameters for the classical Taylor and Secant models were found to be the same, and the predictions of these two models were almost the same for all the deformation processes studied in the present Chapter. An assessment of the predictive capability of the VPSC model with the Secant scheme also applied to the classic Taylor model. It has been demonstrated that, among the models examined, the VPSC model with the Affine self-consistent model gives the best overall performance and requires no artificial tuning as does the meff scheme.

Our numerical results have clearly indicated that the R values under uniaxial tension and compression within the sheet plane evolve remarkably with imposed strain. This suggests that using R values measured at a given strain to determine anisotropic constants in anisotropic yield functions for HCP polycrystals is not appropriate for other strains.

It is important to point out that the main purpose of the present Chapter is to evaluate various homogenization assumptions for predicting the mechanical behavior of polycrystalline materials from the responses of their single crystals, while the basic descriptions of plastic deformation of the single crystals are the same for all the models. More specifically, the slip/twinning hardening is described by (3.6) and (3.7) and twinning is characterized by the PTR model. The evaluation made in the present Chapter depends

on the single crystal plasticity linearization employed. More advanced slip and twinning models have been developed (Kalidindi, 1998; 2001; Staroselsky and Anand, 2003; Wu et al., 2007b; Beyerlein and Tomé, 2008; Proust et al., 2009). An assessment of the validity of the various homogenization methods by comparison with local field calculations done by Fast Fourier Transform technique have been reported by Lebensohn et al. (2007). The authors conclude that a linearization based on accounting for (first order) stress fluctuations inside the grains provides a good match with the results of a full-field calculation, especially when the plastic anisotropy of the grains is large [see Fig. 2 in Lebensohn et al. (2007)].

It is important to mention that self-consistent polycrystal plasticity models consider the interaction between a given grain and a "homogenized matrix" representing the rest of the materials, but they do not take into account the specific interaction between an individual grain and its neighboring grains, or inhomogeneous deformation within the grain itself. When the phenomenon to be studied depends on the local characteristics and heterogeneity of such interaction (stress-strain response, Lankford coefficient and texture evolution are not particularly sensitive to local effects), then Crystal Plasticity Finite Element Models (CPFEM) may be required. In CPFEM simulations, an element of the finite element mesh represents either a single crystal or a part of a single crystal, and the constitutive response at an integration point is described by the single crystal constitutive model. This approach enforces both equilibrium and compatibility throughout the polycrystalline aggregate in the weak finite element sense (Anand and Kalidindi, 1994; Wu et al., 2004b). Furthermore, this approach facilitates taking into account grain morphology and modeling of inhomogeneous deformations at the crystal level (Wu et al., 2006; Wu et al., 2007a; Shi et al., 2010).

Chapter 4. Study of lattice strains in magnesium alloy AZ31 based on EVPSC model

Abstract — The recently developed large strain elastic visco-plastic self-consistent (EVPSC) model, which incorporates both slip and twinning deformation mechanisms, is used to study the lattice strain evolution in extruded magnesium alloy AZ31 under uniaxial tension and compression. The results are compared against in-situ neutron diffraction measurements done on the same alloy. For the first time, the effects of stress relaxation and strain creep on lattice strain measurements in respectively displacement controlled and load controlled in-situ tests are numerically assessed. It is found that the stress relaxation has a significant effect on the lattice strain measurements. It is also observed that although the creep does not significantly affect the trend of the lattice strain evolution, a better agreement with the experiments is found if creep is included in the simulations.

4.1 Introduction

It has been generally accepted that the evolution of the elastic lattice strains during loading in different grain orientations can be used as a very sensitive indicator of plastic deformation mechanisms at microscopic levels (Xu et al., 2008). Therefore, plastic deformation mechanisms can be studied by analyzing elastic lattice strain data, in addition to macroscopic stress-strain curves and texture evolutions. However, the measured lattice strains only provide crystallographic plane separations and are difficult to interpret in terms of tensorial strain and stress states. Elasto-plastic crystal models are required to understand the experimental results, especially so in the case of low symmetry materials (Brown et al., 2005).

Diffraction methods employing either neutrons or X-rays are widely used to determine lattice strains by measuring lattice spacing. The use of neutron diffraction-based internal strain measurements is a relatively new technique; early development was reported by MacEwen et al. (1983). The advantage of using neutrons over conventional X-rays is that the neutrons can penetrate deeply into a metal volume and diffract off particular sets of grains, thereby facilitating lattice-distortion measurements in those grains throughout the volume of a metal specimen. The measurements give data pertaining to the lattice strains of families of crystals having one common crystallographic direction. The distinct disadvantage of neutrons, however, is the long collection times. In a typical in-situ neutron diffraction experiment, the sample is deformed incrementally, stopping at each point to collect neutrons. The holding times typically vary between 5 and 20 minutes, depending on the material tested and on the peak-definition required (Agnew et al., 2006a; Muransky et al., 2008; Neil et al., 2010). As a consequence, during the measurement it takes place a well documented stress

relaxation in the case of a “displacement controlled” experiment, or creep in the case of a “load controlled” experiment.

Self-consistent polycrystal models have been widely used to interpret experimentally measured lattice strain data. Within this modeling paradigm, the precise surroundings of each grain are not accounted for. This apparent limitation, however, is not so significant in using neutron diffraction to measure *in-situ* internal strains in aggregates. The reason is that this technique measures average lattice spacing, coming from many grains with a common plane normal, but each experiencing different surroundings. As a result, the assumption of effective medium surrounding each grain ellipsoid has the same level of detail as the measurement, and makes these polycrystal models well suited to interpret the measurements provided by neutron diffraction. The visco-plastic self-consistent (VPSC), developed by Molinari et al. (1987) and Lebensohn and Tomé (1993), is a very popular self-consistent polycrystal model that has been successfully applied to simulate large strain behavior and texture evolution of hexagonal close-packed (HCP) polycrystalline Mg under various deformation modes (Agnew et al., 2001; Agnew and Duygulu, 2005; Jain and Agnew, 2007; Proust et al., 2009). However, viscoplastic models, such as VPSC, do not include elastic deformation and thus cannot be used to study lattice strains. Most of the experimentally measured lattice strain data have been interpreted by using the elastic-plastic self-consistent (EPSC) model developed by Turner and Tomé (1994). The aforementioned EPSC model works only for small deformation and does not include texture evolution associated with slip or twinning reorientation. Only recently Clausen et al. (2008) extended the EPSC model by including texture development and stress relaxation due to twinning, while Neil et al. (2010) developed a large strain EPSC model to approximately account for the kinematics of large strain, rigid body rotations, texture evolution and grain shape evolution. However, the rate-insensitive character of the constitutive law upon which the EPSC is based, prevents us from addressing strain rate-sensitivity in general, and the experimentally observed stress relaxation and creep associated with finite hold times for data acquisition in particular. It is expected that such a macroscopic relaxation and creep can only be accounted by a rate-sensitive elastic-plastic model. Very recently, Mareau and Daymond (2010) reported an elasto-viscoplastic self-consistent (EVPSC) model to describe the behaviour of HCP materials where multiple deformation modes, including plastic slip and twinning, coexist. The model was applied to study the development of lattice strains in a moderately textured Zircaloy-2 slab. However, the EVPSC model by Mareau and Daymond (2010) works only for small deformations, and relaxation during individual measurements was not explicitly accounted for in their simulations. However, because *in-situ* measurements may be done at large strains (Neil et al., 2010), and because neutron collection times are usually large, experimentally measured lattice strain data should be

interpreted by using a large strain EVPSC model and by explicitly accounting for effects of relaxation or creep.

The large strain EVPSC model, recently developed by Wang et al. (2010e), has been found to be able to predict many aspects of the large strain behaviour of HCP materials (Wang et al., 2010b; 2010c). In the present paper, the EVPSC model is applied to study lattice strains in magnesium alloy AZ31 under uniaxial tension and compression. The results are compared to the corresponding experimental data reported by Agnew et al. (2006a). The effects of stress relaxation and strain creep associated with finite hold times for data acquisition on the calculated lattice strains are emphasized. To the authors' knowledge, these important effects have not been investigated until now.

The plan of this paper is as follows. In Section 4.2, we explain how the average lattice strain is calculated as the relative change in average lattice spacing. Section 4.3 briefly recapitulates the EVPSC model we are going to adopt throughout this paper, mainly for the purpose of definition and notation. Section 4.4 presents results and discussions. Conclusions are presented in Section 4.5.

4.2 Lattice strains

The in-situ neutron diffraction technique measures the lattice spacing d_{hkl} of the planes (hkl) in a subset of grains that have the (hkl) plane normal parallel to the diffraction direction. The Bragg condition, namely $n\lambda = d^{hkl} \sin \theta$, relates the spacing of the diffracting plane to the beam wavelength λ and the angle θ between the beam and the plane normal, where n is an integer. The use of a 'white' beam (a continuous spectra of wavelengths), and the finite dimension of the detector (which spans about 15 deg), mean that lattice spacings within a certain range (typically $1\text{\AA} < d < 3\text{\AA}$) contribute to a given diffraction peak. As a consequence of such experimental conditions, a subset of grains with (hkl) normals contained within the solid angle of the detector, contribute to a given peak. In addition, because these grains do not experience the same stress conditions, their (hkl) spacing varies and leads to broadening of the peak. As a consequence, the diffraction peak represents a distribution of interplanar spacings d_{hkl} . Here, as in other similar papers, we are only concerned with the shift of the peak maximum with applied load, which is indicative of the average lattice strain within the corresponding subset of grains. The average lattice strain is calculated as the relative change in average plane spacing, d :

$$\langle \varepsilon^{hkl} \rangle = \frac{\langle d^{hkl} \rangle - d_0^{hkl}}{d_0^{hkl}} \quad (4.1)$$

where d_0 is the initial (stress-free) plane spacing in the single crystals. Observe that this strain is purely elastic and induced by the Cauchy stress in the subset of grains. Diffraction data are frequently plotted as a macro-stress vs. micro-strain curve, with the

applied macroscopic stress in the vertical axis and the average lattice strain $\langle \varepsilon^{hkl} \rangle$ in the horizontal axis. In the elastic regime, the lattice strain increases linearly with the macroscopic stress, and the slope is a function of directional Young modulus E^{hkl} and the bulk crystallographic texture. In the ideal case that all the grains were to yield simultaneously and continue accommodating deformation without any hardening, the stress would stop evolving in every grain, and so would the lattice strains. Such a case is implausible because of hardening and the intrinsic elastic and plastic anisotropy of crystalline grains which deform by slip and twinning. Typically, subsets of grains in ‘soft’ orientations yield first and stop bearing internal stresses, while subsets of grains in ‘hard’ orientations continue to deform elastically. Because the macroscopic stress is an average of the grain stresses, plastic relaxation in one subset of grains leads to greater load sharing in another subset. The lattice strain deviations from linearity imply that plastic deformation is taking place within grains in the subsets, and inflections in the curves can ultimately be related to activation of specific slip and twin systems.

4.3 The EVPSC model

The elastic visco-plastic self-consistent (EVPSC) model for polycrystals recently developed by Wang et al. (2010e) is a completely general elastic-visco-plastic, fully anisotropic, self-consistent polycrystal model, applicable to large strains and to any crystal symmetry. The model is based on the approximation proposed by Molinari et al (1997) for treating the elasto-visco-plastic inclusion problem. Here, we provide a brief description of the model. For details we refer to Wang et al. (2010e).

The elastic constitutive equation for a crystal is:

$$\overset{\nabla}{\sigma}^* = \mathcal{L} : \mathbf{d}^e - \sigma \text{tr}(\mathbf{d}^e) \quad (4.2)$$

where \mathcal{L} is the fourth order elastic stiffness tensor, \mathbf{d}^e is the elastic strain rate tensor and

$\overset{\nabla}{\sigma}^*$ is the Jaumann rate of the Cauchy stress σ based on the lattice spin tensor \mathbf{w}^e . The single crystal elastic anisotropy is included in \mathcal{L} through the crystal elastic constants C_{ij} (Wang and Mora, 2008). For isotropic elasticity \mathcal{L} is a function only of Young’s modulus, E , and Poisson’s ratio, ν .

Plastic deformation of a crystal is assumed to be due to crystallographic slip and twinning on systems $(\mathbf{s}^\alpha, \mathbf{n}^\alpha)$. Here, \mathbf{s}^α and \mathbf{n}^α are respectively the slip/twinning direction and normal direction of the slip/twinning system α . The following equation gives the grain (crystal) plastic strain rate \mathbf{d}^p (Asaro and Needleman, 1985):

$$\mathbf{d}^p = \sum_{\alpha} \dot{\gamma}^{\alpha} \mathbf{P}^{\alpha}, \quad \dot{\gamma}^{\alpha} = \dot{\gamma}_0 \left| \frac{\tau^{\alpha}}{\tau_{cr}^{\alpha}} \right|^{\frac{1}{m}-1} \frac{\tau^{\alpha}}{\tau_{cr}^{\alpha}} \quad (4.3)$$

where $\dot{\gamma}_0$ is a reference value for the slip/twinning rate, m is the slip/twinning rate sensitivity, and $\mathbf{P}^\alpha = (\mathbf{s}^\alpha \mathbf{n}^\alpha + \mathbf{n}^\alpha \mathbf{s}^\alpha)/2$ is the Schmid tensor for system α . $\tau^\alpha = \boldsymbol{\sigma} : \mathbf{P}^\alpha$ and τ_{cr}^α are the resolved shear stress and critical resolved shear stress (CRSS) for system α , respectively. The evolution of τ_{cr}^α due to hardening processes is given by:

$$\dot{\tau}_{cr}^\alpha = \frac{d\hat{\tau}^\alpha}{d\gamma_{ac}} \sum_{\beta} h^{\alpha\beta} \dot{\gamma}^\beta \quad (4.4)$$

where $\gamma_{ac} = \sum_{\alpha} \int |\dot{\gamma}^\alpha| dt$ is the accumulated shear strain in the grain, and $h^{\alpha\beta}$ are the latent hardening coupling coefficients, which empirically account for the obstacles on system α associated with system β . $\hat{\tau}^\alpha$ is the threshold stress, described here by an extended Voce law (Tomé et al., 1984):

$$\hat{\tau}_0^\alpha = \tau_0^\alpha + (\tau_1^\alpha + h_1^\alpha \gamma_{ac}) (1 - \exp(-\frac{h_0^\alpha}{\tau_1^\alpha} \gamma_{ac})) \quad (4.5)$$

Here, τ_0 , h_0 , h_1 and $\tau_0 + \tau_1$ are the initial CRSS, the initial hardening rate, the asymptotic hardening rate, and the back-extrapolated CRSS, respectively. The polar nature of twinning is incorporated into the model simply by specifying a very large CRSS for the reverse direction.

The response of a polycrystal comprised of many grains is obtained using a self-consistent approach: each grain is treated as an ellipsoidal inclusion embedded in a Homogeneous Effective Medium (HEM), which represents the aggregate of all the grains. Interactions between each grain and the HEM are described using the Eshelby inclusion formalism (Eshelby, 1957). During each deformation step, the single crystal constitutive rule (which describes the grain-level response) and the self-consistency criteria are solved simultaneously. This ensures that the grain-level stresses and strain rates are consistent with the boundary conditions imposed on the HEM. The behaviour of the inclusion (single crystal) and HEM (polycrystal) can be linearized as follows (Wang et al., 2010e):

$$\mathbf{d} = \mathbf{M}^e : \dot{\boldsymbol{\sigma}} + \mathbf{M}^v : \boldsymbol{\sigma} + \mathbf{d}^0 \quad (4.6)$$

$$\mathbf{D} = \bar{\mathbf{M}}^e : \dot{\boldsymbol{\Sigma}} + \bar{\mathbf{M}}^v : \boldsymbol{\Sigma} + \mathbf{D}^0 \quad (4.7)$$

Here, \mathbf{M}^e , \mathbf{M}^v , \mathbf{d} , $\boldsymbol{\sigma}$ and \mathbf{d}_0 are the elastic compliance, the viscoplastic compliance, strain rate, true stress and the back-extrapolated strain rate for the grain. $\bar{\mathbf{M}}^e$, $\bar{\mathbf{M}}^v$, \mathbf{D} , $\boldsymbol{\Sigma}$ and \mathbf{D}_0 are the corresponding terms for the HEM. The grain-level stress and strain rates are related self-consistently to the corresponding values for the HEM via an empirical superposition of the purely elastic and purely visco-plastic expressions (Molinari et al., 1997):

$$(\mathbf{d} - \mathbf{D}) = -\tilde{\mathbf{M}}^e : (\dot{\boldsymbol{\sigma}} - \dot{\boldsymbol{\Sigma}}) - \tilde{\mathbf{M}}^v : (\boldsymbol{\sigma} - \boldsymbol{\Sigma}) \quad (4.8)$$

The interaction tensors $\tilde{\mathbf{M}}^e$ and $\tilde{\mathbf{M}}^v$ are given by:

$$\tilde{\mathbf{M}}^e = (\mathbf{I} - \mathbf{S}^e)^{-1} : \mathbf{S}^e : \bar{\mathbf{M}}^e, \quad \tilde{\mathbf{M}}^v = (\mathbf{I} - \mathbf{S}^v)^{-1} : \mathbf{S}^v : \bar{\mathbf{M}}^v \quad (4.9)$$

where \mathbf{S}^e and \mathbf{S}^v are the elastic and visco-plastic Eshelby tensors for a given grain, respectively, and \mathbf{I} is the identity tensor.

Various linearization/self-consistent schemes have been proposed (Lebensohn et al., 2004). Very recently, Wang et al. (2010a; 2010d) evaluated these self-consistent approaches by applying them to the large strain behaviour of magnesium alloy AZ31B sheet under different deformation processes. It was found that the Affine self-consistent scheme gave the best overall performance among the self-consistent approaches examined. Therefore, the Affine self-consistent scheme is employed in the present study. The single crystal constitutive law is:

$$\mathbf{M}^v = \frac{\dot{\gamma}_0}{m} \sum_{\alpha} \left(\frac{\tau^{\alpha}}{\tau_{cr}^{\alpha}} \right)^{\frac{1}{m}-1} \frac{\mathbf{P}^{\alpha} \mathbf{P}^{\alpha}}{\tau_{cr}^{\alpha}} \quad (4.10)$$

$$\mathbf{d}_0 = \left(1 - \frac{1}{m}\right) \mathbf{d}^p$$

To model twinning, the Predominant Twin Reorientation (PTR) scheme proposed by Tomé et al. (1991) is used. PTR prevents grain reorientation by twinning until a threshold volume fraction A^{th1} is accumulated in any given system and rapidly raises the threshold to a value around $A^{th1} + A^{th2}$.

4.4 Results and discussions

The material considered in the present paper is magnesium alloy AZ31 extruded bar, which has been experimentally studied by Agnew et al. (2006a). The initial crystallographic texture of the bar is discretized to 2160 grains with independent orientations and weights. The $\{0002\}$ and $\{10\bar{1}0\}$ pole figures of the texture (**Figure 4.1**) show that the grains tend to have their basal planes oriented parallel (c -axis oriented perpendicular) to the extrusion direction (ED) of the bar. Polycrystal modeling predictions of HCP, and especially internal stress predictions, depend strongly upon the combination of deformation modes selected and their hardening evolution. Extensive recent work (Koike, 2005) has confirmed that the dominant deformation modes in polycrystalline AZ31 at room temperature are basal slip $\{0002\} \langle 11\bar{2}0 \rangle$ and tensile twinning $\{10\bar{1}2\} \langle 10\bar{1}1 \rangle$, with non-basal slip occurring in the vicinity of grain boundaries where strain incompatibilities perturb the local stress state. The importance of pyramidal $\langle c+a \rangle$ slip $\{11\bar{2}2\} \langle 11\bar{2}3 \rangle$ to accommodate deformation in the c direction of grains has been reported by Agnew and Duygulu (2005). Previous modeling works on lattice strains of AZ31 by Agnew et al. (2006a) and Muransky et al. (2008) have shown

that the simulations including prismatic slip $\{10\bar{1}0\} \langle 11\bar{2}0 \rangle$ give predictions which are more consistent with the experiments. Therefore, basal, prismatic and pyramidal slip as well as tensile twinning are selected here as the main deformation modes in AZ31.

Table 4.1 Values of the material parameters for the slip and twin systems used in the EVPSC model. The parameter h^{st} lists latent hardening effect of twinning activity upon the other deformation modes. All other latent hardening parameters in Eq. 4.4 are 1.

| Mode | τ_0 (MPa) | τ_1 (MPa) | h_0 (MPa) | h_1 (MPa) | h^{st} | A^{th1} | A^{th2} |
|--------------|----------------|----------------|-------------|-------------|----------|-----------|-----------|
| Basal | 17 | 1 | 190 | 10 | 1 | | |
| Prismatic | 85 | 10 | 750 | 10 | 1 | | |
| Pyramidal | 100 | 113 | 2000 | 0 | 0.65 | | |
| Tensile Twin | 20 | 0 | 0 | 0 | 1 | 0.5 | 0.8 |

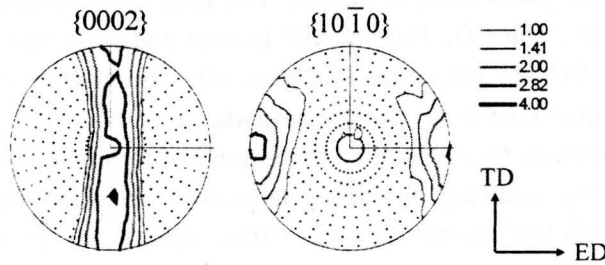


Figure 4.1 Initial texture of AZ31 bar represented in terms of the $\{0002\}$ and $\{10\bar{1}0\}$ pole distributions (Agnew et al., 2006a).

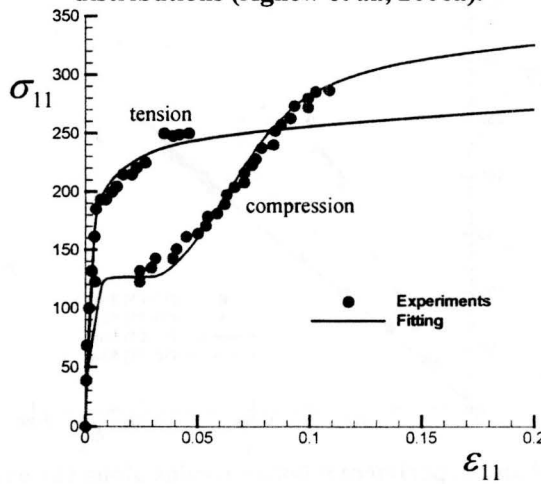


Figure 4.2 Stress-strain responses of AZ31 bar under uniaxial tension and compression along ED. The experimental data are taken from (Agnew et al., 2006a).

The reference slip/twinning rate, $\dot{\gamma}_0$, and the rate sensitivity, m , are prescribed to be the same for all slip/twinning systems: $\dot{\gamma}_0 = 0.001s^{-1}$ and $m = 0.05$, respectively, unless otherwise mentioned. The room temperature elastic constants of magnesium single

crystal reported by Simmons and Wang (1971), i.e. $C_{11} = 58.0$, $C_{12} = 25.0$, $C_{13} = 20.8$, $C_{33} = 61.2$ and $C_{44} = 16.6$ (units of GPa) are used in the simulations. The set of CRSSs and hardening parameters for each mode are estimated by fitting numerical simulations of uniaxial tension and compression along the ED to the corresponding experimental flow curves. In these simulations, a strain rate, $D_{11} = 0.001s^{-1}$, is prescribed in the loading direction, and the macroscopic stress components are enforced to be zero, except for the stress σ_{11} along the loading direction. Because of the extrusion texture, the majority of c -axes experience contraction (extension) during uniaxial tension (compression) along ED. As a consequence, twinning is not activated in axial tension, but contributes substantially to deformation during axial compression. Thus, values for the material parameters associated with the slip systems are determined from uniaxial tension along ED, while values for the material parameters associated with tensile twinning are determined from uniaxial compression along ED. The uniaxial tension and compression true stress - true strain curves along ED are presented in Figure 4.2. The characteristic S-shape of the compressive flow curve clearly reveals the importance of twinning in compression. The macroscopic yield stresses for uniaxial compression and tension are around 120 MPa and 190 MPa, respectively, showing the strong tension/compression asymmetry associated with twinning. The EVPSC model with the Affine scheme fits the experimental curves quite well. Table 4.1 lists the values of the material parameters obtained from these simulations. These parameters will be used in subsequent simulations.

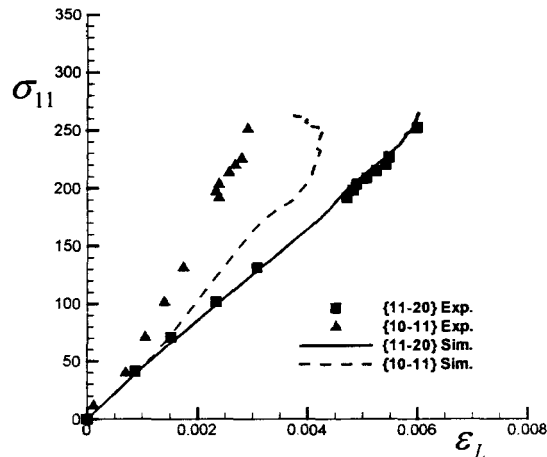


Figure 4.3 Simulated and experimental lattice strains along the axial direction under uniaxial tension.

Figure 4.3 shows the predicted and experimental internal strains along the axial direction under uniaxial tension. As reported by Agnew et al. (2006a), the non-linearity of lattice strains starts at an overall stress of around 50 MPa due to the activity of basal slip systems which have low CRSSs. Because of the texture, the $\{10\bar{1}0\}$ and $\{11\bar{2}0\}$

reflections along the loading direction are the most accurate. In Figure 4.3, only the results of $\{11\bar{2}0\}$ family are presented because the lattice strains in the $\{10\bar{1}0\}$ and $\{11\bar{2}0\}$ families are almost the same. From the comparison with the experimental data it is observed that the lattice strains of $\{11\bar{2}0\}$ family are accurately predicted by the EVPSC model, while for the $\{10\bar{1}1\}$ family the model significantly overestimates the lattice strains. Figure 4.4 shows relative activities of slip/twinning under uniaxial tension along ED. It is found that mostly basal slip and prismatic slip accommodate the plastic deformation. Little or no pyramidal slip or tensile twinning activity is predicted.

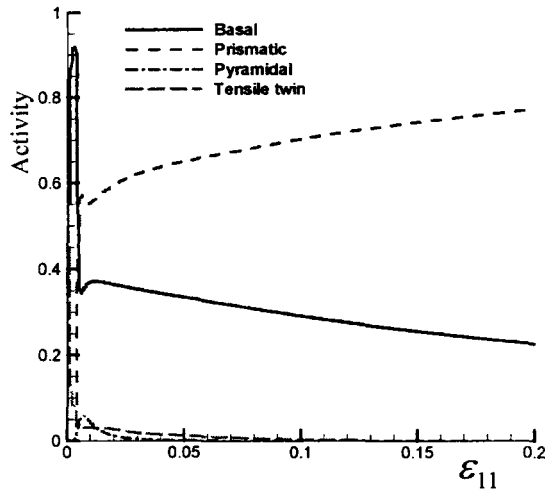


Figure 4.4 Relative activity of the various deformation modes under uniaxial tension.

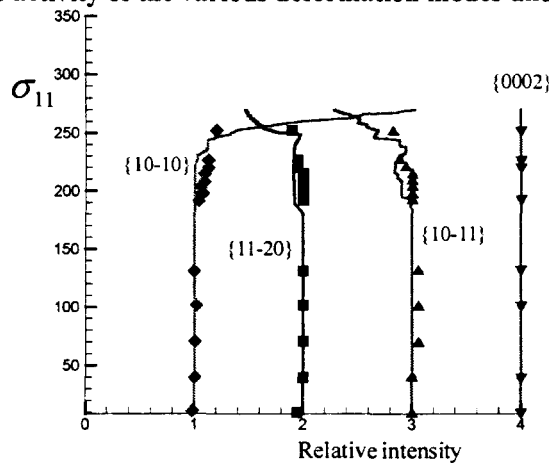


Figure 4.5 Simulated and experimental relative intensities along the axial direction under uniaxial tension. The origin is shifted by 1 unit parallel to abscissa so as to avoid congestion.

Figure 4.5 presents the relative diffraction intensities associated with various diffraction planes along the axial direction under uniaxial tension. In the simulations, the diffraction intensities are assumed to be proportional to the volume fraction of the

corresponding grain families. The absolute diffraction intensities depend on many factors including the volume fraction of grains involved, diffraction angle and texture of the sample. As a consequence, it is difficult to calculate absolute intensities for comparison with the experiment. Instead, a relative diffraction intensity, which is defined as the instantaneous intensity normalized by the corresponding initial intensity, is used here. To avoid congestion, the original relative intensities are shifted by one unit parallel to abscissa in **Figure 4.5**. It can be seen that both the experimental and simulated relative intensities remain constant before yielding ($\sigma_{11} \approx 190$ MPa). Because only very few grains have their {0002} plane along ED the intensity of the {0002} family keeps extremely small in the entire deformation process. After yielding, the intensities of the other families change due to texture evolution. However, these changes in intensity are small when the applied stress is below 250 MPa, which is the maximum stress value recorded in the tensile test. At large strains, the predicted intensity variations show a remarkable shift, which is actually due to the significant texture evolution by further straining up to 20% while the applied stress is nearly saturated.

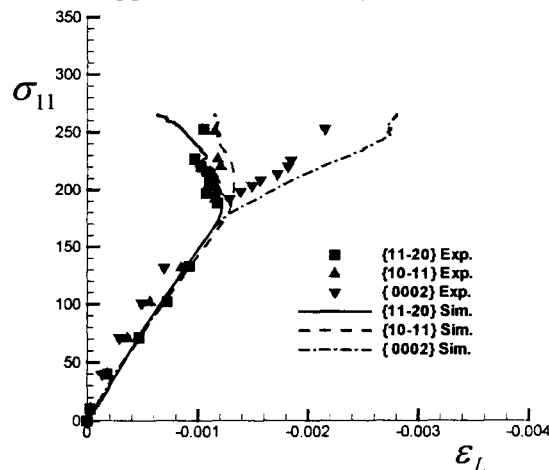


Figure 4.6 Simulated and experimental lattice strains along the transverse direction under uniaxial tension.

The lattice strains along the transverse direction under uniaxial tension are shown in **Figure 4.6**. Before yielding, the lattice strains in the {0002}, $\{11\bar{2}0\}$ and $\{10\bar{1}1\}$ families are almost the same and increase linearly with macroscopic applied stress. At $\sigma_{11} \approx 190$ MPa, a dramatic increase in the lattice strain of the {0002} family and a significant decrease in the lattice strain of the $\{11\bar{2}0\}$ and $\{10\bar{1}1\}$ families are observed in comparison to their initial linear slopes. This indicates that the grains of the {0002} family bear more stresses, while the grains of the $\{11\bar{2}0\}$ and $\{10\bar{1}1\}$ families bear relatively less stress. The reason for this can be found from **Figure 4.4**, which shows large prismatic activity and little pyramidal and twinning activity. The former system

accommodates deformation perpendicular to the c -axis, and the latter systems accommodate deformation along c -axis. If pyramidal or twinning are not active, more elastic strain accumulates along the c -axis. The predictions based on the EVPSC model are in reasonable agreement with the experimental data. The relative intensities for various families in the transverse direction under uniaxial tension are shown in **Figure 4.7** (lines for predictions and symbols for experiments). The results are consistent with the ones along the axial direction shown in **Figure 4.5** More specifically, there is practically no change in the intensity until about 190 MPa, and a small change from there to 250 MPa. Past this point, the predictions are affected by the fact that there is a dramatic increase in macroscopic strain and thus a significant texture evolution with little increase in stress because the applied stress is nearly saturated (see **Figure 4.2**).

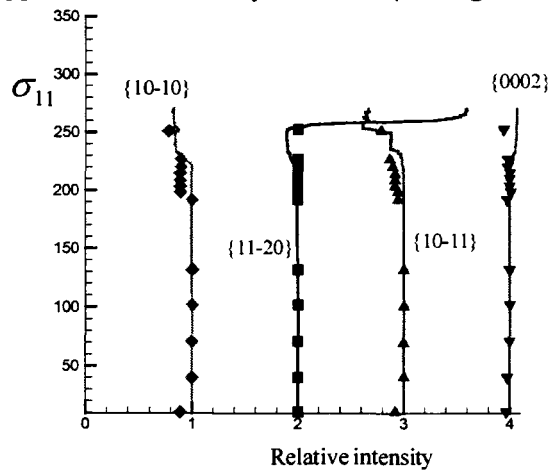


Figure 4.7 Simulated and experimental relative intensities along the transverse direction under uniaxial tension. The origin is shifted by 1 unit parallel to abscissa so as to avoid congestion.

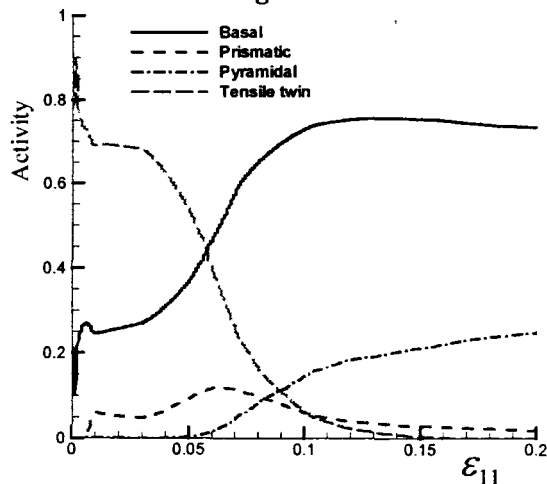


Figure 4.8 Activity of various deformation modes under uniaxial compression.

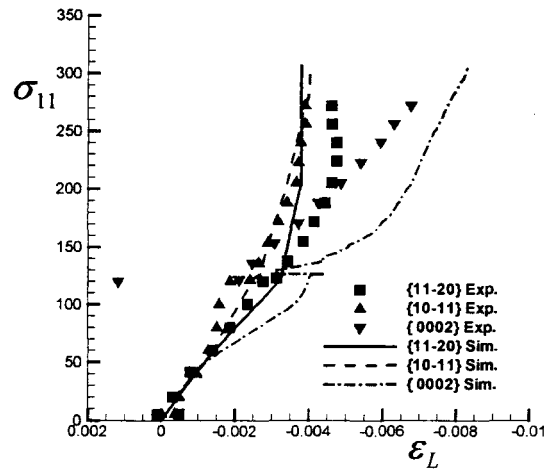


Figure 4.9 Simulated and experimental lattice strains along the axial direction under uniaxial compression.

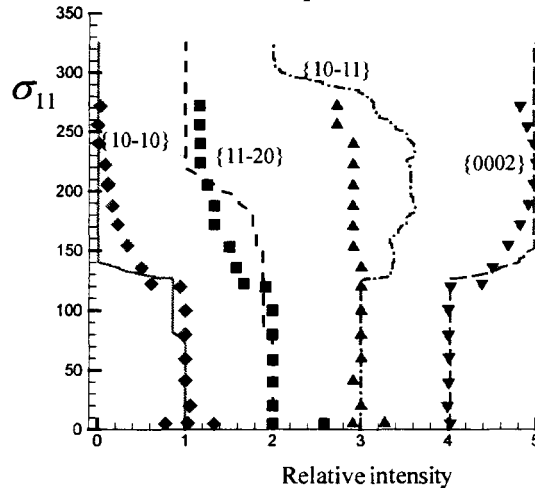


Figure 4.10 Simulated and experimental relative intensities along the axial direction under uniaxial compression. The origin is shifted by 1 unit parallel to abscissa so as to avoid congestion.

We proceed by numerically predicting the lattice strains under uniaxial compression along ED. **Figure 4.8** shows relative activities of slip/twinning under uniaxial compression. It is found that under uniaxial compression and at strains $|\varepsilon_{11}| < 0.05$, tensile twinning is very active, and the remaining plasticity is accommodated by basal slip and prismatic slip. The tensile twinning activity decreases rapidly, while the basal slip activity significantly increases in the simulation and dominates deformation past $|\varepsilon_{11}| > 0.10$. For strains $|\varepsilon_{11}| > 0.05$ the model predicts increasing pyramidal slip activity and little to no prismatic slip. Both observations are a consequence of the previous twinning activity, by which most grains reorient their c -axis along ED.

Figure 4.9 presents the lattice strains along the axial direction under uniaxial compression. The macroscopic yield stress is about 120 MPa, which coincides with the plateau in the compressive stress - strain curve where the twinning activity dominates (see **Figure 4.2** and **Figure 4.8**). At the yield point of compression, twinning reorients the $\{0002\}$ planes 'into' the detector, and an obvious stress transfer takes place. The newly formed twins are in tension and thus more compression has to be taken by the families of $\{10\bar{1}0\}$ and $\{11\bar{2}0\}$. This "shear over-relaxation" effect associated with twinning is not included in the EVPSC model, but is accounted for and discussed by Clausen et al. (2008) within a modified EPSC framework, and has been experimentally characterized by Aydiner et al. (2009) using X-ray diffraction. The conclusion by Clausen et al. (2008) and Aydiner et al. (2009) is that, when formed, the twinned domains align their c-axis with the compression direction ($\{0002\}$ family), but exhibit a tensile stress along such direction. Their stress state shifts rapidly to be compressive as more stress is applied and they grow (**Figure 4.9**). The transient lattice strain at yielding is only crudely simulated by the EVPSC because the PTR scheme reorients the whole grain when a threshold value is reached, rather than doing so gradually. However, when most of the grains have been reoriented, the lattice strain of $\{10\bar{1}1\}$ and $\{0002\}$ families predicted by the EVPSC agrees with the experimental data both qualitatively and quantitatively. For the family of $\{11\bar{2}0\}$, the EVPSC model predicts the experimental data qualitatively but underestimates the lattice strain because there is a small fraction of grains in that family due to the PTR scheme.

Figure 4.10 shows the relative diffraction intensities associated with various diffraction planes along the axial direction for the case of uniaxial compression. Because the initial intensity of the $\{0002\}$ family is extremely small, its intensity is normalized by its largest value, instead of the initial value. It is observed that the intensities predicted by the EVPSC model (lines) are in reasonably good agreement with the experimental ones (symbols). At yielding where twinning dominates, the predicted intensities change more rapidly than the experimental ones. The most significant disagreement between predications and experimental data is found from the relative diffractive intensity associated with the $\{10\bar{1}1\}$ family. While the experimental intensity slightly decreases with increasing stress, the prediction has a sudden increase at yielding and remains significantly higher than the experimental one until the stress reaches about 250 MPa. Above this stress level, the predicted intensity decreases dramatically with increasing stress.

The lattice strains along the transverse direction under uniaxial compression are presented in **Figure 4.11**. The compressive lattice strain of the $\{0002\}$ family results from the twinning activity. The EVSPC model qualitatively captures the experimental evolution of lattice strains but the trends are exaggerated. The growth of the twin

domains inside the parent grain has the effect of inducing a compressive transverse strain, which manifests itself as shifting the $\{0002\}$ planes in the parent towards the compression region, although a simplistic Poisson analysis would predict them to be in tension. The $\{10\bar{1}1\}$ family exhibits a similar behavior. **Figure 4.12** shows the relative intensities of various diffraction planes along the transverse direction under uniaxial compression. A dramatic change in the intensities at yielding is due to the twin induced reorientation. It can be seen that the EVPSC model provides a good agreement with the experimental intensities.

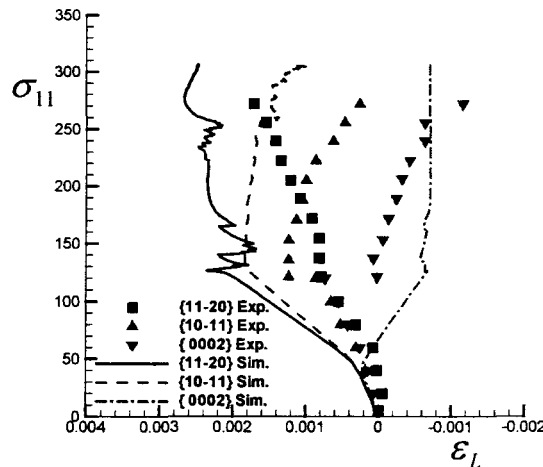


Figure 4.11 Simulated and experimental lattice strains along the transverse direction under uniaxial compression.

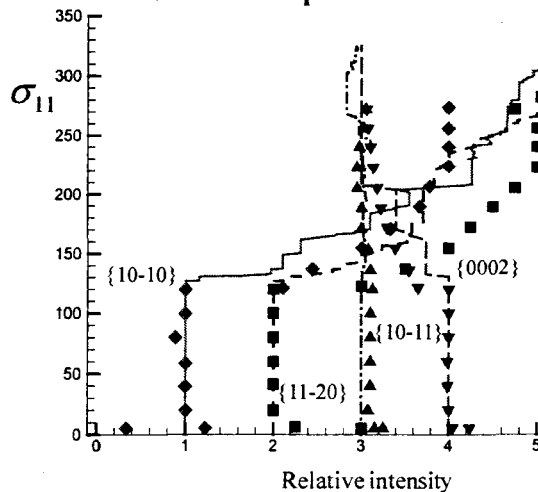


Figure 4.12 Simulated and experimental relative intensities along the transverse direction under uniaxial compression. The origin is shifted by 1 unit parallel to abscissa so as to avoid congestion.

As mentioned previously, each in-situ neutron diffraction measurement of lattice strain takes approximately 10 minutes, depending on the penetration of neutrons for the particular material. Therefore, stress relaxation in displacement controlled loading and

creep in load controlled loading are unavoidable. It is expected that the stress distribution changes little during creep and as a result, the associated lattice strains are not expected to change much in load controlled loading. However, in displacement controlled loading, the applied stress drops significantly during the period of data acquisition, and this stress relaxation will change the lattice strains. However, the effects of the stress relaxation and creep on the lattice strains have not been assessed. For the first time, in the present paper, these effects are numerically investigated using the EVPSC model.

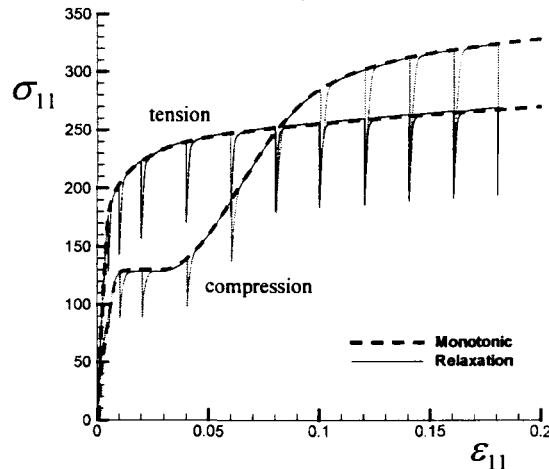


Figure 4.13 Stress and strain curves under monotonic loading and loading with relaxation.

In the calculations that follow, relaxation is simulated at each measuring point, following which the aggregate is reloaded up to the measuring point. In the simulations, the imposed macroscopic strain rate $D_{11} = 0.001s^{-1}$ is reduced to zero instantaneously at the onset of relaxation. In a simulation of monotonic uniaxial tension/compression under a constant imposed strain rate $D_{11} = 0.001s^{-1}$ it will take 120s to reach strain of 0.12. On the other hand, each in-situ neutron diffraction measurement of lattice strain takes approximately 10 minutes, which is much longer than the time required for completing a monotonic loading. Therefore, the relaxation time is prescribed to be 500s. It will become clear later that 500s are enough for lattice strains to be almost saturated. The boundary conditions for relaxation are taken as: $D_{11} = 0$, $\dot{\sigma}_j = 0$ except $\dot{\sigma}_{11} \neq 0$. To maintain the constant applied strain, due to the viscous nature of the EVPSC model, the inelastic strains during relaxation increase with time at the expense of the reduction of the elastic strains. **Figure 4.13** gives the macroscopic stress - strain curves under loading with and without relaxation. The legend “relaxation” in **Figure 4.13** and other figures shown later indicates loading with relaxation, while “Monotonic” implies loading without relaxation. It can be seen that at the relaxation point, the stress drops by about 25% for this particular relaxation time. The higher the stress, the more the stress relaxation that takes place. The same rate sensitivity ($m=0.05$) and hardening parameters (**Table 4.1**) are used for the

loading and the relaxation. Although the same set of parameters may not apply to both processes, the purpose of this paper is to investigate the qualitative effects of relaxation upon the measurements, and not to precisely characterize the creep parameters.

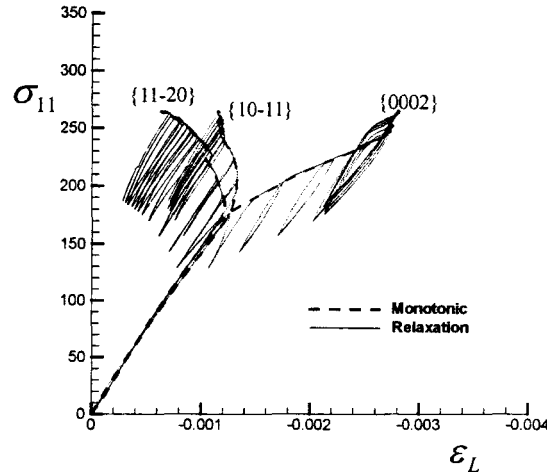


Figure 4.14 Simulated lattice strains along the transverse direction under uniaxial tension with relaxation and without relaxation (monotonic).

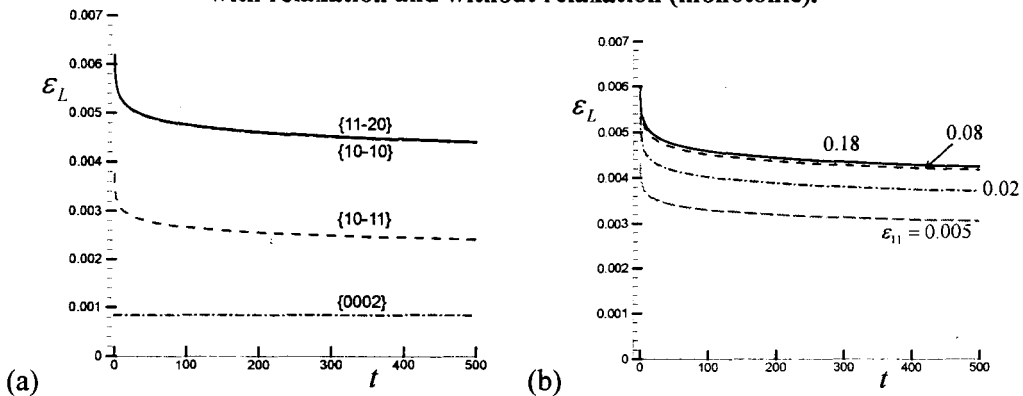


Figure 4.15 Simulated lattice strains along the axial direction under uniaxial tension with relaxation (a) at $\epsilon_{11} = 0.18$; and (b) lattice strain for the $\{11\bar{2}0\}$ diffraction plane under various strain levels.

Figure 4.14 shows the simulated lattice strains along the transverse direction under uniaxial tension with and without relaxation. Obviously, stress relaxation affects the predicted lattice strain significantly. Figure 4.15a illustrates the lattice strains along the axial direction under uniaxial tension for a single relaxation path at $\epsilon_{11} = 0.18$. The lattice strain of the $\{0002\}$ family remains unchanged because the stress is far from the threshold values in those grains, while the lattice strain of the $\{11\bar{2}0\}$ family experiences the most significant change during stress relaxation. It is found that the lattice strains drop rapidly at the early stage of the relaxation and behave asymptotically at larger times. Clearly, the lattice strains are almost constant after 200s. Figure 4.15b plots the relaxation of the

$\{11\bar{2}0\}$ poles at four different measurement points. It is observed that the higher the elastic strain - and so the closer the stress is to the flow value - the more the lattice strain is relaxed for a fixed time interval. More specifically, at 200s there is a lattice strain relaxation of 0.001, 0.0013, 0.0015 and 0.0016 at total strains of 0.005, 0.02, 0.08 and 0.18, respectively. Typically, the internal strains drop by about 25% in the first 200s.

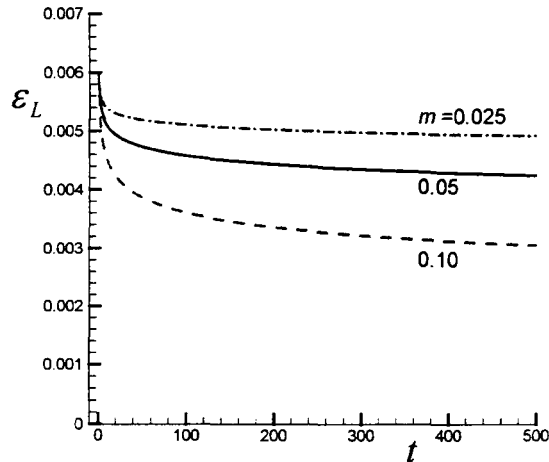


Figure 4.16 Effect of strain rate sensitivity m on the simulated lattice strains along the axial direction for the $\{11\bar{2}0\}$ diffraction plane under uniaxial tension with relaxation at $\varepsilon_{11} = 0.18$.

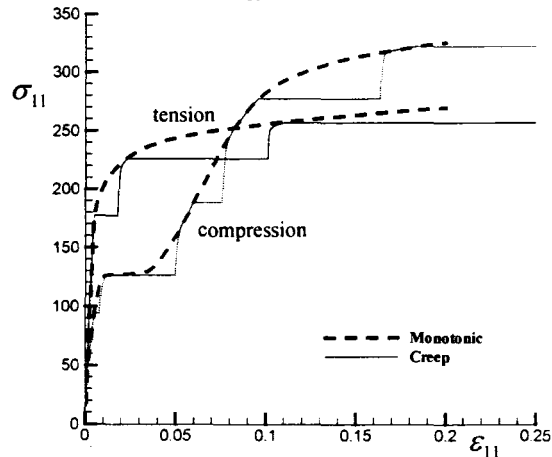


Figure 4.17 Stress and strain curves under uniaxial tension and compression with creep and without creep (monotonic).

The relaxation results shown in Figs. 4.13-4.15 depend on the ratio of the effective viscosity of the plastic behavior to the elastic modulus. While the previous simulations are based on using a strain rate sensitivity $m = 0.05$ in the EVPSC model, **Figure 4.16** shows the effect of strain rate sensitivity on the simulated lattice strains along the axial direction for the $\{11\bar{2}0\}$ family under uniaxial tension with stress relaxation at $\varepsilon_{11} = 0.18$. As expected, the amount of decrease in the lattice strain during stress relaxation increases

with increasing strain rate sensitivity. Furthermore, the higher the strain rate sensitivity, the longer the time for the lattice strain to approach its saturated value. However, even if $m = 0.10$ the evolution of the lattice strain with time becomes insignificant after 200s.

Unfortunately, the predicted effect of relaxation on lattice strains cannot be assessed experimentally since the in-situ tests carried by Agnew et al. (2006a) were performed under load control. A few displacement controlled in-situ tests were performed by Clausen et al. (2008) in the plateau region of the stress-strain curve for the case of ED compression, because in these region load control leads to a substantial amount of creep taking place. These tests were supplementary to load controlled in-situ tests in order to maintain measurement accuracy at the region where twinning dominates.

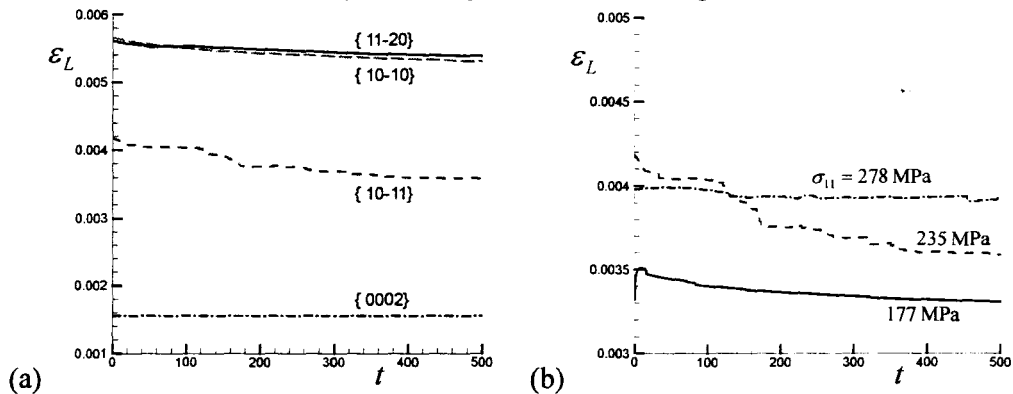


Figure 4.18 Simulated lattice strains along the axial direction under uniaxial tension with creep (a) at $\sigma_{11} = 235$ MPa; and (b) lattice strain for the $\{10\bar{1}1\}$ diffraction plane under various stress levels.

Figure 4.17 gives the macroscopic stress - strain curves under two loading conditions: either allowing for creep during holding times, or not. The legend “Creep” in Figure 4.17 indicates loading followed by creep, while “Monotonic” implies loading without allowing creep. The boundary conditions for creep are taken as: $\dot{\sigma}_{ij} = 0$, and the creep time is again prescribed to be 500s. It is observed that the magnitude of the creep strain depends on the hardening rate at the onset of creep. The higher the hardening rate, the smaller the creep strain there is. This is because creep accommodates plastic deformation without changing the resolved shear stress and, when the hardening rate is higher, the corresponding CRSS increases rapidly and therefore the accommodated strain becomes less at a given time interval according to equations (4.3) and (4.4).

Figure 4.18a shows the lattice strains along the axial direction for several diffraction planes at a creep stress of 235 MPa under uniaxial tension. It can be seen that, except for the $\{10\bar{1}1\}$ family, the axial lattice strains remain almost constant during creep. Figure 4.18b plots the evolution of the lattice strains with time for the $\{10\bar{1}1\}$ plane at three different measurement points. It is found that the reduction in the lattice strain

during creep is much more significant at $\sigma_{11} = 235$ MPa than that at $\sigma_{11} = 278$ MPa. This is due to the fact that the hardening rate at $\sigma_{11} = 235$ MPa is much higher than that at $\sigma_{11} = 278$ MPa. However, even at $\sigma_{11} = 235$ MPa the evolution of the lattice strain with time becomes insignificant after 200s.

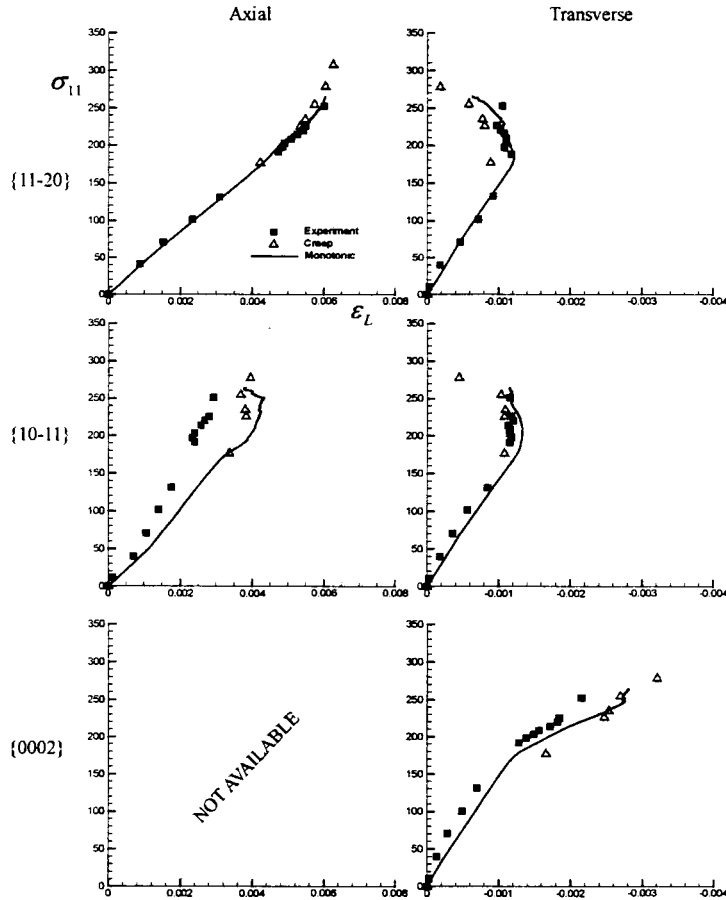


Figure 4.19 Effect of creep on the predicted lattice strains under uniaxial tension.

Figure 4.19 and Figure 4.20 show the effect of creep on the predicted lattice strains under uniaxial tension and compression, respectively. For a comparison, the results under monotonic loading (i.e. without creep) are also included in the figures. For each measurement, the lattice strains with creep are taken at a creep time of 200s. Since the lattice strains evolve very slowly after 200s (see Figure 4.18), it is found that accounting for creep does not significantly affect the trend of the lattice strain evolution. However, a more careful observation reveals that a better agreement, noticeable but not very significant, with the experiments is found if creep is included in the simulations.

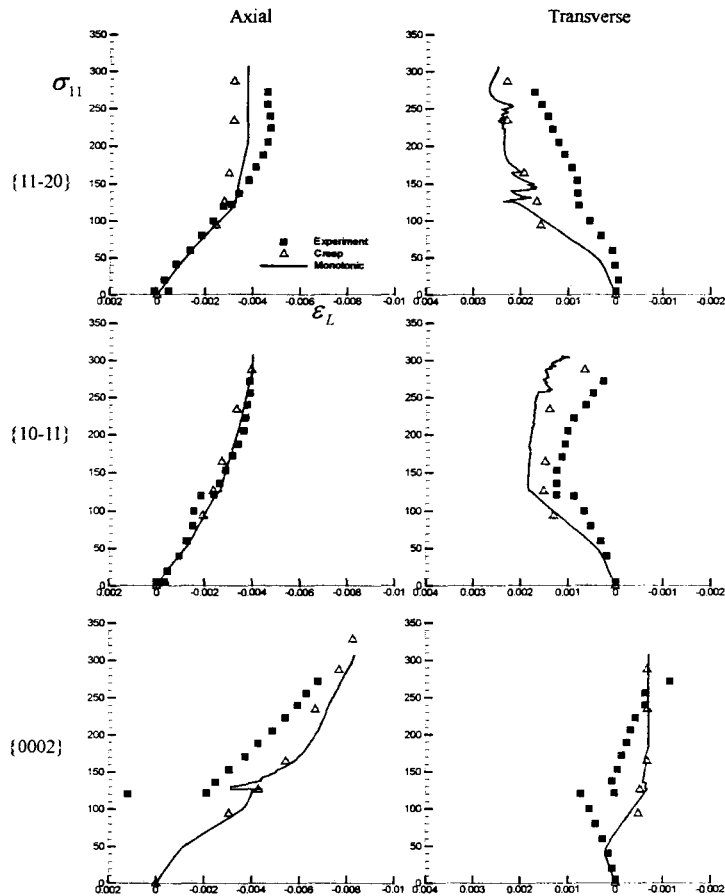


Figure 4.20 Effect of creep on the predicted lattice strains under uniaxial compression.

Comparing **Figure 4.15b** and **Figure 4.18b** and noticing the difference in scale between these figures, it is found that, for a given strain rate sensitivity ($m = 0.05$), the evolution of lattice strains during strain creep is much less important than that during stress relaxation. Though not shown here, numerical tests indicate that this observation holds for a wide range of strain rate sensitivity. Fig. 21 shows the predicted lattice strains along the axial direction for several diffraction planes under uniaxial tension with relaxation and creep at $\sigma_{11} = 235$ MPa. It is noted that, from **Figure 4.15** and **Figure 4.18**, the effects of stress relaxation and strain creep on lattice strains depend on the stress and strain at which the relaxation and creep are initiated. At the stress $\sigma_{11} = 235$ MPa and the corresponding strain $\varepsilon_{11} = 0.035$, the effect of creep on lattice strains is most significant (see **Figure 4.15** **Figure 4.18b**), although still much smaller than the effect of stress relaxation on lattice strains (see **Figure 4.15b**). Therefore, together with **Figure 4.15** and **Figure 4.18**, **Figure 4.21** confirms that creep has relatively smaller influence on lattice strain evolution than relaxation does. This implies that enforcing constant stress at each

measuring point may be a more efficient situation for comparing experiments and simulations.

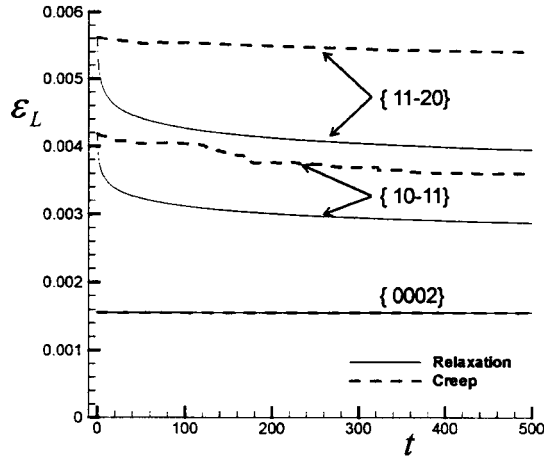


Figure 4.21 Simulated lattice strains along the axial direction under uniaxial tension with relaxation or creep at $\sigma_{11} = 235$ MPa.

4.5 Conclusions

The recently developed large strain elastic visco-plastic self-consistent (EVPSC) model, which incorporates both slip and twinning deformation mechanisms, has been used to study lattice strain evolution in conventional extruded magnesium alloy AZ31 under uniaxial tension and compression. The predictions have been compared with in-situ experimental measurements obtained using in-situ neutron diffraction. The EVPSC model can qualitatively and almost quantitatively predict the evolution of lattice strains.

For the first time, the stress relaxation and creep effects associated with in-situ neutron measurements have been modeled for strain controlled and stress controlled measuring methods, respectively. It has been found that the stress relaxation (strain control) has a more significant effect on the lattice strain measurements than the creep does. It has been also observed that although the creep does not significantly affect the trend of the lattice strain evolution, a better agreement with the experiments is found if creep is included in the simulations. Numerical results have suggested that enforcing constant stress at each measuring point may be a more efficient situation for comparing experiments and simulations.

Finally, it is worth mentioning that crystal plasticity based finite element (FE) approach has been also widely used to interpret neutron diffraction results (Dawson et al., 2001; Marin et al., 2008). In FE simulations an element of the FE mesh represents either a single crystal or a part of a single crystal, and the constitutive response at an integration point is described by the single crystal constitutive model. This approach enforces both equilibrium and compatibility throughout the polycrystalline aggregate in the weak FE sense (Anand and Kalidindi, 1994; Wu et al., 2004b). Furthermore, it facilitates

consideration of grain morphology and the modeling of deformation inhomogeneity within individual grains (Wu and Lloyd, 2004; Wu et al., 2007a). This work is in progress and will be reported elsewhere.

Chapter 5. On crystal plasticity formability analysis for magnesium alloy sheets

Abstract — Sheet metal formability is assessed in terms of the forming limit diagram (FLD) for magnesium alloys with hexagonal close packed (HCP) crystallographic structure. All simulations are based on the recently developed elastic viscoplastic self-consistent (EVPSC) model and the classical Taylor model, in conjunction with the M-K approach. The role of crystal plasticity models and the effects of basal texture on formability of magnesium alloy AZ31B sheet are studied numerically. It is observed that formability in HCP polycrystalline materials is very sensitive to the intensity of the basal texture. The path-dependency of formability is examined based on different non-proportional loading histories, which are combinations of two linear strain paths. It is found that while the FLD in strain space is very sensitive to strain path changes, the forming limit stress diagram (FLSD) in stress space is much less path-dependent. It is suggested that the FLSD is much more favourable than the FLD in representing forming limits in the numerical simulation of sheet metal forming processes. The numerical results are found to be in good qualitative agreement with experimental observations.

5.1 Introduction

The concept of the forming limit diagram (FLD) has been used to represent conditions for the onset of sheet necking (Hecker, 1975); this is now a standard tool for characterizing materials in terms of their overall forming behavior. Most theoretical and numerical FLD analyses have been based on the so-called M-K approach, developed by Marciniak and Kuczynski (1967). Within the M-K framework, the influence of various constitutive features on FLDs has been explored using phenomenological plasticity models (Neale and Chater, 1980; Wu et al., 2003) and crystal plasticity (Zhou and Neale, 1995; Wu et al., 1997; Inal et al., 2005; Signorelli et al., 2009). Using the M-K approach, the predicted FLDs based on crystal plasticity were in good agreement with measured FLDs for rolled aluminum alloy sheets (Wu et al., 1998; Knockaert et al., 2002). However, almost all the FLD analyses have been for polycrystalline sheet metals with face centered cubic (FCC) and body centered cubic (BCC) crystallographic structures. Only very recently, Neil and Agnew (2009) and Levesque et al. (2010) carried out crystal plasticity based FLD analyses for magnesium alloys with hexagonal close packed (HCP) crystallographic structure, based on respectively the visco-plastic self-consistent (VPSC) model developed by Molinari et al. (1987) and Lebensohn and Tomé (1993) and the Taylor-type model proposed by Kalidindi (1998).

In the present Chapter, an FLD analysis for magnesium alloy AZ31B sheet is carried out based on the elastic-viscoplastic self-consistent (EVPSC) model recently developed by Wang et al. (2010e) and the classical Taylor model (Taylor, 1938), in

conjunction with the M-K approach. The main purposes of this Chapter are to study (1) the effect of basal texture on formability; (2) the role of constitutive model on predicted FLDs; and (3) the path-dependency of formability.

First of all, it is well known that conventionally processed magnesium sheet exhibits very limited formability, due to the limit number of plastic deformation modes available. This can be explained based on the deformation behavior of magnesium single crystals deformed in uniaxial or biaxial tension with the basal plane parallel to the loading direction. In this case, the imposed extension is accompanied by contraction normal to the loading axis, in the direction tangential to the basal plane; very limited reduction normal to the basal plane is observed, and the crystals exhibit low ductility (Reed-Hill and Robertson, 1957b). This behaviour has strong implications for the room temperature formability of HCP magnesium wrought alloys, in which the basal planes typically lie preferentially in the plane normal to the primary compression direction imposed during processing. However, recent experimental works have revealed that formability of magnesium sheets can be significantly improved through texture optimization by mainly re-orientating basal plane. For example, Huang et al. (2008) have reported an increase in the uniform strain prior to necking in AZ31 sheet produced by differential speed rolling (DSR), where the basal poles are tilted $\sim 15^\circ$ in the rolling direction (RD). Chino et al. (2008) have observed enhanced tensile ductility of AZ31 bar through torsional extrusion (TE), where the basal poles are inclined $\sim 30^\circ$ to the extrusion direction. Mukai et al. (2001) and Agnew et al. (2004) have shown that enhanced ductility can be achieved through equal channel angular extrusion (ECAE), where the basal planes are preferentially inclined $\sim 45^\circ$ to the extrusion direction. In a recently study, Wang et al. (2010c) investigated the influence of basal texture on the uniform strain under uniaxial tension and the limit strain under in-plane plane strain tension. This preliminary study suggested that formability can be significantly improved by controlling texture even without grain refinement. The present Chapter carries out a detailed study on the effects of basal texture on FLDs.

Secondly, it is also well-known that predicted FLDs are sensitive to the constitutive modes employed (Wu et al., 2003). Motivated by the works on effects of texture on formability of aluminum alloy sheets (Kuroda and Ikawa, 2004; Wu et al., 2004a; Yoshida et al., 2007), Signorelli and Bertinetti (2009) recently investigated how the cube texture affects the formability of FCC sheet metals. It was found that the predicted FLDs based on the VPSC model are quite different to the ones based on the classical Taylor model. In the present Chapter, the role of the constitutive model on formability of HCP sheet metals is assessed by comparing the predicted FLDs based on the EVPSC model with various self-consistent schemes and the classical Taylor model.

Finally, both experimental and numerical results have indicated that FLDs from FCC and BCC sheet metals are very sensitive to strain path changes (Laukonis and

Ghosh, 1978; Graf and Hosford, 1994; Zhao et al., 1996; Hiwatashi et al., 1998; Kuroda and Tvergaard, 2000; Wu et al., 2000; Wu et al., 2005). Knowing the drawback of conventional FLDs, Arrieux et al. (1982), among others, represented formability based on the state of stress rather than the state of strain. They constructed a forming limit stress diagram (FLSD) by plotting the calculated principal stresses at necking. It was concluded that all FLSDs, based on phenomenological plasticity models such as Hill (1948) and Hosford (1979) and crystal plasticity theory (Asaro and Needleman, 1985), were almost path-independent (Arrieux, 1995; Zhao et al., 1996; Stoughton, 2000; Wu et al., 2000; Stoughton and Zhu, 2004; Wu et al., 2005). However, effects of strain path changes have not been studied for HCP polycrystalline sheets. This Chapter examines the path-dependency of the formability for HCP polycrystalline sheets. In these simulations, non-proportional loading histories are developed using combinations of two linear strain paths. The first strain path, the pre-strain operation, is common to all loading histories. Subsequent linear deformation paths are imposed by varying the strain-rate ratio for the development of an FLD applicable to that given pre-strain path and amount.

This Chapter is outlined as follows. In Section 5.2, the EVPSC model is briefly introduced. The problem is formulated in Section 5.3. Followed by the calibration of the models against experimental stress-strain curves, numerical results and discussions are provided in Section 5.4. Finally, Section 5.5 presents conclusions.

5.2 Constitutive Model

The Elastic Visco-Plastic Self-Consistent (EVPSC) model for polycrystals recently developed by Wang et al. (2010e) is a completely general elastic-viscoplastic, fully anisotropic, self-consistent polycrystal model, applicable to large strains and to any crystal symmetry. Here, we very briefly describe the model. For details we refer to Wang et al. (2010e).

The elastic constitutive equation for a crystal is:

$$\overset{\nabla}{\sigma}^* = \mathcal{L} : \mathbf{d}^e - \sigma \text{tr}(\mathbf{d}^e) \quad (5.1)$$

where \mathcal{L} is the fourth order elastic stiffness tensor, \mathbf{d}^e is the elastic strain rate tensor and $\overset{\nabla}{\sigma}^*$ is the Jaumann rate of the Cauchy stress σ based on the lattice spin tensor ω^e . The single crystal elastic anisotropy is included in \mathcal{L} through the crystal elastic constants C_{ij} (Wang and Mora, 2008). If elasticity is assumed to be isotropic, \mathcal{L} is a function only of Young's modulus, E , and Poisson's ratio, ν .

Plastic deformation of a crystal is assumed to be due to crystallographic slip and twinning on systems $(\mathbf{s}^\alpha, \mathbf{n}^\alpha)$. Here, \mathbf{s}^α and \mathbf{n}^α are the slip/twinning direction and the direction normal to the slip/twinning plane for system α , respectively. The following

equation gives the grain (crystal) level plastic strain rate d^p (Asaro and Needleman, 1985):

$$d^p = \dot{\gamma}_0 \sum_{\alpha} P^{\alpha} \left| \tau^{\alpha} / \tau_{cr}^{\alpha} \right|^{(1/m-1)} (\tau^{\alpha} / \tau_{cr}^{\alpha}) \quad (5.2)$$

where $\dot{\gamma}_0$ is a reference value for the slip/twinning rate, m is the slip/twinning rate sensitivity, $P^{\alpha} = (s^{\alpha} n^{\alpha} + n^{\alpha} s^{\alpha})/2$ is the Schmid tensor for system α , and $\tau^{\alpha} = \sigma : P^{\alpha}$ and τ_{cr}^{α} are the resolved shear stress (RSS) and critical resolved shear stress (CRSS) for system α , respectively. The evolution of τ_{cr}^{α} due to hardening processes is given by:

$$\dot{\tau}_{cr}^{\alpha} = \frac{d\hat{\tau}^{\alpha}}{d\gamma_{ac}} \sum_{\beta} h^{\alpha\beta} \dot{\gamma}^{\beta} \quad (5.3)$$

where $\gamma_{ac} = \sum_{\alpha} |\gamma^{\alpha}|$ is the accumulated shear strain in the grain, and $h^{\alpha\beta}$ are the latent hardening coupling coefficients, which empirically account for the obstacles on system α associated with system β . $\hat{\tau}^{\alpha}$ is the threshold stress and is characterized by:

$$\hat{\tau}^{\alpha} = \tau_0^{\alpha} + (\tau_1^{\alpha} + h_1^{\alpha} \gamma_{ac}) (1 - \exp(-h_0^{\alpha} \gamma_{ac} / \tau_1^{\alpha})) \quad (5.4)$$

Here, τ_0 , h_0 , h_1 and $\tau_0 + \tau_1$ are the initial CRSS, the initial hardening rate, the asymptotic hardening rate, and the back-extrapolated CRSS, respectively. The polar nature of twinning is incorporated into the model simply by specifying a very large CRSS for the reverse direction.

Various homogenization methods have been developed to characterize the mechanical behavior of a polycrystalline aggregate from the responses of their single crystals. Among them, the most popular Taylor model assumes that the strains of each grain are equal to the imposed macroscopic strains, and the macroscopic stresses are the average of the stresses over all the grains. Another popular homogenizing method is the self-consistent approach: each grain is treated as an ellipsoidal inclusion embedded in a homogeneous effective medium (HEM), which is an aggregate of all the grains. Interactions between each grain and the HEM are described using the Eshelby inclusion formalism (Eshelby, 1957). During each deformation step, the single crystal constitutive rule (which describes the grain-level response) and the self-consistency criteria are solved simultaneously. This ensures that the grain-level stresses and strain rates are consistent with the boundary conditions imposed on the HEM. The behaviour of the inclusion (single crystal) and of the HEM can be linearized as follows (Wang et al., 2010e):

$$d = M^e : \dot{\sigma} + M^v : \sigma + d^0 \quad (5.5)$$

$$D = \bar{M}^e : \dot{\Sigma} + \bar{M}^v : \Sigma + D_0 \quad (5.6)$$

where M^e , M^v and d_0 are the elastic compliance, the visco-plastic compliance, and the back-extrapolated term for the grain, respectively. \bar{M}^e , \bar{M}^v , D , Σ and D_0 are the

corresponding terms for the HEM. The grain-level stress and strain rates are related self-consistently to the corresponding values for the HEM as follows:

$$(\mathbf{d} - \mathbf{D}) = -\tilde{\mathbf{M}}^e : (\dot{\boldsymbol{\sigma}} - \dot{\boldsymbol{\Sigma}}) - \tilde{\mathbf{M}}^v : (\boldsymbol{\sigma} - \boldsymbol{\Sigma}) \quad (5.7)$$

where the interaction tensors $\tilde{\mathbf{M}}^e$ and $\tilde{\mathbf{M}}^v$ are given by:

$$\tilde{\mathbf{M}}^e = (\mathbf{I} - \mathbf{S}^e)^{-1} : \mathbf{S}^e : \bar{\mathbf{M}}^e, \quad \tilde{\mathbf{M}}^v = (\mathbf{I} - \mathbf{S}^v)^{-1} : \mathbf{S}^v : \bar{\mathbf{M}}^v \quad (5.8)$$

Here, \mathbf{S}^e and \mathbf{S}^v are the elastic and visco-plastic Eshelby tensors for a given grain, respectively. \mathbf{I} is the identity tensor.

Different self-consistent schemes (SCSs) depend on different choices for the linearization. Among various SCSs, the Secant SCS employees the following linearization:

$$M_{ijkl}^{v,affine} = \dot{\gamma}_0 \sum_{\alpha} (\tau^{\alpha} / \tau_{cr}^{\alpha})^{(1/m-1)} (P_{ij}^{\alpha} P_{kl}^{\alpha} / \tau_{cr}^{\alpha}), \quad d_{0ij}^{affine} = 0 \quad (5.9)$$

while the Affine SCS applies the linearization:

$$M_{ijkl}^{v,affine} = \dot{\gamma}_0 / m \sum_{\alpha} (\tau^{\alpha} / \tau_{cr}^{\alpha})^{(1/m-1)} (P_{ij}^{\alpha} P_{kl}^{\alpha} / \tau_{cr}^{\alpha}), \quad d_{0ij}^{affine} = (1 - 1/m) d_{ij}^s \quad (5.10)$$

With the aid of the Tangent and Secant relation: $\bar{\mathbf{M}}^{v,tangent} = \bar{\mathbf{M}}^{v,secant} / m$ (Hutchinson, 1976), the interaction tensor in the Tangent self-consistent scheme is given by:

$$\tilde{\mathbf{M}}^v = (\mathbf{I} - \mathbf{S}^v)^{-1} : \mathbf{S}^v : \bar{\mathbf{M}}^{v,secant} / m \quad (5.11)$$

Molinari and Tóth (1994) introduced a scalar interaction parameter m^{eff} by tuning the self-consistent predictions with the finite element results. The resulted meff SCS provides an intermediate interaction tensor:

$$\tilde{\mathbf{M}}^v = (\mathbf{I} - \mathbf{S}^v)^{-1} : \mathbf{S}^v : \bar{\mathbf{M}}^{v,secant} / m^{eff} \quad (5.12)$$

The scheme would produce a rigid upper bound solution when $m^{eff} = \infty$. if $m^{eff} = m$ is assumed, this scheme reduces to the Tangent scheme [see also Tomé (1999)]

For details concerning the self-consistent equations associated with the different visco-plastic self-consistent algorithms, we refer the interested reader to Lebensohn et al. (2007).

Very recently, Wang et al. (2010a) evaluated several self-consistent approaches by studying the large strain behaviour of magnesium alloy AZ31B sheet under different deformation processes. It was found that, of the approaches examined, the Affine self-consistent and m^{eff} self-consistent with interaction stiffness between the Secant (stiff) and Tangent (compliant) give the best results. Therefore, the EVPSC model with the Affine self-consistent scheme and m^{eff} self-consistent scheme, together with the classical Taylor model, are employed to study the role of constitutive model on FLDs.

To model the twinning activity, the Predominant Twin Reorientation (PTR) scheme proposed by Tomé et al. (1991) is used. PTR prevents grain reorientation by

twinning until a threshold value A^{th1} is accumulated in any given system and rapidly raises the threshold to a value around $A^{th1} + A^{th2}$.

For simplicity, EVPSC models with the Affine and m^{eff} SCSs are respectively called the Affine and meff models in the rest of the present Chapter.

5.3 Problem formulation and method of solution

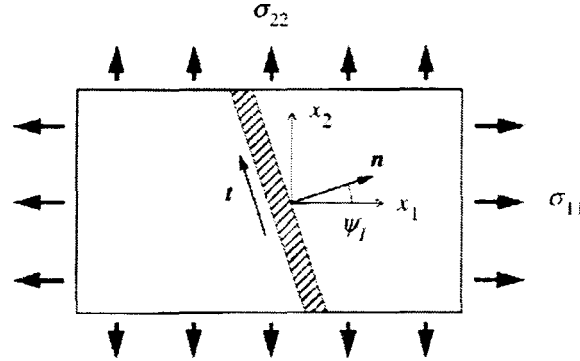


Figure 5.1 The geometry and convention employed in the FLD analysis.

Following the numerical procedure developed by Wu et al. (1997), the EVPSC model outlined above, in conjunction with the M-K approach, is implemented into a numerical code for constructing the FLDs. We assume that the axes x_1 and x_2 define the rolling direction (RD) and the transverse direction (TD) in the plane of the sheet, while x_3 represents the direction normal to the sheet (ND). The basic assumption of the M-K approach is the existence of material imperfections in the form of grooves that is initially inclined at an angle ψ_j with respect to the x_1 reference direction (Figure 5.1). Marciniak and Kuczynski (1967) showed that a slight intrinsic inhomogeneity in load bearing capacity throughout a deforming sheet can lead to unstable growth of strain in the region of the imperfection, and subsequently cause localized necking and failure. In the present Chapter, quantities inside the groove are denoted by $(\)^b$. The thickness along the minimum section in the groove is denoted by $h^b(t)$, with an initial value $h^b(0)$. The initial geometric non-uniformity is defined by

$$f_0 = h^b(0)/h(0) \quad (5.13)$$

with $h(0)$ being the initial sheet thickness outside the imperfection groove.

The deformation outside the imperfection groove is assumed to be:

$$D_{22}/D_{11} = \dot{\epsilon}_{22}/\dot{\epsilon}_{11} = \rho, \quad D_{12} = 0, \quad W_{12} = 0 \quad (5.14)$$

where $\dot{\epsilon}_{11} = D_{11}$ and $\dot{\epsilon}_{22} = D_{22}$ are the (principal) logarithmic strain rates and the W_{ij} values are components of the spin tensor. It is further assumed that $D_{13} = D_{23} = W_{13} = W_{23} = 0$, while D_{33} is specified by the condition $\dot{\sigma}_{33} = 0$.

Under the imposed deformations described in (4.14), the evolution of the groove orientation ψ is given by

$$\dot{\psi} = n_1 n_2 (D_{11} - D_{22}) - (n_1^2 - n_2^2) D_{12} \quad (5.15)$$

where $n_1 = \cos\psi$ and $n_2 = \sin\psi$ are the components of the unit normal to the band (Figure 5.1). Here and consequently, all quantities are in the current configuration.

Equilibrium and compatibility inside and outside the groove are automatically satisfied because uniform deformations are assumed both inside and outside the groove. The compatibility condition at the groove interface is given in terms of the differences in the velocity gradients inside and outside the groove:

$$L_{\xi\eta}^b = L_{\xi\eta} + v_\xi n_\eta \quad (5.16)$$

or

$$D_{\xi\eta}^b = D_{\xi\eta} + (v_\xi n_\eta + v_\eta n_\xi)/2, \quad W_{\xi\eta}^b = W_{\xi\eta} + (v_\xi n_\eta - v_\eta n_\xi)/2 \quad (5.17)$$

where v_ξ are parameters to be determined. Here, and subsequently, Greek indices range from 1 to 2. Equilibrium balance on each side of the interface requires that

$$n_\xi \sigma_{\xi\eta}^b h^b = n_\xi \sigma_{\xi\eta} h \quad (5.18)$$

in the current configuration. A set of incremental equations for v_ξ is now obtained by substituting the incremental constitutive equations (5.1) into the incremental form of (5.18), using (5.17) to eliminate the strain increments $D_{\xi\eta}^b$. Together with the condition $\dot{\sigma}_{33}^b = 0$, this furnishes three algebraic equations for solving v_1 , v_2 and the unknown D_{33}^b . The sheet thickness outside the band h and inside the band h^b are updated based on the relations

$$\dot{h} = D_{33} h, \quad \dot{h}^b = D_{33}^b h^b \quad (5.19)$$

The onset of sheet necking is defined by the occurrence of a much higher maximum principal logarithmic strain rate inside the band than outside, taken here as the condition $\dot{\epsilon}^b/D_{11} \geq 10^5$, where $\dot{\epsilon}^b$ represents the maximum strain rate inside the band. The corresponding principal logarithmic strains ϵ_{11}^* and ϵ_{22}^* , and principal stresses σ_{11}^* and σ_{22}^* outside the band are the limit strains and limit stresses, respectively. For a real sheet, numerous initial imperfections can exist with different orientations. A conservative estimate of the forming limit strain is that obtained from limit strain values for various values of the initial band orientation ψ_i , and then selecting the minimum value as the actual forming limit strain. The entire FLD of a sheet is determined by repeating the procedure for different strain paths outside the band as prescribed by the strain-rate ratio ρ . To study path-dependency of FLDs, non-proportional loading histories are developed using combinations of two linear strain paths. The first strain path; i.e. the pre-

strain operation, is common to all loading histories. Subsequent linear deformation paths are imposed by varying the strain-rate ratio for the development of an FLD applicable to that given pre-strain path and amount.

5.4 Results and discussions

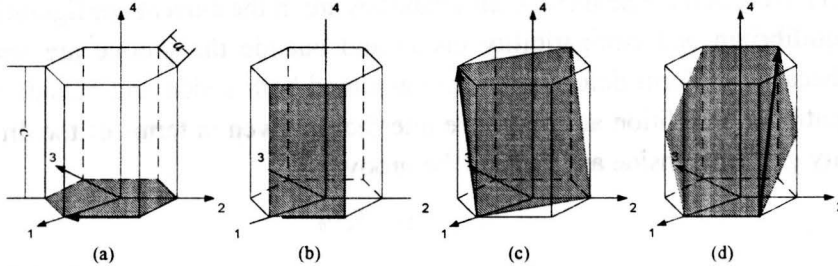


Figure 5.2 Plastic deformation modes in hexagonal structure: (a) Basal $\langle a \rangle$ slip systems, (b) Prismatic $\langle a \rangle$ slip systems, (c) Pyramidal $\langle c+a \rangle$ slip systems, and (d) extension twin.

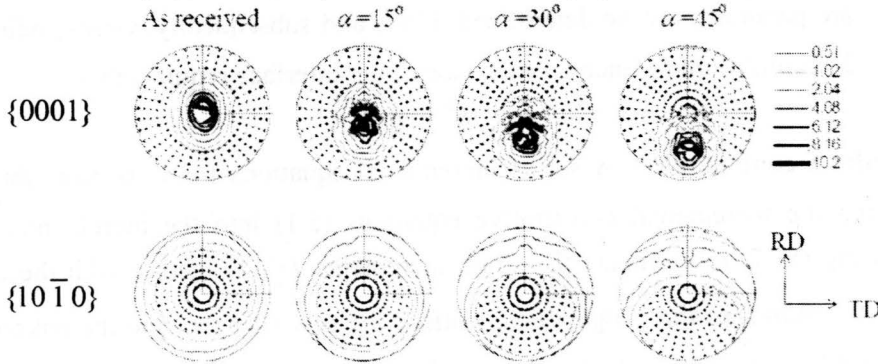


Figure 5.3 Initial textures represented in terms of the $\{0001\}$ and $\{10\bar{1}0\}$ pole figures.

We assume that plastic deformation is due to slip in the Basal $\langle a \rangle$ ($\{0001\} \langle 11\bar{2}0 \rangle$), Prismatic $\langle a \rangle$ ($\{10\bar{1}0\} \langle 11\bar{2}0 \rangle$) and Pyramidal $\langle c+a \rangle$ ($\{\bar{1}\bar{1}22\} \langle \bar{1}\bar{1}23 \rangle$) slip systems, and twinning on the $\{10\bar{1}2\} \langle \bar{1}011 \rangle$ extension twin system (see **Figure 5.2**). It is noted that Pyramidal $\langle a \rangle$ ($\{1\bar{1}01\} \langle 11\bar{2}0 \rangle$) slip system is frequently referred to in the magnesium literature. However, it has been reported that the Prismatic $\langle a \rangle$ slip is more important than Pyramidal $\langle a \rangle$ slip (Ward Flynn et al., 1961). Furthermore, as pointed out by Agnew et al. (2001), the kinds of deformations and crystallographic textures induced by Pyramidal $\langle a \rangle$ slip could also result from a combination of Basal $\langle a \rangle$ slip and Prismatic $\langle a \rangle$ slip. Therefore, Pyramidal $\langle a \rangle$ is not included in the present Chapter.

Table 5.1 List of values of material constants for various polycrystal plasticity models.

| Model | Mode | τ_0 | τ_1 | h_0 | h_1 | Latent | A^{th1} | A^{th2} |
|--------|-----------|----------|----------|-------|-------|--------|-----------|-----------|
| Taylor | Basal | 13 | 4 | 5000 | 30 | 4 | | |
| | Prismatic | 73 | 35 | 400 | 60 | 4 | | |

| | | | | | | | | |
|--|----------------|-----|-----|------|-----|---|------|---|
| | Pyramidal | 110 | 83 | 2500 | 0 | 2 | | |
| | Extension Twin | 31 | 0 | 0 | 0 | 4 | 0.82 | 0 |
| Affine | Basal | 9 | 1 | 5000 | 25 | 4 | | |
| | Prismatic | 79 | 40 | 590 | 50 | 4 | | |
| | Pyramidal | 100 | 100 | 5000 | 0 | 2 | | |
| | Extension Twin | 47 | 0 | 0 | 0 | 4 | 0.72 | 0 |
| m^{eff} ($m^{\text{eff}}=0.1$) | Basal | 17 | 6 | 3800 | 100 | 4 | | |
| | Prismatic | 77 | 33 | 650 | 50 | 4 | | |
| | Pyramidal | 148 | 35 | 9600 | 0 | 2 | | |
| | Extension Twin | 33 | 0 | 0 | 0 | 4 | 0.81 | 0 |

The reference material studied in the present Chapter is a magnesium alloy AZ31B sheet at room temperature. The experimentally measured mechanical behaviour of the sheet has been reported by Jain and Agnew (2007). The measured $\{0001\}$ and $\{10\bar{1}0\}$ pole figures for the as-received reference sheet are shown in **Figure 5.3**. This is a typical rolling texture with major and minor peaks close to ND, at about 5° and -5° along the RD, respectively. **Figure 5.3** also shows the pole figures obtained by rotating the reference texture by an angle α about TD. In the $\{0001\}$ pole figures, this rotation results in a vertical downward translation of the peaks in the reference texture (i.e. a downward translation of the peaks along RD). The intensity of the basal texture as a function of tilted angle α is shown in Fig. 4. The intensity is calculated as the ratio of the number of grains with a maximum orientation difference to the ideal basal orientation of less than 15° , to the total number of grains. The ideal basal grain corresponds to perfect alignment of the basal pole with the normal direction. It is interesting to note that the calculated intensity for $\alpha=5^\circ$ is higher than for $\alpha=0^\circ$ (reference texture). The reason for this is that the reference texture has its major peak at around 5° with respect to the RD. For $\alpha=5^\circ$, this peak is translated into the centre of the pole figure (i.e., the ideal orientation), resulting in the observed intensification of the basal texture. Nevertheless, the intensity decreases rapidly when the tilt angle is relatively large.

The reference slip/twinning rate, $\dot{\gamma}_0$, and the rate sensitivity, m , assumed to be same for all slip/twinning systems, are taken as 0.001s^{-1} and 0.05, respectively, unless otherwise mentioned. We further assume that elasticity is isotropic with Young's modulus $E = 2 \times 10^5 \text{MPa}$ and Poisson's ratio $\nu = 0.33$. Values of the other material parameters are estimated by fitting numerical simulations of uniaxial tension and compression along the RD to the corresponding experimental data for the reference sheet. In these simulations, a strain rate of $D_{11} = 0.001\text{s}^{-1}$ is prescribed in the loading direction; the only non-zero stress component is the normal stress along the loading direction. All of the strains are allowed to develop freely. Thus, in addition to the normal strains in the width and thickness directions, three shear strains are allowed to develop. Since the c -axes of the constituent grains are preferentially oriented normal to RD in the reference texture, extension

twinning contributes little to plastic deformation in uniaxial tension along the RD, but is the predominant plastic deformation mode in uniaxial compression at small strains. Thus, values for the material parameters associated with slip systems are determined from uniaxial tension along the RD, while values for the material parameters associated with twinning are determined from uniaxial compression along the RD. **Figure 5.5** presents the uniaxial tension and compression true stress and plastic strain curves along the RD. The importance of twinning in compression is clearly revealed by the characteristic S-shape of the flow curve. The Taylor model and EVPSC model associated with Affine self-consistent scheme and m-effective scheme fit the experimental stress strain curves well. **Table 5.1** contains the material parameters obtained from the simulations. These parameters are used in all subsequent simulations.

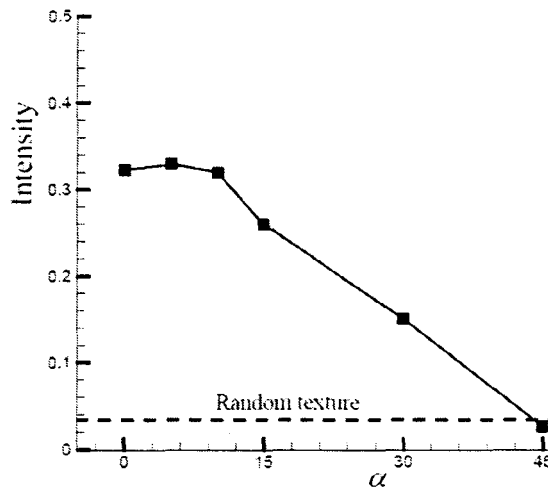


Figure 5.4 The intensity of basal texture as a function of tilted angle α .

It is worth mentioning that $E = 45\text{GPa}$ is frequently referred to in the magnesium literature. Wang et al. (2010e) have shown that the predicted stress-strain curves and texture evolution based on the EVPSC are not sensitive to the value of Young's modulus and are very close to those based on the VPSC models at large strains for monotonic loading. For example, the calculated stress-strain curves shown in **Figure 5.5** are not significantly dependent on the value of Young's modulus and are almost the same as the ones according to the VPSC model at large strains. Furthermore, with the value of the Young's modulus used, $E = 200\text{GPa}$, responses of the sheets considered are expected to be nearly rigid plastic, and the predictions based on the EVPSC model should be almost the same as those based on the VPSC model, even at small strains. Thus, without losing generality, using a very high value of Young's modulus makes it easy for us to validate the EVPSC model based FLD code because the difference in predictions between the EVPSC and VPSC is expected to be very small during the entire deformation process.

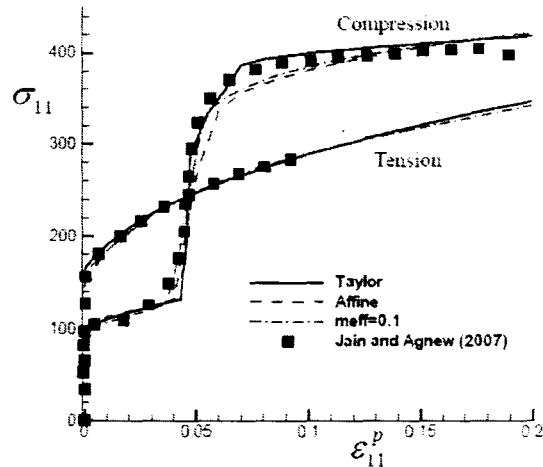


Figure 5.5 True stress and plastic strain curves under uniaxial tension/compression along the RD. The experimental data are taken from Jain and Agnew (2007).

We proceed by constructing FLDs using the value of the material parameters determined above. In all the simulations reported in the present Chapter, the initial geometric non-uniformity is taken as $f_0 = 0.99$. **Figure 5.6** shows the predicted FLDs for the reference sheet based on the Taylor, Affine and meff models. Generally speaking, all the models predict similar overall FLDs, which are analogical to the one obtained by Neil and Agnew (2009) at room temperature. It is seen from **Figure 5.6** that the predicted major limit strain ϵ_{11}^* decreases with ρ to reach its lowest point at $\rho \approx 0.1$ for all the models, and then increases until $\rho = 0.4, 0.2$ and 0.3 for the Taylor, Affine and meff models, respectively. With further increasing ρ , ϵ_{11}^* once again decreases. It is interesting to note that the "hump" shown in **Figure 5.6** in the right-hand side of the predicted FLDs was also found by Chino et al. (2007) from the measured FLDs for magnesium alloy AZ31 sheet at elevated temperature. As mentioned previously, in the simulations we have scanned every 5° of a range of ψ_I and then determined the critical groove angle that gives the minimum localization strain, i.e. the limit strain. **Figure 5.7** gives the predicted critical groove orientations. It is seen that, for all the models employed, a groove oriented at $\psi_I = 0$ is favourable for necking when $-0.4 \leq \rho \leq 0.8$, while the critical groove orientation $\psi_I = 5^\circ$ is found under uniaxial tension ($\rho = -0.5$). At equi-biaxial tension ($\rho = 1$) the critical groove orientations $\psi_I = 10^\circ, 20^\circ, 10^\circ$ are calculated based on the Taylor, Affine and meff models, respectively. When $\rho = 0.9$, the critical groove orientation $\psi_I = 10^\circ$ is found for the meff model, while a groove oriented at $\psi_I = 0^\circ$ is favourable for the Taylor and Affine models.

Previous studies have indicated that FLDs are usually sensitive to the material rate sensitivity (Hutchinson and Neale, 1977; Wu et al., 1997). **Figure 5.8** shows the change in the predicted FLD based on the Affine model when the value of the material rate

sensitivity m is decreased from 0.05 to 0.02. Decreasing the rate sensitivity tends to degrade the hardening at large strains. Consistent with this, **Figure 5.8** shows that the limit strain is decreased relative to that in **Figure 5.6**. The effect of m on FLDs shown in **Figure 5.8** is similar to that based on the M–K approach in conjunction with phenomenological plasticity (Neale and Chater, 1980) and crystal plasticity for FCC polycrystals (Wu et al., 1997).

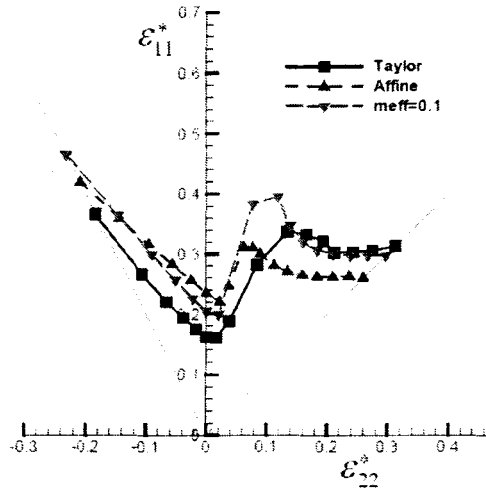


Figure 5.6 Predicted forming limit diagrams for the reference sheet based on various polycrystal plasticity models.

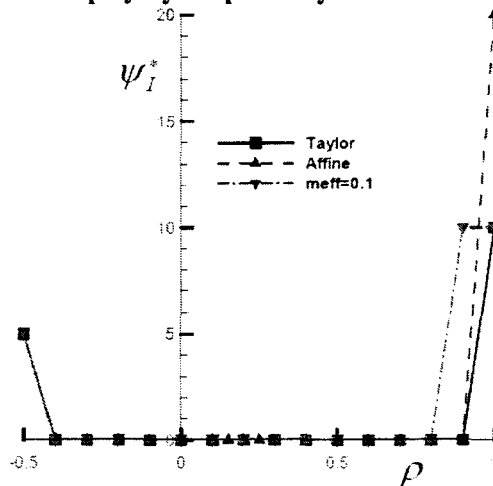


Figure 5.7 Predicted critical groove orientations for the reference sheet based on various polycrystal plasticity models.

It is generally accepted that texture evolution has a significant effect on the initiation and propagation of shear bands in FCC polycrystalline metals (Inal et al., 2002a; b). In this Chapter, repeating calculations reported in **Figure 5.6** but turning off the texture evolution assesses the influence of the texture evolution on FLDs. Numerical results based on the Affine model are presented in **Figure 5.9**. It is observed that texture

evolution has a negligible effect on limit strains for strain paths nearby in-plane plane strain tension. However, texture evolution decreases the limit strains significantly when $\rho \geq 0.4$ or $\rho \leq -0.3$. The predicted effect of texture evolution shown in Figure 5.9 is opposite to those found for FCC and BCC polycrystals. Wu et al. (2004a; 2007a) have reported that texture evolution significantly increases the limit strains for strain paths $\rho \geq 0$ for FCC polycrystals, while Inal et al. (2005) have found that texture evolution has a negligible influence on predicted FLDs for BCC polycrystals.

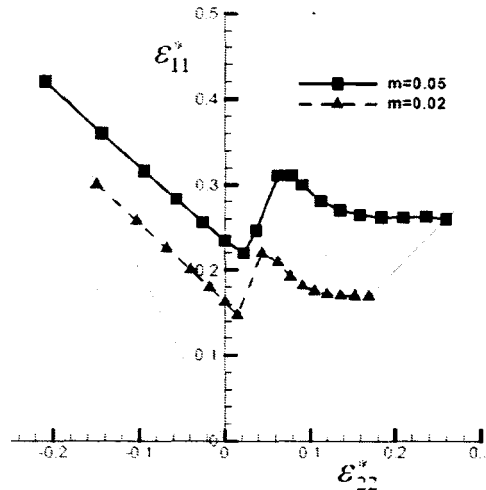


Figure 5.8 Influence of the material rate sensitivity parameter m on the predicted FLDs for the reference sheet based on the Affine model.

The effects of initial texture on predicted FLDs have been extensively studied for FCC and BCC polycrystalline sheets (Wu et al., 1997; Wu et al., 1998). Figures 5.10-12 present the influence of initial texture on the predicted FLDs based on the Taylor model, Affine model and meff model, respectively. All the models predict a general trend: formability of HCP sheets can be improved by weakening the basal texture through rotating the reference texture by an angle α about the TD. It is noted that when $\alpha = 45^\circ$ the intensity of basal texture is almost the same as that in a random texture (see Figure 5.4), and consequently the predicted limit strains are comparable to those for random texture. Fig. 13 shows the predicted critical groove orientations when $\alpha = 45^\circ$. It is seen that a groove oriented at $\psi_i = 0^\circ$ is favourable for necking when $-0.3 \leq \rho \leq 0.4$, for all models employed. Based on the Taylor model, the critical groove orientations $\psi_i = 0^\circ$, 5° and 10° are found for $\rho = -0.4$, $\rho = -0.5$ and $\rho \geq 0.9$, respectively. According to the meff model, $\psi_i = 10^\circ$ is the critical groove orientation for strain paths $\rho \geq 0.5$ or $\rho \leq -0.4$. The critical groove orientations $\psi_i = 5^\circ$ and 10° are found respectively for $\rho = -0.5$ and $\rho \geq 0.8$ if the Affine model is applied. The effect of basal texture on formability is even more clearly exhibited in Figure 5.14, which shows the predicted limit strain versus the tilted angle α under in-plane plane strain tension ($\rho = 0$) based on

various models. It is clear that the predicted necking strain is dramatically increased when the tilted angles $\alpha > 15^\circ$.

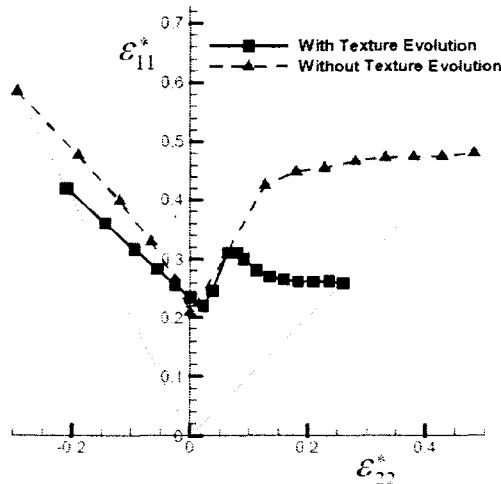


Figure 5.9 Influence of texture evolution on the predicted FLDs for the reference sheet based on the Affine model.

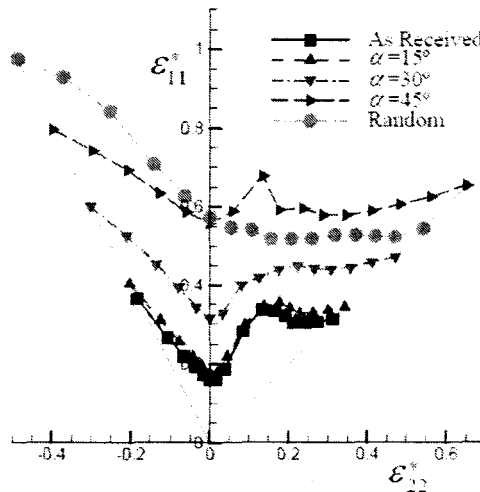


Figure 5.10 Influence of initial texture on the predicted FLDs based on the Taylor model.

Figures 5.10-14, together with Figures 5.6 and 5.7, clearly indicate that if values of material parameters in the constitutive models are determined by best-fitting the same experimental data, the constitutive models predict similar FLDs. In other words, the difference in the predicted FLDs between various models is quantitative rather than qualitative.

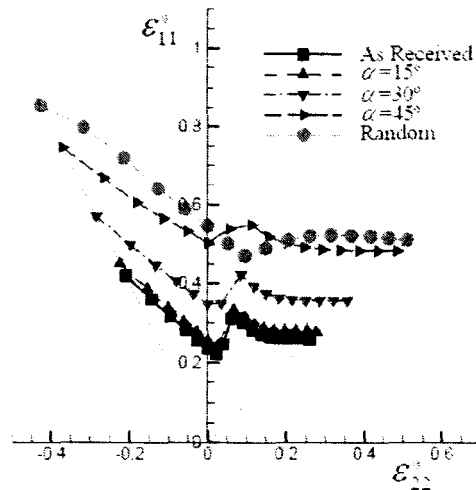


Figure 5.11 Influence of initial texture on the predicted FLDs based on the Affine model.

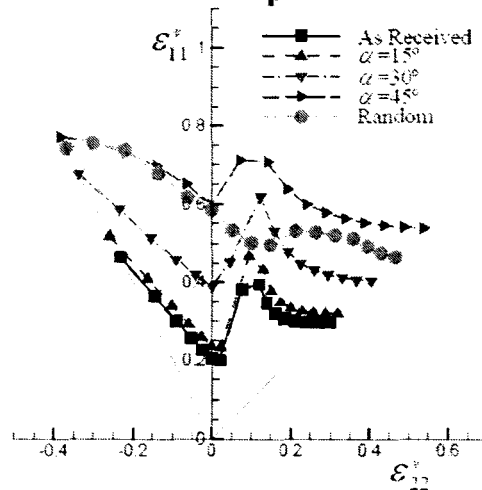


Figure 5.12 Influence of initial texture on the predicted FLDs based on the meff model.

Finally, the effects of strain path changes on FLDs for the reference sheet are numerically studied based on the Affine model. The sheet is pre-strained respectively in uniaxial tension ($\rho = -0.5$), in-plane plane strain tension ($\rho = 0$) and equi-biaxial tension ($\rho = 1$). When the designed pre-strain level is reached, the current imperfection f and deformation state inside and outside the groove are used as the starting state for the subsequent strain path in the FLD analysis.

Figure 5.15 shows FLDs for both the as-received and sheets pre-strained in uniaxial stretching up to $\epsilon_{11} = 0.1$ and 0.15 , respectively. It is clear that uniaxial pre-straining not only shifts the whole FLDs to the left, but also shifts the FLDs upwards. The use of uniaxial tension pre-strain can thus lead to large regions of strain path enhanced formability, where strain states can be reached through non-proportional histories which could not be achieved by proportional histories.

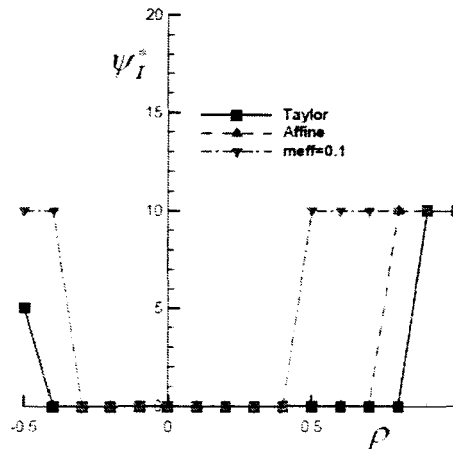


Figure 5.13 Predicted critical groove orientations for the initial texture rotated 45° around TD based on various polycrystal plasticity models.

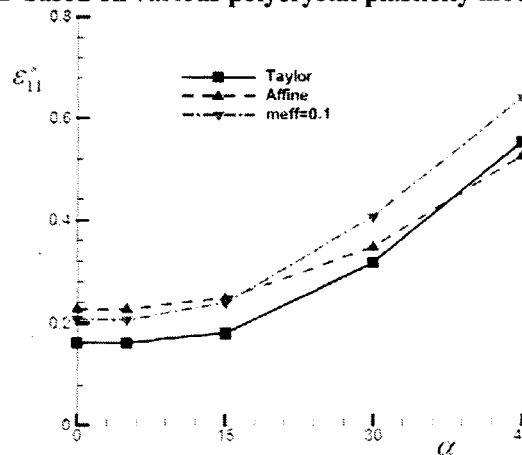


Figure 5.14 Influence of basal texture on the predicted limit strain under in-plane plane strain tension ($\rho=0$).

Figure 5.16 shows the predicted FLDs following in-plane plane strain tension operations. As expected, the limit strain for in-plane plane strain tension is not affected by the pre-straining. The FLD shape exhibits a trend of changing from U towards V due to the pre-straining. More specifically, for strain paths $\rho \geq 0.3$, it is found that the pre-straining has almost no effect on the limit strain ϵ_{11} , but it dramatically decreases the limit strain ϵ_{22} . For subsequent strain paths $\rho < 0$, the pre-straining reduces both limit strains ϵ_{11} and ϵ_{22} . The FLD predicted following equi-biaxial pre-strain is shown in Figure 5.17. The formability associated with subsequent in-plane plane strain tension following the equi-biaxial tension pre-strain is predicted to shift to slightly lower major strain and to significantly increase the minor strain. This results in lowering the forming limits for most strain combinations in the region to the right of in-plane plane strain tension.

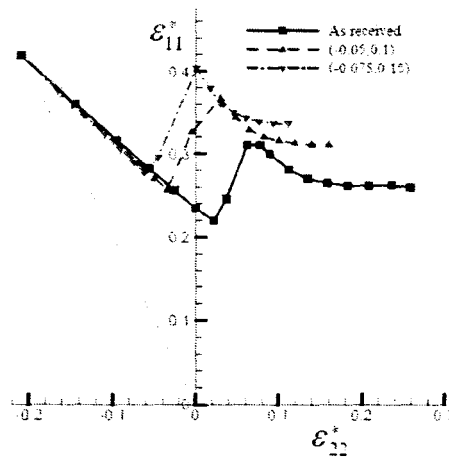


Figure 5.15 Predicted FLDs for the reference sheet pre-strained to different levels in uniaxial tension ($\rho = -0.5$) based on the Affine model.

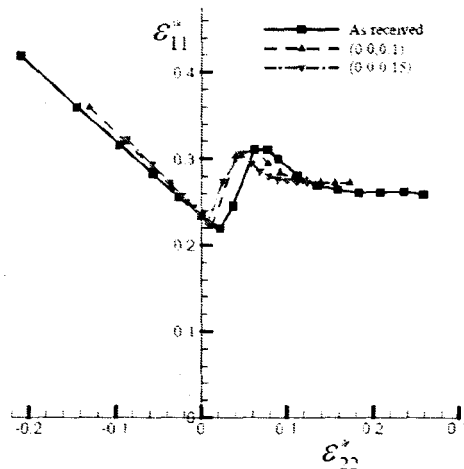


Figure 5.16 Predicted FLDs for the reference sheet pre-strained to different levels in in-plane plane strain tension ($\rho = 0$) based on the Affine model.

Figures 5.15-17 clearly indicate that the FLD of the HCP sheet is very sensitive to strain path changes. The limit strains could be either raised or lowered depending on the nature of the strain path change. This observation is similar to the general trends of effects of strain path changes on forming limits in steel and aluminum sheets (Laukonis and Ghosh, 1978; Graf and Hosford, 1994).

As mentioned previously, extensive researches on FCC and BCC polycrystalline sheets have confirmed that while the FLD is very sensitive to strain path changes, the FLSD is much less path-dependent (Stoughton, 2000; Wu et al., 2000; Wu et al., 2005). However, the FLSD and its path-dependency have not been studied for HCP polycrystalline sheets. Figure 5.18 gives the predicted limit stresses under proportional (linear) and non-proportional loading histories, shown as different symbols in the figure. For example, the legend "(-0.075, 0.15)" indicates that the sheet is pre-strained in strain

path $\rho = -0.075/0.15 = -0.5$ up to strains $\varepsilon_{22} = -0.075$ and $\varepsilon_{22} = 0.15$. It is noted that in addition to the three pre-strains reported in Figures 5.15-17, Figure 5.18 also includes a case with the legend "(0.03, 0.15)", in which the sheet is pre-strained in strain path $\rho = 0.03/0.15 = 0.2$ up to strains $\varepsilon_{22} = 0.03$ and $\varepsilon_{11} = 0.15$. It is clear that the predicted FLSDs under non-proportional loading histories are close to the FLSD under linear loading. Therefore, the predicted FLSD is not sensitive to strain path changes for magnesium alloy AZ31B sheet.

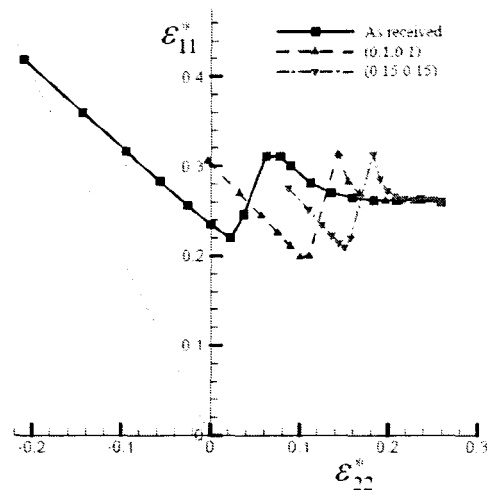


Figure 5.17 Predicted FLDs for the reference sheet pre-strained to different levels in equibiaxial tension ($\rho = 1$) based on the Affine model.

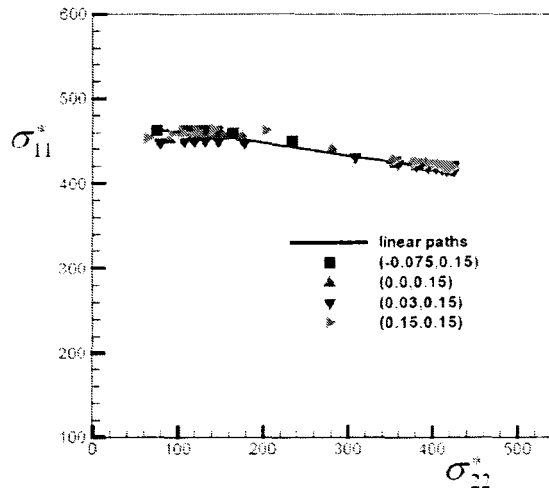


Figure 5.18 Predicted limit stresses for the reference sheet pre-strained in various different pre-straining paths indicated by different symbols based on the Affine model.

It is worth mentioning that the effects of strain path changes on the predicted FLDs and FLSDs shown in Figures 5.15-18 are based on the Affine model. However, similar results have been obtained by using the Taylor and meff models as well.

5.5 Conclusions

In this Chapter, we have calculated FLDs based on the classical Taylor model and the recently developed EVPSC model with various self-consistent schemes, in conjunction with the M-K approach, for magnesium alloy AZ31B sheet. In all the polycrystal plasticity models considered, both slip and twinning contribute to plastic deformations. The material parameters for the various models were first fitted to experimental uniaxial tension and compression curves along the RD and then used to predict FLDs. The effects of initial texture, texture evolution, strain rate-sensitivity, and strain path changes on forming limits have been studied. The numerical results have been found to be in good qualitative agreement with experimental observations. The following conclusions can be drawn:

- 1) Formability of HCP sheets can be improved by weakening the basal texture through equal channel angular extrusion, torsion extrusion, and differential speed rolling even without grain refinement.
- 2) If values of material parameters in constitutive models are determined by best-fitting the same experimental data, the constitutive models predict similar FLDs for magnesium alloy AZ31B sheet. In other words, the difference in the predicted FLDs between various models is quantitative rather than qualitative.

While the FLD is very sensitive to strain path changes, the FLSD is much less path-dependent. This implies that the FLSD is much more favourable than the FLD in representing forming limits in the numerical simulation of sheet metal forming processes.

Chapter 6. General conclusions

First, a finite strain elastic-viscoplastic self-consistent model (EVPSC) for polycrystalline materials has been developed. At the grain level, both slip and twinning are included as the plastic deformation mechanisms, while elastic anisotropy is accounted for in the elastic moduli. The transition from single crystal to polycrystal is based on a completely self-consistent approach based on an approximate interaction equation originally proposed by Kouddane et al. (1993). As expected, at large monotonic strains elasticity saturates and the EVPSC model gives results very close to the VPSC model: the differences in the predicted stress-strain curves and texture evolution are negligible for monotonic loadings. For deformations involving elasto-plastic transients associated with unloading and strain path changes, EVPSC predicts clear and gradual transitions, while VPSC gives stress discontinuities because the model is not able to model elastic deformation. Through the simulation of a stress relaxation test in HCP, the proposed EVPSC model captures the effect of strain rate and elastic stiffness in the macroscopic mechanical response. The proposed EVPSC model is very flexible to implement sophisticated descriptions for slip, twinning, and hardening.

Secondly, various self-consistent schemes of EVPSC/VPSC model have been evaluated by studying large strain behavior of magnesium alloy AZ31B sheet under different deformation processes. An assessment of the predictive capability of the polycrystal plasticity models has been made based on comparisons of the predicted and experimental stress responses and R values. It is interesting to point out that the estimated values of the material parameters for the classical Taylor and Secant models were found to be the same, and the predictions of these two models were almost the same for all the deformation processes studied in the present Chapter. An assessment of the predictive capability of the VPSC model with the Secant scheme also applied to the classic Taylor model. It has been demonstrated that, among the models examined, the VPSC model with the Affine self-consistent model gives the best overall performance and requires no artificial tuning as does the meff scheme. The numerical results have clearly indicated that the R values under uniaxial tension and compression within the sheet plane evolve remarkably with imposed strain. This suggests that using R values measured at a given strain to determine anisotropic constants in anisotropic yield functions for HCP polycrystals is not appropriate for other strains.

The recently developed large strain elastic visco-plastic self-consistent (EVPSC) model, which incorporates both slip and twinning deformation mechanisms, has been used to study lattice strain evolution in conventional extruded magnesium alloy AZ31 under uniaxial tension and compression. The predictions have been compared with in-situ experimental measurements obtained using in-situ neutron diffraction. The EVPSC model can qualitatively and almost quantitatively predict the evolution of lattice strains.

For the first time, the stress relaxation and creep effects associated with in-situ neutron measurements have been modeled for strain controlled and stress controlled measuring methods, respectively. It has been found that the stress relaxation (strain control) has a more significant effect on the lattice strain measurements than the creep does. It has been also observed that although the creep does not significantly affect the trend of the lattice strain evolution, a better agreement with the experiments is found if creep is included in the simulations. Numerical results have suggested that enforcing constant stress at each measuring point may be a more efficient situation for comparing experiments and simulations.

Finally, FLDs have been calculated based on the classical Taylor model and the recently developed EVPSC model with various self-consistent schemes, in conjunction with the M-K approach, for magnesium alloy AZ31B sheet. The effects of initial texture, texture evolution, strain rate-sensitivity, and strain path changes on forming limits have been studied. The numerical results have been found to be in good qualitative agreement with experimental observations. Formability of HCP sheets can be improved by weakening the basal texture through equal channel angular extrusion, torsion extrusion, and differential speed rolling, etc. even without grain refinement. If values of material parameters in constitutive models are determined by best-fitting the same experimental data, the constitutive models predict similar FLDs for magnesium alloy AZ31B sheet. In other words, the difference in the predicted FLDs between various models is quantitative rather than qualitative. While the FLD is very sensitive to strain path changes, the FLSD is much less path-dependent. This implies that the FLSD is much more favourable than the FLD in representing forming limits in the numerical simulation of sheet metal forming processes.

Bibliography

- Agnew, S.R., 2002. Plastic anisotropy of magnesium alloy AZ31B sheet. TMS Annual Meeting, Magnesium Technology 2002.169-174.
- Agnew, S.R., Brown, D.W., Tomé, C.N., 2006a. Validating a polycrystal model for the elastoplastic response of magnesium alloy AZ31 using in situ neutron diffraction. *Acta Materialia* 54, 4841-4852.
- Agnew, S.R., Duygulu, O., 2005. Plastic anisotropy and the role of non-basal slip in magnesium alloy AZ31B. *International Journal of Plasticity* 21, 1161-1193.
- Agnew, S.R., Horton, J.A., Lillo, T.M., Brown, D.W., 2004. Enhanced ductility in strongly textured magnesium produced by equal channel angular processing. *Scripta Materialia* 50, 377-381.
- Agnew, S.R., Senn, J.W., Horton, J.A., 2006b. Mg sheet metal forming: Lessons learned from deep drawing Li and Y solid-solution alloys. *JOM* 58, 62-69.
- Agnew, S.R., Tomé, C.N., Brown, D.W., Holden, T.M., Vogel, S.C., 2003. Study of slip mechanisms in a magnesium alloy by neutron diffraction and modeling. *Scripta Materialia* 48, 1003-1008.
- Agnew, S.R., Yoo, M.H., Tomé, C.N., 2001. Application of texture simulation to understanding mechanical behavior of Mg and solid solution alloys containing Li or Y. *Acta Materialia* 49, 4277-4289.
- Ahzi, S., Asaro, R.J., Parks, D.M., 1993. Application of crystal plasticity theory for mechanically processed bscCo superconductors. *Mechanics of Materials* 15, 201-222.
- Akhtar, A., Teghtsoonian, E., 1969a. Solid solution strengthening of magnesium single crystals-I alloying behaviour in basal slip. *Acta Metallurgica* 17, 1339-1349.
- Akhtar, A., Teghtsoonian, E., 1969b. Solid solution strengthening of magnesium single crystals-II the effect of solute on the ease of prismatic slip. *Acta Metallurgica* 17, 1351-1356.
- Althuler, T.L., Christian, J.W., 1966. Low temperature twinning in pure iron. *Acta Metallurgica* 14, 903-908.
- Anand, L., Kalidindi, S.R., 1994. The process of shear-band formation in plane-strain compression of FCC metals - effects of crystallographic texture. *Mechanics of Materials* 17, 223-243.
- Arrieux, R., 1995. Determination and use of the forming limit stress diagrams in sheet-metal forming. *Journal of Materials Processing Technology* 53, 47-56.
- Arrieux, R., Bedrin, C., Boivin, M., 1982. Determination of an intrinsic forming limit stress diagram for isotropic metal sheets. in *Proceedings of the 12th Biennial Congress IDDRG*, pp. 61-71.
- Asaro, R.J., Needleman, A., 1985. Texture development and strain hardening in rate dependent polycrystals. *Acta Metallurgica Et Materialia* 33, 923-953.
- Asaro, R.J., Rice, J.R., 1977. Strain localization in ductile single crystals. *Journal of the Mechanics and Physics of Solids* 25, 309-338.
- Avedesian, M.M., Baker, H., 1999. *ASM Speciality Handbook Magnesium and Magnesium Alloys*. ASM International, Materials Park, OH.
- Avery, D.H., Hosford, W.F., Backofen, W.A., 1965. Plastic anisotropy in magnesium sheet. *Transactions of the Metallurgical Society of AIME* 233, 71-78.
- Aydiner, C.C., Bernier, J.V., Clausen, B., Lienert, U., Tome, C.N., Brown, D.W., 2009. Evolution of stress in individual grains and twins in a magnesium alloy aggregate. *Physical Review B* 80, 024113 1-4.
- Bakarian, P.W., Mathewson, C.H., 1943. Slip and twinning in magnesium single crystals at elevated temperatures. *Transactions of the Metallurgical Society of AIME* 152, 226-254.

- Barlat, F., Lege, D.J., Brem, J.C., 1991. A six-component yield function for anisotropic materials. *International Journal of Plasticity* 7, 693-712.
- Barlat, F., Maeda, Y., Chung, K., Yanagawa, M., Brem, J.C., Hayashida, Y., Lege, D.J., Matsui, K., Murtha, S.J., Hattori, S., Becker, R.C., Makosey, S., 1997. Yield function development for aluminum alloy sheets. *Journal of the Mechanics and Physics of Solids* 45, 1727-1763.
- Barlat, F., Yoon, J.W., Cazacu, O., 2007. On linear transformations of stress tensors for the description of plastic anisotropy. *International Journal of Plasticity* 23, 876-896.
- Bassani, J.L., Wu, T.Y., 1991. Latent hardening in single-crystals II. Analytical characterization and predictions. *Proceedings of the Royal Society of London A435*, 21-41.
- Bell, R.L., Cahn, R.W., 1957. The dynamics of twinning and the interrelation of slip and twinning in zinc crystals. *Proceedings of the Royal Society of London A239*, 494-521.
- Berghezan, A., Fourdeux, A., Amelincks, S., 1961. Transmission electron microscopy studies of dislocations and stacking faults in a hexagonal metal: zinc. *Acta Metallurgica* 9, 464-490.
- Bettles, C.J., Gibson, M.A., 2005. Current wrought magnesium alloys: Strengths and weaknesses. *JOM* 57, 46-49.
- Beyerlein, I.J., Tomé, C.N., 2008. A dislocation-based constitutive law for pure Zr including temperature effects. *International Journal of Plasticity* 24, 867-895.
- Boucher, N.A., Christian, J.W., 1972. The influence of pre-strain on deformation twinning in niobium single crystals. *Acta Metallurgica* 20, 581-591.
- Brown, D.W., Agnew, S.R., Bourke, M.A.M., Holden, T.M., Vogel, S.C., Tomé, C.N., 2005. Internal strain and texture evolution during deformation twinning in magnesium. *Materials Science and Engineering A399*, 1-12.
- Budianski, B., Wu, T.T., 1962. Theoretical prediction of plastic strains of polycrystals. In: *Proceedings of the 4th U.S. National Congress on Applied Mechanics*. ASME, New York, pp. 1175-1185.
- Burke, E.C., Hibbard, W.R., 1952. Plastic deformation of magnesium single crystals. *Transactions of AIME* 194, 295-303.
- Byrne, J.G., 1963. Plastic deformation of Mg-Mn alloy single crystals. *Acta Metallurgica* 11, 1023-1027.
- Cahn, R.W., 1954. Twinned crystals. *Advances in Physics* 3, 363-445.
- Carr, D.G., Holden, T.M., Ripley, M.I., Brown, D., Vogel, S.C., 2007. Investigation of grain-scale stresses and modeling of tensile deformation in a zircaloy-4 weldment. *Metallurgical and Materials Transactions* 38A, 2410-2418.
- Cazacu, O., Barlat, F., 2004. A criterion for description of anisotropy and yield differential effects in pressure-insensitive metals. *International Journal of Plasticity* 20, 2027-2045.
- Cazacu, O., Plunkett, B., Barlat, F., 2006. Orthotropic yield criterion for hexagonal closed packed metals. *International Journal of Plasticity* 22, 1171-1194.
- Chaboche, J.L., 1986. Time-independent constitutive theories for cyclic plasticity. *International Journal of Plasticity* 2, 149-188.
- Chaboche, J.L., 2008. A review of some plasticity and viscoplasticity constitutive theories. *International Journal of Plasticity* 24, 1642-1693.
- Chin, G.Y., Hosford, W.F., Mendorf, D.R., 1969. Accommodation of constrained deformation in f.c.c. metals by slip and twinning. *Proceedings of the Royal Society of London A309*, 433-456.
- Chino, Y., Iwasaki, H., Mabuchi, M., 2007. Stretch formability of AZ31 Mg alloy sheets at different testing temperatures. *Materials Science and Engineering A466*, 90-95.
- Chino, Y., Sassa, K., Mabuchi, M., 2008. Enhancement of tensile ductility of magnesium alloy produced by torsion extrusion. *Scripta Materialia* 59, 399-402.

- Christian, J.W., Mahajan, S., 1995. Deformation twinning. *Progress in Materials Science* 39, 1-157.
- Chun, J.S., Byrne, J.G., 1969. Precipitate strengthening mechanisms in magnesium zinc alloy single crystals. *Journal of Materials Science* 4, 861-872.
- Chun, J.S., Byrne, J.G., Bornemann, A., 1969. Inhibition of deformation twinning by precipitates in a magnesium-zinc alloy. *Philosophical Magazine* 20, 219-300.
- Churchman, A.T., 1954. The slip modes of titanium and the effect of purity on their occurrence during tensile deformation of single crystals. *Proceedings of the Royal Society of London A226*, 216-226.
- Clausen, B., Tomé, C.N., Brown, D.W., Agnew, S.R., 2008. Reorientation and stress relaxation due to twinning: Modeling and experimental characterization for Mg. *Acta Materialia* 56, 2456-2468.
- Conrad, H., Robertson, W.D., 1957. Effect of temperature on the flow stress and strain-hardening coefficient of magnesium single crystals. *Transactions of AIME* 209, 503-513.
- Dawson, P., Boyce, D., MacEwen, S., Rogge, R., 2001. On the influence of crystal elastic moduli on computed lattice strains in AA-5182 following plastic straining. *Materials Science and Engineering A313*, 123-144.
- Dawson, P.R., MacEwen, S.R., Wu, P.D., 2003. Advances in sheet metal forming analyses: dealing with mechanical anisotropy from crystallographic texture. *International Materials Reviews* 48, 86-122.
- Del Valle, J.A., Ruano, O.A., 2009. Effect of annealing treatments on the anisotropy of a magnesium alloy sheet processed by severe rolling. *Materials Letters* 63, 1551-1554.
- Emley, E.F., 1966. *Principles of magnesium technology*. Pergamon Press in Oxford, New York.
- Eshelby, J.D., 1957. The determination of the elastic field of an ellipsoidal inclusion, and related problems. *Proceedings of the Royal Society of London A241*, 376-396.
- Eyckens, P., Van Bael, A., Van Houtte, P., 2009. Marciniak-Kuczynski type modelling of the effect of Through-Thickness Shear on the forming limits of sheet metal. *International Journal of Plasticity* 25, 2249-2268.
- Gharghouri, M.A., 1997. Study of the mechanical properties of magnesium-8.5wt% aluminum by in-situ neutron diffraction. Ph.D Thesis. Department of Materials Science and Engineering. McMaster University, Hamilton, Canada.
- Gharghouri, M.A., Weatherly, G.C., Embury, J.D., Root, J., 1999. Study of the mechanical properties of Mg-7.7at.% Al by in-situ neutron diffraction. *Philosophical Magazine A79*, 1671-1695.
- Graf, A., Hosford, W., 1994. The influence of strain-path changes on forming limit diagrams of Al 6111 T-4. *International Journal of Mechanical Sciences* 36, 897-910.
- Groves, G.W., Kelley, E.W., 1963. Independent slip system in crystals. *Philosophical Magazine* 8, 877-887.
- Harren, S.V., 1991. The finite deformation of rate-dependent polycrystals - II: A comparison of the self-consistent and Taylor methods. *Journal of the Mechanics and Physics of Solids* 39, 361-383.
- Hartig, C., Styczynski, A., Kaiser, F., Letzig, D., 2005. Plastic anisotropy and texture evolution of rolled AZ31 magnesium alloys. *Materials Science and Forum* 495-497, 1615-1620.
- Hartt, W.H., Reed-Hill, R.E., 1967. The irrational habit of second-order {10-11}-{10-12} twins in magnesium. *Transactions of the Metallurgical Society of AIME* 239, 1511-1517.
- Hauser, F.E., Landon, P.R., Dorn, J.E., 1958. Deformation and fracture of alpha solid solutions of lithium in magnesium. *Transactions of the ASM* 50, 856-883.
- Hauser, F.E., Starr, C.D., Tietz, L., Dorn, J.E., 1955. Deformation mechanisms in polycrystalline aggregates of magnesium. *Transactions of the ASM* 47, 102-134.

- Hecker, S.S., 1975. Formability of aluminum alloy sheet. *Journal of Engineering Materials and Technology* 97, 66-73.
- Hill, R., 1948. A theory of the yielding and plastic flow of anisotropic metals. *Proceedings of the Royal Society of London A*193, 281-297.
- Hill, R., 1965. Continuum micro-mechanics of elastoplastic polycrystals. *Journal of the Mechanics and Physics of Solids* 13, 89-101.
- Hill, R., 1966. Generalized constitutive relations for incremental deformation of metals crystals by multislip. *Journal of the Mechanics and Physics of Solids* 14, 95-102.
- Hill, R., Rice, J.R., 1972. Constitutive analysis of elastic-plastic crystal at arbitrary strain. *Journal of the Mechanics and Physics of Solids* 20, 401-413.
- Hiwataishi, S., Van Bael, A., Van Houtte, P., Teodosiu, C., 1998. Prediction of forming limit strains under strain-path changes: Application of an anisotropic model based on texture and dislocation structure. *International Journal of Plasticity* 14, 647-669.
- Hosford, W.A., 1979. On yield loci of anisotropic cubic metals. In: *Proceedings of the 7th North American Metalworking Conference, SME, Dearborn, MI*, pp. 191-197.
- Hosford, W.F., 1993 *The Mechanics of Crystal and Textured Polycrystals*. New York: Oxford University Press.
- Hsu, S.S., Cullity, B.D., 1954. On the torsional deformation and recovery of single crystals. *Transactions of AIME* 200, 305-312.
- Huang, X.S., Suzuki, K., Watazu, A., Shigematsu, I., Saito, N., 2008. Mechanical properties of Mg-Al-Zn alloy with a tilted basal texture obtained by differential speed rolling. *Materials Science and Engineering A*488, 214-220.
- Hutchinson, J.W., 1970. Elastic-plastic behavior of polycrystalline metals hardening accounting to Taylor's rule. *Journal of the Mechanics and Physics of Solids* 12, 11-24.
- Hutchinson, J.W., 1976. Bounds and self-consistent estimates for creep of polycrystalline materials. *Proceedings of the Royal Society of London A*348, 101-127.
- Hutchinson, J.W., Neale, K.W., 1977. Influence of strain-rate sensitivity on necking under uniaxial tension. *Acta Metallurgica* 25, 839-846.
- Inal, K., Neale, K.W., Aboutajeddine, A., 2005. Forming limit comparisons for FCC and BCC sheets. *International Journal of Plasticity* 21, 1255-1266.
- Inal, K., Wu, P.D., Neale, K.W., 2002a. Finite element analysis of localization in FCC polycrystalline sheets under plane stress tension. *International Journal of Solids and Structures* 39, 3469-3486.
- Inal, K., Wu, P.D., Neale, K.W., 2002b. Instability and localized deformation in polycrystalline solids under plane-strain tension. *International Journal of Solids and Structures* 39, 983-1002.
- Iwakuma, T., Nemat-Nasser, S., 1984. Finite elastic plastic-deformation of polycrystalline metals. *Proceedings of the Royal Society of London A*394, 87-119.
- Jain, A., Agnew, S.R., 2007. Modeling the temperature dependent effect of twinning on the behavior of magnesium alloy AZ31B sheet. *Materials Science and Engineering A*462, 29-36.
- Kai, M., Horita, Z., Langdon, T.G., 2008. Developing grain refinement and superplasticity in a magnesium alloy processed by high-pressure torsion. *Materials Science and Engineering A*488, 117-124.
- Kaiser, F., Letzig, D., Bohlen, J., Styczynski, A., Hartig, C., Kainer, K.U., 2003. Anisotropic properties of magnesium sheet AZ31. *Materials Science and Forum* 419-422, 315-320.
- Kalidindi, S.R., 1998. Incorporation of deformation twinning in crystal plasticity models. *Journal of the Mechanics and Physics of Solids* 46, 267-290.
- Kalidindi, S.R., 2001. Modeling anisotropic strain hardening and deformation textures in low stacking fault energy fcc metals. *International Journal of Plasticity* 17, 837-860.

- Kalidindi, S.R., Bronkhorst, C.A., Anand, L., 1992. Crystallographic texture evolution in bulk deformation processing of FCC metals. *Journal of the Mechanics and Physics of Solids* 40, 537-569.
- Karafilis, A.P., Boyce, M.C., 1993. A general anisotropic yield criterion using bounds and a transformation weighting tensor. *Journal of the Mechanics and Physics of Solids* 41, 1859-1886.
- Kelley, E.W., Hosford, W.F., 1968a. The deformation characteristics of textured magnesium. *Transactions of the Metallurgical Society of AIME* 242, 654-661.
- Kelley, E.W., Hosford, W.F., 1968b. Plane-strain compression of magnesium and magnesium alloy crystals. *Transactions of the Metallurgical Society of AIME* 242, 5-13.
- King, J.F., 2005. Magnesium roadmap 2004 - priorities for development of magnesium technology and applications in UK. Report for Light Metals Division of the Institute of Materials, Minerals and Mining, the Institute of Materials, Minerals and Mining.
- King, J.F., 2007. Magnesium: commodity or exotic? *Materials Science and Technology* 23, 1-14.
- Kleiner, S., Uggowitzer, P.J., 2004. Mechanical anisotropy of extruded Mg-6% Al-1% Zn alloy. *Materials Science and Engineering A379*, 258-263.
- Knockaert, R., Chastel, Y., Massoni, E., 2002. Forming limits prediction using rate-independent polycrystalline plasticity. *International Journal of Plasticity* 18, 231-247.
- Kocks, U.F., Tomé, C.N., Wenk, H.R., 1998. *Texture and anisotropy*. Cambridge University Press, Cambridge.
- Kocks, U.F., Westlake, D.G., 1967. The importance of twinning for the ductility of CPH polycrystals. *Transactions of the Metallurgical Society of AIME* 239, 1107-1109.
- Koike, J., 2005. Enhanced deformation mechanisms by anisotropic plasticity in polycrystalline Mg alloys at room temperature. *Metallurgical and Materials Transactions* 36A, 1689-1696.
- Koike, J., Kobayashi, T., Mukai, T., Watanabe, H., Suzuki, M., Maruyama, K., Higashi, K., 2003. The activity of non-basal slip systems and dynamic recovery at room temperature in fine-grained AZ31B magnesium alloys. *Acta Materialia* 51, 2055-2065.
- Koike, J., Ohyama, R., 2005. Geometrical criterion for the activation of prismatic slip in AZ61 Mg alloy sheets deformed at room temperature. *Acta Materialia* 53, 1963-1972.
- Kojima, Y., 2000. Platform science and technology for advanced magnesium alloys. *Materials Science Forum* 350-351, 3-17.
- Kouddane, R., Molinari, A., Canova, G.R., 1991. Self-consistent modeling of heterogeneous viscoelastic and elastic-viscoplastic materials. Presented at Mecamat 91, Fontainebleau, France.
- Kouddane, R., Molinari, A., Canova, G.R., 1993. Self-consistent modeling of heterogeneous viscoelastic and elastic-viscoplastic materials. In: Teodosiu, C., Raphanel, J.L., Sidoroff, F. (Eds), *Large Plastic Deformations, Fundamentals and Applications of Metal Forming*. Balkema, Rotterdam, The Netherlands. 121-141.
- Kröner, E., 1958. Berechnung der elastischen Konstanten des Vielkristalls aus den Konstanten des Einkristalls. *Zeitschrift für Physik* 151, 504-518.
- Kröner, E., 1961. Zur plastischen verformung des vielkristalls. *Acta Metallurgica* 9, 155-161.
- Kubota, K., Mabuchi, M., Higashi, K., 1999. Processing and mechanical properties of fine-grained magnesium alloys. *Journal of Materials Science* 34, 2255-2262.
- Kuroda, M., Ikawa, S., 2004. Texture optimization of rolled aluminum alloy sheets using a genetic algorithm. *Materials Science and Engineering A385*, 235-244.
- Kuroda, M., Tvergaard, V., 2000. Forming limit diagrams for anisotropic metal sheets with different yield criteria. *International Journal of Solids and Structures* 37, 5037-5059.
- Laukonis, J.V., Ghosh, A.K., 1978. Effects of strain path changes on the formability of sheet metals. *Metallurgical Transactions* 9A, 1849-1856.

- Lebensohn, R., Solas, D., Canova, G., Brechet, Y., 1996a. Modelling damage of Al-Zn-Mg alloys. *Acta Materialia* 44, 315-325.
- Lebensohn, R.A., Dawson, P.R., Kern, H.M., Wenk, H.R., 2003. Heterogeneous deformation and texture development in halite polycrystals: comparison of different modeling approaches and experimental data. *Tectonophysics* 370, 287-311.
- Lebensohn, R.A., Gonzalez, M.I., Tomé, C.N., Pochettino, A.A., 1996b. Measurement and prediction of texture development during a rolling sequence of Zircaloy-4 tubes. *Journal of Nuclear Materials* 229, 57-64.
- Lebensohn, R.A., Tomé, C.N., 1993. A self-consistent anisotropic approach for the simulation of plastic-deformation and texture development of polycrystals - application to zirconium alloys. *Acta Metallurgica Et Materialia* 41, 2611-2624.
- Lebensohn, R.A., Tomé, C.N., 1994. A self-consistent viscoplastic model - prediction of rolling textures of anisotropic polycrystals. *Materials Science and Engineering A175*, 71-82.
- Lebensohn, R.A., Tomé, C.N., Castaneda, P.P., 2007. Self-consistent modelling of the mechanical behaviour of viscoplastic polycrystals incorporating intragranular field fluctuations. *Philosophical Magazine* 87, 4287-4322.
- Lebensohn, R.A., Tomé, C.N., Maudlin, P.J., 2004. A selfconsistent formulation for the prediction of the anisotropic behavior of viscoplastic polycrystals with voids. *Journal of the Mechanics and Physics of Solids* 52, 249-278.
- Lebensohn, R.A., Turner, P.A., Signorelli, J.W., Canova, G.R., Tomé, C.N., 1998. Calculation of intergranular stresses based on a large-strain viscoplastic self-consistent polycrystal model. *Modelling and Simulation in Materials Science and Engineering* 6, 447-465.
- Lee, M.G., Kim, S.J., Wagoner, R.H., Chung, K., Kim, H.Y., 2009. Constitutive modeling for anisotropic/asymmetric hardening behavior of magnesium alloy sheets: Application to sheet springback. *International Journal of Plasticity* 25, 70-104.
- Lee, M.G., Wagoner, R.H., Lee, J.K., Chung, K., Kim, H.Y., 2008. Constitutive modeling for anisotropic/asymmetric hardening behavior of magnesium alloy sheets. *International Journal of Plasticity* 24, 545-582.
- Levesque, J., Inal, K., Neale, K.W., Mishra, R.K., 2010. Numerical modeling of formability of extruded magnesium alloy tubes. *International Journal of Plasticity* 26, 65-83.
- Li, J., Weng, G.J., 1997. A secant-viscosity approach to the time-dependent creep of an elastic-viscoplastic composite. *Journal of the Mechanics and Physics of Solids* 45, 1069-1083.
- Li, J., Weng, G.J., 1998a. Time-dependent creep of a dual-phase viscoplastic material with lamellar structure. *International Journal of Plasticity* 14, 755-770.
- Li, J., Weng, G.J., 1998b. A unified approach from elasticity to viscoelasticity to viscoplasticity of particle-reinforced solids. *International Journal of Plasticity* 14, 193-208.
- Li, M., Lou, X.Y., Kim, J.H., Wagoner, R.H., 2010. An efficient constitutive model for room-temperature, low-rate plasticity of annealed Mg AZ31B sheet. *International Journal of Plasticity* 26, 820-858.
- Lin, T.H., 1957. Analysis of elastic and plastic strains of face-centered cubic crystals. *Journal of the Mechanics and Physics of Solids* 5, 143-149.
- Lou, X.Y., Li, M., Boger, R.K., Agnew, S.R., Wagoner, R.H., 2007. Hardening evolution of AZ31B Mg sheet. *International Journal of Plasticity* 23, 44-86.
- Macewen, S.R., Christodoulou, N., Salinasrodriguez, A., 1990. Residual grain-interaction stresses in zirconium alloys. *Metallurgical Transactions* 21A, 1083-1095.
- Macewen, S.R., Faber, J., Turner, A.P.L., 1983. Overview .26. the use of time-of-flight neutron-diffraction to study grain interaction stresses. *Acta Metallurgica* 31, 657-676.
- Macewen, S.R., Tomé, C.N., Faber, J., 1989. Residual-stresses in annealed zircaloy. *Acta Metallurgica* 37, 979-989.

- Mahajan, S., Williams, D.F., 1973. Deformation twinning in metals and alloys. *International Materials Reviews* 3, 43-61.
- Marciniak, Z., Kuczynski, K., 1967. Limit strains in the process of stretch-forming sheet metal. *International Journal of Mechanical Sciences* 9, 609-620.
- Marcinkowski, M.J., Lipsitt, H.A., 1962. The plastic deformation of chromium at low temperature. *Acta Metallurgica* 10, 95-111.
- Mareau, C., Daymond, M.R., 2010. Study of internal strain evolution in Zircaloy-2 using polycrystalline models: Comparison between a rate-dependent and a rate-independent formulation. *Acta Materialia* 58, 3313-3325.
- Marin, T., Dawson, P.R., Gharghour, M.A., Rogge, R.B., 2008. Diffraction measurements of elastic strains in stainless steel subjected to in situ biaxial loading. *Acta Materialia* 56, 4183-4199.
- Masson, R., Bornert, M., Suquet, P., Zaoui, A., 2000. An affine formulation for the prediction of the effective properties of nonlinear composites and polycrystals. *Journal of the Mechanics and Physics of Solids* 48, 1203-1227.
- Mathewson, C.H., Phillips, A.J., 1928. Twinning in beryllium, magnesium, zinc and cadmium. *Proceedings Of The Institute Of Metals Division - AIME* 78.
- McDonald, J.C., 1940. Tensile properties of rolled magnesium alloys, I - binary alloys with aluminum, antimony, bismuth, cadmium, copper, lead, nickel, silver, thallium, tin and zinc. *Transactions of the Metallurgical Society of AIME* 137, 430-441.
- Mercier, S., Jacques, N., Molinari, A., 2005. Validation of an interaction law for the Eshelby inclusion problem in elasto-viscoplasticity. *International Journal of Solids and Structures* 42, 1923-1941.
- Mercier, S., Molinari, A., 2009. Homogenization of elastic-viscoplastic heterogeneous materials: Self-consistent and Mori-Tanaka schemes. *International Journal of Plasticity* 25, 1024-1048.
- Meyers, M.A., Vohringer, O., Lubarda, V.A., 2001. The onset of twinning in metals: A constitutive description. *Acta Materialia* 49, 4025-4039.
- Miura, S., 2004. Unpublished research. Hokkaido University, Hokkaido, Japan.
- Molinari, A., Ahzi, S., Kouddane, R., 1997. On the self-consistent modeling of elastic-plastic behavior of polycrystals. *Mechanics of Materials* 26, 43-62.
- Molinari, A., Canova, G.R., Ahzi, S., 1987. A self-consistent approach of the large deformation polycrystal viscoplasticity. *Acta Metallurgica* 35, 2983-2994.
- Molinari, A., Toth, L.S., 1994. Tuning a self-consistent viscoplastic model by finite-element results .I. modeling. *Acta Metallurgica Et Materialia* 42, 2453-2458.
- Mordike, B.L., Ebert, T., 2001. Magnesium - Properties - applications - potential. *Materials Science and Engineering A302*, 37-45.
- Mukai, T., Yamanoi, M., Watanabe, H., Higashi, K., 2001. Ductility enhancement in AZ31 magnesium alloy by controlling its grain structure. *Scripta Materialia* 45, 89-94.
- Mura, T., 1987. *Micromechanics of defects in solids*. Martinus Nijhoff, Dordrecht, The Netherlands.
- Muransky, O., Carr, D.G., Barnett, M.R., Oliver, E.C., Sittner, P., 2008. Investigation of deformation mechanisms involved in the plasticity of AZ31 Mg alloy: In situ neutron diffraction and EPSC modelling. *Materials Science and Engineering A496*, 14-24.
- Neale, K.W., Chater, E., 1980. Limit strain predictions for strain-rate sensitive anisotropic sheets. *International Journal of Mechanical Sciences* 22, 563-574.
- Neil, C.J., Agnew, S.R., 2009. Crystal plasticity-based forming limit prediction for non-cubic metals: Application to Mg alloy AZ31B. *International Journal of Plasticity* 25, 379-398.

- Neil, C.J., Wollmershauser, J.A., Clausen, B., Tomé, C.N., Agnew, S.R., 2010. Modeling lattice strain evolution at finite strains and experimental verification for copper and stainless steel using in situ neutron diffraction. *International Journal of Plasticity* 26, 1772-1791.
- Nemat-Nasser, S., Obata, M., 1986. Rate-dependent, finite elastoplastic deformation of polycrystals. *Proceedings of the Royal Society of London A407*, 343-375.
- Obara, T., Yoshinga, H., Morozumi, S., 1973. $\{11-22\}\langle 1-1\ 23\rangle$ slip systems in magnesium. *Acta Metallurgica* 21, 845-853.
- Paquin, A., Berbenni, S., Favier, V., Lemoine, X., Berveiller, M., 2001. Micromechanical modeling of the elastic-viscoplastic behavior of polycrystalline steels. *International Journal of Plasticity* 17, 1267-1302.
- Patridge, P.G., 1967. The crystallography and deformation modes of hexagonal close packed metals. *Metallurgical Reviews* 12, 169-194.
- Perez-Prado, M.T., del Valle, J.A., Contreras, J.M., Ruano, O.A., 2004. Microstructural evolution during large strain hot rolling of an AM60 Mg alloy. *Scripta Materialia* 50, 661-665.
- Plunkett, B., Cazacu, O., Barlat, F., 2008. Orthotropic yield criteria for description of the anisotropy in tension and compression of sheet metals. *International Journal of Plasticity* 24, 847-866.
- Poirier, J.P., Le Hazif, R., 1976. Microscopie électronique et déformation plastique des métaux et alliages hexagonaux compacts. *Journal de Microscopie et de Spectroscopie Electroniques* 1, 595-607.
- Potzies, C., Hort, N., Kainer, K.U., 2003. Proc 60th Annual IMA World Magnesium Conf.
- Proust, G., Tomé, C.N., Jain, A., Agnew, S.R., 2009. Modeling the effect of twinning and detwinning during strain-path changes of magnesium alloy AZ31. *International Journal of Plasticity* 25, 861-880.
- Rapperport, E.J., 1959. Room temperature deformation processes in zirconium. *Acta Metallurgica* 7, 254-260.
- Reed-Hill, R.E., 1960. A study of the $\{10-11\}$ and $\{10-13\}$ twinning modes in magnesium. *Transactions of the Metallurgical Society of AIME* 218, 554-558.
- Reed-Hill, R.E., 1973. The inhomogeneity of plastic deformation. American Society for Metals, Metals Park, OH.
- Reed-Hill, R.E., Robertson, W.D., 1957a. Additional modes of deformation twinning in magnesium. *Acta Metallurgica* 5, 717-727.
- Reed-Hill, R.E., Robertson, W.D., 1957b. Deformation of magnesium single crystals by nonbasal slip. *Transactions of AIME* 209, 496-502.
- Reed-Hill, R.E., Robertson, W.D., 1958. Pyramidal slip in magnesium. *Transactions of the Metallurgical Society of AIME* 212, 256-259.
- Sachs, G., 1928. Plasticity problems in metals. *Zeitschrift Verein Deutscher Ingenieur* 72, 734-736.
- Schmid, E., 1931. Beitrage zur physik und metallographie des magnesium. *Zeitschrift für Elektrochemie* 37, 447-459.
- Schmid, E., Boas, W., 1950. Plasticity of crystals with special reference to metals. Chapman and Hall LTD, London.
- Sheely, W.F., Nash, R.R., 1960. Mechanical properties of magnesium monocrystals. *Transactions of the Metallurgical Society of AIME* 218, 416-423.
- Shi, Y., Wu, P.D., Lloyd, D.J., Embury, J.D., 2010. Crystal plasticity based analysis of localized necking in aluminum tube under internal pressure. *European Journal of Mechanics a-Solids* 29, 475-483.
- Signorelli, J.W., Bertinetti, M.A., 2009. On the role of constitutive model in the forming limit of FCC sheet metal with cube orientations. *International Journal of Mechanical Sciences* 51, 473-480.

- Signorelli, J.W., Bertinetti, M.A., Turner, P.A., 2009. Predictions of forming limit diagrams using a rate-dependent polycrystal self-consistent plasticity model. *International Journal of Plasticity* 25, 1-25.
- Simmons, G., Wang, H., 1971. *Single crystal elastic constants and calculated polycrystal properties*. Cambridge (MA): MIT Press.137.
- Song, B., Huang, G.S., Li, H.C., Zhang, L., Huang, G.J., Pan, F.S., 2010. Texture evolution and mechanical properties of AZ31B magnesium alloy sheets processed by repeated unidirectional bending. *Journal of Alloys and Compounds* 489, 475-481.
- Staroselsky, A., Anand, L., 1998. Inelastic deformation of polycrystalline face centered cubic materials by slip and twinning. *Journal of the Mechanics and Physics of Solids* 46, 671-696.
- Staroselsky, A., Anand, L., 2003. A constitutive model for hcp materials deforming by slip and twinning: application to magnesium alloy AZ31B. *International Journal of Plasticity* 19, 1843-1864.
- Stohr, J.F., Poirier, J.P., 1972. Etude en microscopie electronique de glissement pyramidal $\{112\}\langle 1123\rangle$ dans le magnesium. *Philosophical Magazine* 25, 1313-1329.
- Stoughton, T.B., 2000. A general forming limit criterion for sheet metal forming. *International Journal of Mechanical Sciences* 42, 1-27.
- Stoughton, T.B., Zhu, X.H., 2004. Review of theoretical models of the strain-based FLD and their relevance to the stress-based FLD. *International Journal of Plasticity* 20, 1463-1486.
- Styczynski, A., Hartig, C., Bohlen, J., Letzig, D., 2004. Cold rolling textures in AZ31 wrought magnesium alloy. *Scripta Materialia* 50, 943-947.
- Taylor, G.I., 1938. Plastic strain in metals. *Journal of the Institute of Metals* 62, 307-324.
- Thompson, N., Millard, D.J., 1952. Twin formation, in cadmium. *Philosophical Magazine* 43, 422-440.
- Tomé, C.N., 1999. Self-consistent polycrystal models: a directional compliance criterion to describe grain interactions. *Modelling and Simulation in Materials Science and Engineering* 7, 723-738.
- Tomé, C.N., Canova, G.R., Kocks, U.F., Christodoulou, N., Jonas, J.J., 1984. The relation between macroscopic and microscopic strain-hardening in FCC polycrystals. *Acta Metallurgica* 32, 1637-1653.
- Tomé, C.N., Lebensohn, R.A., Kocks, U.F., 1991. A model for texture development dominated by deformation twinning - application to zirconium alloys. *Acta Metallurgica Et Materialia* 39, 2667-2680.
- Tomé, C.N., Pochettino, A.A., Penelle, R., 1988. Analysis of plastic anisotropy of rolled zircaloy-4. ICOTOM: Eighth International Conference on Textures of Materials; Santa Fe, New Mexico; USA. 985-990.
- Turner, P.A., Tomé, C.N., 1993. Self-consistent modeling of viscoelastic polycrystals - application to irradiation creep and growth. *Journal of the Mechanics and Physics of Solids* 41, 1191-1211.
- Turner, P.A., Tomé, C.N., 1994. A study of residual-stresses in zircaloy-2 with rod texture. *Acta Metallurgica Et Materialia* 42, 4143-4153.
- Turner, P.A., Tomé, C.N., Woo, C.H., 1994. Self-consistent modeling of nonlinear viscoelastic polycrystals - an approximate scheme. *Philosophical Magazine* A70, 689-711.
- Walpole, L.J., 1969. On the overall elastic moduli of composite materials. *Journal of the Mechanics and Physics of Solids* 17, 235-251.
- Wang, H., Raeisnia, B., Wu, P.D., Agnew, S.R., Tomé, C.N., 2010a. Evaluation of self-consistent crystal plasticity models for magnesium alloy AZ31B sheet. *International Journal of Solids and Structures* 47, 2905-2917.

- Wang, H., Wu, P.D., Boyle, K.P., Neale, K.W., 2010b. On crystal plasticity formability analysis for magnesium alloy sheets. *International Journal of Solids and Structures*. In press, doi:10.1016/j.ijsolstr.2010.1012.1004.
- Wang, H., Wu, P.D., Gharghour, M.A., 2010c. Effects of basal texture on mechanical behaviour of magnesium alloy AZ31B sheet. *Materials Science and Engineering A527*, 3588-3594.
- Wang, H., Wu, P.D., Neale, K.W., 2010d. On the role of the constitutive model and basal texture on the mechanical behavior of magnesium alloy AZ31B sheet. *Journal of Zhejiang University-SCIENCE A* 11, 744-755.
- Wang, H., Wu, P.D., Tomé, C.N., Huang, Y., 2010e. A finite strain elastic-viscoplastic self-consistent model for polycrystalline materials. *Journal of the Mechanics and Physics of Solids* 58, 594-612.
- Wang, Y.C., Mora, P., 2008. Macroscopic elastic properties of regular lattices. *Journal of the Mechanics and Physics of Solids* 56, 3459-3474.
- Ward Flynn, P., Mote, J., Dorn, J.E., 1961. On the thermally activated mechanism of prismatic slip in magnesium single crystals. *Transactions of the Metallurgical Society of AIME* 221, 1148-1154.
- Weng, G.J., 1981. A self-consistent scheme for the relaxation behavior of metals. *Journal of Applied Mechanics* 48, 779-784.
- Weng, G.J., 1982. A unified, self-consistent theory for the plastic-creep deformation of metals. *Journal of Applied Mechanics* 49, 728-734.
- Weng, G.J., 1993. A self-consistent relation for the time-dependent creep of polycrystals. *International Journal of Plasticity* 9, 181-198.
- Wonsiewicz, B.C., Backofen, W.A., 1967. Plasticity of magnesium crystals. *Transactions of the Metallurgical Society of AIME* 239, 1422-1431.
- Wu, P.D., Graf, A., Jain, M., MacEwen, S.R., 2000. On alternative representation of forming limits. *Key Engineering Materials* 177-180, 517-522.
- Wu, P.D., Graf, A., MacEwen, S.R., Lloyd, D.J., Jain, M., Neale, K.W., 2005. On forming limit stress diagram analysis. *International Journal of Solids and Structures* 42, 2225-2241.
- Wu, P.D., Huang, Y., Lloyd, D.J., 2006. Studying grain fragmentation in ECAE by simulating simple shear. *Scripta Materialia* 54, 2107-2112.
- Wu, P.D., Jain, M., Savoie, J., MacEwen, S.R., Tugcu, P., Neale, K.W., 2003. Evaluation of anisotropic yield functions for aluminum sheets. *International Journal of Plasticity* 19, 121-138.
- Wu, P.D., Lloyd, D.J., 2004. Analysis of surface roughening in AA6111 automotive sheet. *Acta Materialia* 52, 1785-1798.
- Wu, P.D., Lloyd, D.J., Jain, M., Neale, K.W., Huang, Y., 2007a. Effects of spatial grain orientation distribution and initial surface topography on sheet metal necking. *International Journal of Plasticity* 23, 1084-1104.
- Wu, P.D., MacEwen, S.R., Lloyd, D.J., Neale, K.W., 2004a. Effect of cube texture on sheet metal formability. *Materials Science and Engineering A364*, 182-187.
- Wu, P.D., MacEwen, S.R., Lloyd, D.J., Neale, K.W., 2004b. A mesoscopic approach for predicting sheet metal formability. *Modelling and Simulation in Materials Science and Engineering* 12, 511-527.
- Wu, P.D., Neale, K.W., Van der Giessen, E., 1997. On crystal plasticity FLD analysis. *Proceedings of the Royal Society of London A453*, 1831-1848.
- Wu, P.D., Neale, K.W., Van der Giessen, E., Jain, M., Makinde, A., MacEwen, S.R., 1998. Crystal plasticity forming limit diagram analysis of rolled aluminum sheets. *Metallurgical and Materials Transactions* 29A, 527-535.

- Wu, X.P., Kalidindi, S.R., Necker, C., Salem, A.A., 2007b. Prediction of crystallographic texture evolution and anisotropic stress-strain curves during large plastic strains in high purity alpha-titanium using a Taylor-type crystal plasticity model. *Acta Materialia* 55, 423-432.
- Xu, F., Holt, R.A., Daymond, M.R., 2008. Modeling lattice strain evolution during uniaxial deformation of textured Zircaloy-2. *Acta Materialia* 56, 3672-3687.
- Yoo, M.H., 1981. Slip, twinning, and fracture in hexagonal close-packed metals. *Metallurgical Transactions* 12A, 409-418.
- Yoo, M.H., Wei, C.T., 1967. Slip modes of hexagonal-close-packed metals. *Journal of Applied Physics* 38, 4317-4322.
- Yoon, J.W., Barlat, F., Chung, K., Pourboghrat, F., Yang, D.Y., 1998. Influence of initial back stress on the earing prediction of drawn cups for planar anisotropic aluminum sheets. *Journal of Materials Processing Technology* 80-81, 433-437.
- Yoshida, K., Ishizaka, T., Kuroda, M., Ikawa, S., 2007. The effects of texture on formability of aluminum alloy sheets. *Acta Materialia* 55, 4499-4506.
- Yoshinaga, H., Horiuchi, R., 1964. On the nonbasal slip in magnesium crystals. *Transactions of the Japan Institute of Metals* 5, 14-21.
- Zaoui, A., 2002. Continuum micromechanics: Survey. *Journal of Engineering Mechanics-ASCE* 128, 808-816.
- Zaoui, A., Raphanel, 1991. On the nature of the intergranular accommodation in the modelling of elastic-plastic behavior of crystalline materials. In: Teodosiu, T. et al. (Eds), *Large Plastic Deformations, Fundamentals and Applications of Metal Forming*. Balkema, Rotterdam, The Netherlands, pp. 185-192.
- Zhang, H., Yan, Q.Q., Li, L.X., 2008. Microstructures and tensile properties of AZ31 magnesium alloy by continuous extrusion forming process. *Materials Science and Engineering A486*, 295-299.
- Zhao, L., Sowerby, R., Sklad, M.P., 1996. A theoretical and experimental investigation of limit strains in sheet metal forming. *International Journal of Mechanical Sciences* 38, 1307-1317.
- Zhou, Y., Neale, K.W., 1995. Predictions of forming limit diagrams using a rate-sensitive crystal plasticity model. *International Journal of Mechanical Sciences* 37, 1-20.

